



SAIMM

THE SOUTHERN AFRICAN INSTITUTE
OF MINING AND METALLURGY

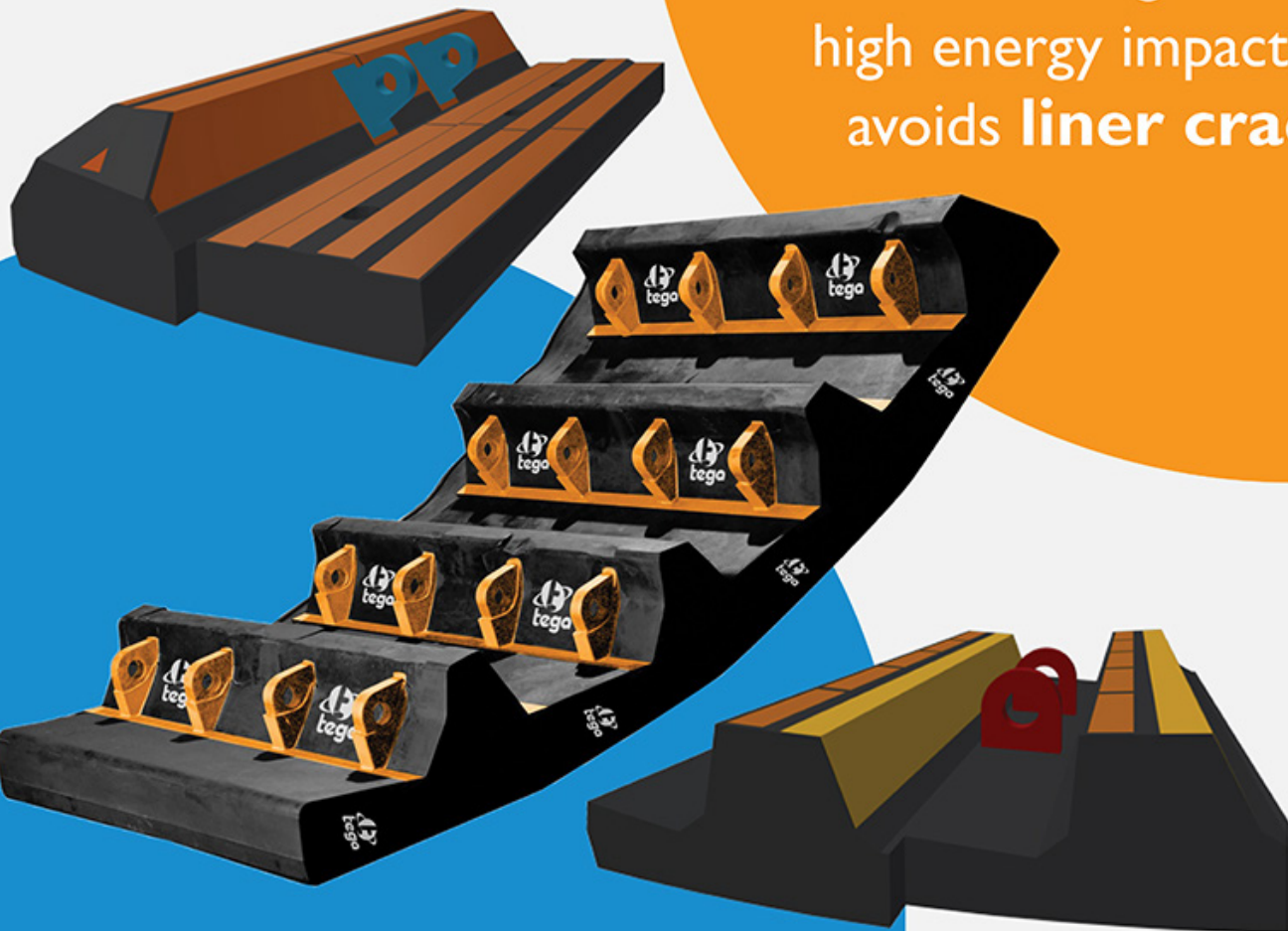
VOLUME 121 NO. 11 NOVEMBER 2021



an ideal liner for high
aspect SAG mills from
34 to 40ft in diameter

maximizes mill
availability

Resilient design cushions
high energy impacts and
avoids **liner cracks**



PARTNERSHIPS IN PRACTICE



DynaWear lining
solution for Ball Mills

peace of mind

DynaWear, ensuring optimised mill liner life, grinding efficiency and capacity, delivering maximum cost benefit to our clients.



PARTNERSHIPS IN PRACTICE

OFFICE BEARERS AND COUNCIL FOR THE 2021/2022 SESSION

Honorary President

Nolitha Fakude
President, Minerals Council South Africa

Honorary Vice Presidents

Gwede Mantashe
Minister of Mineral Resources, South Africa

Ebrahim Patel
Minister of Trade, Industry and Competition, South Africa

Blade Nzimande
Minister of Higher Education, Science and Technology, South Africa

President

I.J. Geldenhuys

President Elect

Z. Botha

Senior Vice President

W.C. Joughin

Junior Vice President

E Matinde

Incoming Junior Vice President

G.R. Lane

Immediate Past President

V.G. Duke

Honorary Treasurer

W.C. Joughin

Ordinary Members on Council

Z. Fakhraei	S.J. Ntsoelengoe
B. Genc	S.M. Rupprecht
K.M. Letsoalo	A.J.S. Spearing
S.B. Madolo	M.H. Solomon
F.T. Manyanga	S.J. Tose
T.M. Mmola	A.T. van Zyl
G. Njowa	E.J. Walls

Co-opted Members

M. Aziz
M.I. van der Bank

Past Presidents Serving on Council

N.A. Barcza	S. Ndlovu
R.D. Beck	J.L. Porter
J.R. Dixon	S.J. Ramokgopa
R.T. Jones	M.H. Rogers
A.S. Macfarlane	D.A.J. Ross-Watt
M.I. Mthenjane	G.L. Smith
C. Musingwini	W.H. van Niekerk

G.R. Lane-TPC Mining Chairperson
Z. Botha-TPC Metallurgy Chairperson

A.T. Chinhava-YPC Chairperson
M.A. Mello-YPC Vice Chairperson

Branch Chairpersons

Johannesburg	D.F. Jensen
Namibia	N.M. Namate
Northern Cape	Jaco Mans
Pretoria	J. Mans
Western Cape	A.B. Nesbitt
Zambia	Vacant
Zimbabwe	C.P. Sadomba
Zululand	C.W. Mienie

PAST PRESIDENTS

*Deceased

- * W. Bettel (1894–1895)
- * A.F. Crosse (1895–1896)
- * W.R. Feldtmann (1896–1897)
- * C. Butters (1897–1898)
- * J. Loevy (1898–1899)
- * J.R. Williams (1899–1903)
- * S.H. Pearce (1903–1904)
- * W.A. Caldecott (1904–1905)
- * W. Cullen (1905–1906)
- * E.H. Johnson (1906–1907)
- * J. Yates (1907–1908)
- * R.G. Bevington (1908–1909)
- * A. McA. Johnston (1909–1910)
- * J. Moir (1910–1911)
- * C.B. Saner (1911–1912)
- * W.R. Dowling (1912–1913)
- * A. Richardson (1913–1914)
- * G.H. Stanley (1914–1915)
- * J.E. Thomas (1915–1916)
- * J.A. Wilkinson (1916–1917)
- * G. Hildick-Smith (1917–1918)
- * H.S. Meyer (1918–1919)
- * J. Gray (1919–1920)
- * J. Chilton (1920–1921)
- * F. Wartenweiler (1921–1922)
- * G.A. Watermeyer (1922–1923)
- * F.W. Watson (1923–1924)
- * C.J. Gray (1924–1925)
- * H.A. White (1925–1926)
- * H.R. Adam (1926–1927)
- * Sir Robert Kotze (1927–1928)
- * J.A. Woodburn (1928–1929)
- * H. Pirow (1929–1930)
- * J. Henderson (1930–1931)
- * A. King (1931–1932)
- * V. Nimmo-Dewar (1932–1933)
- * P.N. Lategan (1933–1934)
- * E.C. Ranson (1934–1935)
- * R.A. Flugge-De-Smidt (1935–1936)
- * T.K. Prentice (1936–1937)
- * R.S.G. Stokes (1937–1938)
- * P.E. Hall (1938–1939)
- * E.H.A. Joseph (1939–1940)
- * J.H. Dobson (1940–1941)
- * Theo Meyer (1941–1942)
- * John V. Muller (1942–1943)
- * C. Biccard Jeppe (1943–1944)
- * P.J. Louis Bok (1944–1945)
- * J.T. McIntyre (1945–1946)
- * M. Falcon (1946–1947)
- * A. Clemens (1947–1948)
- * F.G. Hill (1948–1949)
- * O.A.E. Jackson (1949–1950)
- * W.E. Gooday (1950–1951)
- * C.J. Irving (1951–1952)
- * D.D. Stitt (1952–1953)
- * M.C.G. Meyer (1953–1954)
- * L.A. Bushell (1954–1955)
- * H. Britten (1955–1956)
- * Wm. Bleloch (1956–1957)
- * H. Simon (1957–1958)
- * M. Barcza (1958–1959)
- * R.J. Adamson (1959–1960)
- * W.S. Findlay (1960–1961)
- * D.G. Maxwell (1961–1962)
- * J. de V. Lambrechts (1962–1963)
- * J.F. Reid (1963–1964)
- * D.M. Jamieson (1964–1965)
- * H.E. Cross (1965–1966)
- * D. Gordon Jones (1966–1967)
- * P. Lambooy (1967–1968)
- * R.C.J. Goode (1968–1969)
- * J.K.E. Douglas (1969–1970)
- * V.C. Robinson (1970–1971)
- * D.D. Howat (1971–1972)
- * J.P. Hugo (1972–1973)
- * P.W.J. van Rensburg (1973–1974)
- * R.P. Plewman (1974–1975)
- * R.E. Robinson (1975–1976)
- * M.D.G. Salamon (1976–1977)
- * P.A. Von Wielligh (1977–1978)
- * M.G. Atmore (1978–1979)
- * D.A. Viljoen (1979–1980)
- * P.R. Jochens (1980–1981)
- * G.Y. Nisbet (1981–1982)
- * A.N. Brown (1982–1983)
- * R.P. King (1983–1984)
- * J.D. Austin (1984–1985)
- * H.E. James (1985–1986)
- * H. Wagner (1986–1987)
- * B.C. Alberts (1987–1988)
- * C.E. Fivaz (1988–1989)
- * O.K.H. Steffen (1989–1990)
- * H.G. Mosenthal (1990–1991)
- * R.D. Beck (1991–1992)
- * J.P. Hoffman (1992–1993)
- * H. Scott-Russell (1993–1994)
- * J.A. Cruise (1994–1995)
- * D.A.J. Ross-Watt (1995–1996)
- * N.A. Barcza (1996–1997)
- * R.P. Mohring (1997–1998)
- * J.R. Dixon (1998–1999)
- * M.H. Rogers (1999–2000)
- * L.A. Cramer (2000–2001)
- * A.A.B. Douglas (2001–2002)
- * S.J. Ramokgopa (2002–2003)
- * T.R. Stacey (2003–2004)
- * F.M.G. Egerton (2004–2005)
- * W.H. van Niekerk (2005–2006)
- * R.P.H. Willis (2006–2007)
- * R.G.B. Pickering (2007–2008)
- * A.M. Garbers-Craig (2008–2009)
- * J.C. Ngoma (2009–2010)
- * G.V.R. Landman (2010–2011)
- * J.N. van der Merwe (2011–2012)
- * G.L. Smith (2012–2013)
- * M. Dworzanowski (2013–2014)
- * J.L. Porter (2014–2015)
- * R.T. Jones (2015–2016)
- * C. Musingwini (2016–2017)
- * S. Ndlovu (2017–2018)
- * A.S. Macfarlane (2018–2019)
- * M.I. Mthenjane (2019–2020)
- * V.G. Duke (2020–2021)

Honorary Legal Advisers

M H Attorneys

Auditors

Genesis Chartered Accountants

Secretaries

The Southern African Institute of Mining and Metallurgy

Fifth Floor, Minerals Council South Africa

5 Hollar Street, Johannesburg 2001 • P.O. Box 61127, Marshalltown 2107

Telephone (011) 834-1273/7 • Fax (011) 838-5923 or (011) 833-8156

E-mail: journal@saimm.co.za

Editorial Board

S.O. Bada
R.D. Beck
P. den Hoed
I.M. Dikgwathe
R. Dimitrakopoulos*
M. Dworzanowski*
L. Falcon
B. Genc
R.T. Jones
W.C. Joughin
A.J. Kinghorn
D.E.P. Klenam
H.M. Lodewijks
D.F. Malan
R. Mitra*
H. Möller
C. Musingwini
S. Ndlovu
P.N. Neingo
M. Nicol*
S.S. Nyoni
P. Pistorius
N. Rampersad
Q.G. Reynolds
I. Robinson
S.M. Rupprecht
K.C. Sole
A.J.S. Spearing*
T.R. Stacey
E. Topal*
D. Tudor*
F.D.L. Uahengo
D. Vogt*

*International Advisory Board members

Editor /Chairman of the Editorial Board

R.M.S. Falcon

Typeset and Published by

The Southern African Institute of Mining and Metallurgy
P.O. Box 61127
Marshalltown 2107
Telephone (011) 834-1273/7
Fax (011) 838-5923
E-mail: journal@saimm.co.za

Printed by

Camera Press, Johannesburg

Advertising Representative

Barbara Spence
Avenue Advertising
Telephone (011) 463-7940
E-mail: barbara@avenue.co.za

ISSN 2225-6253 (print)
ISSN 2411-9717 (online)



Directory of Open Access Journals



SAIMM

JOURNAL OF THE SOUTHERN AFRICAN INSTITUTE OF MINING AND METALLURGY

VOLUME 121 NO. 11 NOVEMBER 2021

Contents

Journal Comment: The great conundrum

by R.M.S. Falcon iv-v

President's Corner: To succeed, we need to care

by I.J. Geldenhuys vi-vii

Obituary: Darius Muma

by O. Mahenga and S. Moolla viii

PROFESSIONAL TECHNICAL AND SCIENTIFIC PAPERS

The effect of non-standard loading platen usage on point load index value of rocks

by D. Akbay and R. Altındağ 565

The point load index is a simple, fast, and inexpensive method for determining rock strength that can be applied both in the field and in the laboratory. There are, however, many factors that affect the test result. This study describes an investigation into how the point load index value is affected by the wear of the conical platens in the test device. Experiments were carried out using different test devices fitted with platens of different spherical radii, and on a modified test device that eliminates the human (operator) factor. An equation is proposed to normalize the point load index value with respect to the standard spherical radius value.

Local magnitude calibration of seismic events in the West Rand, Far West Rand, and Klerksdorp–Orkney–Stilfontein–Hartebeesfontein gold mining areas

by M.B.C. Brandt 573

Richter magnitudes for seismic events in South Africa's major gold-mining areas are currently calculated using tabulated calibration values for Southern California, published in 1958. However, this model is incorrect for distances of less than 30 km and should only be applied to crustal earthquakes in regions with similar attenuation properties to those of Southern California. A calibrated Local magnitude scale was derived by means of a multiple regression analysis between the Local magnitudes reported by the South African National Seismograph Network (SANSN) and the largest zero-to-peak trace amplitudes measured on the cluster network horizontal seismograms. Magnitudes reported by individual stations for the same event show a significant scatter around the average owing to the near-surface amplifications of the seismic waves. Average magnitude should be estimated using magnitudes from as many individual stations as possible. Larger event magnitudes should be compared with those recorded by the SANSN.

THE INSTITUTE, AS A BODY, IS NOT RESPONSIBLE FOR THE STATEMENTS AND OPINIONS ADVANCED IN ANY OF ITS PUBLICATIONS.

Copyright© 2021 by The Southern African Institute of Mining and Metallurgy. All rights reserved. Multiple copying of the contents of this publication or parts thereof without permission is in breach of copyright, but permission is hereby given for the copying of titles and abstracts of papers and names of authors. Permission to copy illustrations and short extracts from the text of individual contributions is usually given upon written application to the Institute, provided that the source (and where appropriate, the copyright) is acknowledged. Apart from any fair dealing for the purposes of review or criticism under **The Copyright Act no. 98, 1978, Section 12**, of the Republic of South Africa, a single copy of an article may be supplied by a library for the purposes of research or private study. No part of this publication may be reproduced, stored in a retrieval system, or transmitted in any form or by any means without the prior permission of the publishers. **Multiple copying of the contents of the publication without permission is always illegal.**

U.S. Copyright Law applicable to users in the U.S.A.

The appearance of the statement of copyright at the bottom of the first page of an article appearing in this journal indicates that the copyright holder consents to the making of copies of the article for personal or internal use. This consent is given on condition that the copier pays the stated fee for each copy of a paper beyond that permitted by Section 107 or 108 of the U.S. Copyright Law. The fee is to be paid through the Copyright Clearance Center, Inc., Operations Center, P.O. Box 765, Schenectady, New York 12301, U.S.A. This consent does not extend to other kinds of copying, such as copying for general distribution, for advertising or promotional purposes, for creating new collective works, or for resale.



Comparison of normalized and non-normalized block caving comminution models	
by R. Gómez, R. Castro, F. Betancourt, and M. Moncada.	581
<i>In block cave mining, rock fragmentation is a key parameter that influences the production level design and mine planning. The block caving comminution model, which replicates the fragmentation mechanics between particles under drawn and vertical loads in a draw column, is based on a kinetic and population balance approach, in which non-normalized and normalized assumptions can be used depending on material and comminution system behaviour. In this paper, the non-normalized and normalized approaches are applied and compared to laboratory data to determine which assumption should be used. Based on a statistical analysis, results show that the normalized model can be applied to all the rock types tested.</i>	
Improving productivity at an open-pit mine through enhanced short-term mine planning	
by T.J. Otto and G.C. Lindeque	589
<i>Improving the productivity of heavy mining equipment (HME) at an open-pit mine reduces the unit cost of production. This paper details the improvements in HME productivity that were realized at the Kolomela iron ore mine by implementing an enhanced short-term mine planning (STMP) process. The improvements in the utilization of mining area, blasting frequency and average blast size, distance travelled during shovel relocations, and lost time associated with drills relocating resulted in an 11% increase in the loading rate of the main waste shovel at Kolomela. The enhanced STMP process can be adapted to other open-pit mining operations to improve HME productivity.</i>	
Behaviour of Cu, Fe, Ni, and PGMs during leaching of Ni-Fe-Cu-S converter matte	
by A.P. Van Wyk, G. Akdogan, and S.M. Bradshaw	599
<i>This project investigated the atmospheric leaching of Ni-Cu-Fe-S converter matte to develop a better understanding of the leaching behaviour of the base metals and PGMs under oxidative and non-oxidative conditions. For oxidative leaching conditions, a higher initial acid concentration resulted in higher Cu, Ni and Fe extractions, as well as higher leaching reaction rates. Higher initial acid concentration also resulted in faster Cu, Ru and Ir precipitation. Ni and Fe extraction was much slower under non-oxidative conditions, and the effect of initial acid concentration on Cu precipitation was less pronounced. A higher initial Cu concentration suppressed both Ni and Fe leaching and had a slight negative effect on the precipitation behaviour of Cu, Ru, and Ir.</i>	
A critical review of initial Resource and Reserve tonnage estimation and reporting	
by L. Roux	607
<i>The reporting of Coal Resources in South Africa has been found to be inconsistent, particularly in the Waterberg Coalfield. This review seeks to reconcile run-of-mine production tons with the Coal Resource and Reserve estimation of mineable, in-situ tonnages. Practices and methods are described, alternatives investigated, and checks and balances provided and tested against actual production reconciliations. The greatest contributing factor to the overestimation of Reserve tonnages is the moisture content of the raw material. The best estimates of the mineable, in-situ tonnage will be obtained from the air-dry, raw material density, adjusted to allow for free moisture content.</i>	



The great conundrum



The world is currently going through two major events simultaneously, in a once-in-a-lifetime or 100-year experience: a major pandemic and, as a longer-term cycle, climate change. In reading between the lines, neither has been solved to a satisfactory conclusion and neither are likely to be solved any time soon.

Of specific interest to the mineral, mining and metallurgical industries in the world is the climate change issue. This is where the great divide comes in – firstly, climate scientists and numerous environmental lobbyists projecting that the world is nearing extinction, disaster, more catastrophic weather patterns, and the demise of hundreds of thousands of people, as well as numerous low-lying islands due to projected sea level rise.

This is counterbalanced by alternate views that offer other, less drastic scientific projections based on results drawn from past facts, current experience and other carefully drawn calculations showing far lower points of concern, and setting the world's climate and weather patterns into a more modest and cyclical pattern over a far longer timespan. Such views are often not permitted to be published in the open media.

In essence, both parties claim REALITY, one on the basis of unknown and as yet **unproven future values** as predicted by predicted equations, and the other based on **past experience over millennia**, and more modest, currently experienced views. The history of global emissions is summarized as follows.

At the beginning of the 20th century, smoke pouring out of a chimney was a sign of progress, prosperity and job creation. However, the problems of poor air quality, as early as the end of the 16th century, are well documented. By the middle of the 20th century, air pollution was recognised as a serious problem. For example, the London smog of 1952 resulted in approximately 4000 extra deaths in the city, leading to the introduction of the Clean Air Acts of 1956 and 1968.

Factories and households were subject to smoke emission limitations because of health, safety and environmental reasons. On the other hand, the de-smoking was accompanied by capital and operating costs.

The de-smoking process has always had a negative impact on the 'bottom line' of industrial operations, being an expense that did not earn income but was an essential condition for an operating licence. However, the internalization of external impacts greatly increased the quality of life. The limiting of other pollutants quickly followed, for example de-SOx and de-NOx. Each had its accompanying costs. The limitations of emissions of such pollutants are controlled by regulation.

In a similar vein more recently, the mitigation of greenhouse gas emissions is being addressed as a measure to address global climate change. Such de-carbonization is also accompanied by a cost. The difference between de-smoke, de-SOx and de-NOx and de-carbonization is that the first three are local/regional impacts whereas de-carbonization is considered to be of global concern.

The mitigation of greenhouse gas emissions is therefore now a global matter. For instance, if South Africa alone were to stop using fossil fuels tomorrow, such action would have no noticeable impact on global climate change, but would impact our gross domestic product. However, as de-carbonization is a global action matter, South Africa is obliged to implement such measures in concert with the rest of the world.

But South Africa, and likewise other developing countries, need to balance socio-economic and industrial development with environmental matters. There are five main options to de-carbonise energy that are being undertaken internationally, namely:

- **Fuel Switching**—Switching from high carbon fuels to low carbon fuels leads to lower carbon dioxide emissions. For example, switching from coal to natural gas for electricity generation has been calculated to decrease carbon dioxide emissions by approximately 50%. However, questions arise as to the validity of this calculation. In the case of South Africa, natural gas is in any case scarce, and politically controlled by neighbouring countries, if available at all. The Hydrogen Economy has its own problems as water is required, as well as high levels of power in the manufacture of hydrogen – of which the scarcity of inland water is the most limiting.

Journal Comment (continued)

- *Energy Efficiency*— It is commonsense to use less energy and achieve the same output, thereby lowering energy costs. An example is the swapping of incandescent light bulbs (typically <5% efficient) with a more efficient form of lighting such as a compact fluorescent light bulb (typically 85% efficient) or a light emitting diode (LED) (typically 90% efficient).
- *Renewable Energy*—Renewable energy emits very little carbon dioxide during operation. However, carbon dioxide is emitted during the manufacture of the iron, steel, glass and cement required for construction, and during the mining required to obtain the components for such manufacture. Furthermore, renewable plants have a life span of only 15 to 20 years (*versus* a coal-fired plant of 60 years), and solar panels and wind turbine blades are problematic in their end-of-life discarding, as such materials contain hazardous and dangerous trace elements. The density of renewables is of the order of one part fossil fuel power to 4 to 6 power units from renewable power, each of which require space, and reliable expensive batteries or alternate backup power-generating sources. It is of interest to note that the lack of power during COP26 meetings resulted from low wind and solar power in the UK during that period, and local power conventional power stations were called on to supply the necessary electricity during that period.
- *Nuclear*—Nuclear emits very little carbon dioxide during operation. However, carbon dioxide is emitted during the manufacture of the iron, steel and cement required for nuclear power plant construction, and from the mining required to obtain both uranium and the components for such plant manufacture. However, nuclear is the source most likely to supply energy in the future once fission has been developed to its required control levels.
- *Carbon Capture Utilization and Storage*—This involves capturing the carbon dioxide before it is released into the atmosphere and storing it in an appropriately deep geological formation. It is also possible to utilize carbon dioxide to create higher energy products, using renewable energy.

The most notable use of carbon dioxide is for enhanced oil recovery, where approximately 50% of the injected carbon dioxide remains in the geological formation. South Africa has no oil deposits where this technology can be used. However, recent research has shown that CO₂ from Eskom-equivalent flue gases can be used to manufacture valuable carbon materials, including carbon nanotubes, carbon fibre, and activated carbon. Other greenhouse gases are also now able to be utilized for the manufacture of a host of other valuable commodities, including fertilizers and sulphuric acid for the mining industry. It is worth noting that Sasol, in gasifying coal, supplies one third of South Africa's liquid fuels including petrol, and many dozens of chemicals, paint, plastics, explosives, pharmaceuticals and cloth, and a vast array of other industrial materials and chemicals. Coal and its related sediments are also valuable sources of rare earth elements.

Of particular interest to coal-rich countries is the example of the clean coal technologies, of which the Turk Power Station in the USA is one such example. This coal-fired power plant has been running for some time in the USA and it produces 99.9% clean air – *i.e.* NO emissions at all. This example mirrors many plants now operating or currently being installed in the Far East.

Each of these options has a different maturity profile, as well as varying associated costs. Once emission limitations are imposed it would be up to each person, company or country to determine which technology is appropriate for that person or body's use. But the question needs to be asked – why not consider the alternate view and use such emissions at great benefit to the country until the maturing of safe and reliable energy sources (fission?) are developed in the medium to longer term?

The important role of coal in South Africa's power generation and manufacturing economy is evident. Its role can be expected to continue for many years as the country moves to meet its environmental commitments. It is important to understand this resource and its use so that it can be utilized in the most effective, responsible and efficient manner.

R.M.S. Falcon



To succeed, we need to care



The 1995 film ‘The Englishman Who Went up a Hill but Came down a Mountain’ is set in 1917, with World War I in the background, and revolves around two English cartographers arriving at a Welsh village to measure its ‘mountain’ to update the official maps of the region. When the cartographers conclude that the mountain is only a hill because it is slightly short of the required height of 1000 feet (305 m) for a mountain, the villagers conspire to delay their departure while they build an earth mound on top of their hill, aiming to make it high enough to rank as a mountain. The story is told humorously against the backdrop of a small Welsh community trying to save their town’s honour, but underlying the

machinations of the villagers, there is more. In this story, Garw Mountain symbolises the restoration of the community’s war-damaged self-esteem and illustrates the importance of shared purpose and vision. We live in times of immense turmoil and uncertainty. Our decisions and actions over the next 50 years or so will determine the quality of life of the human villagers of the future.

Ok (short for Okjökull) is the first Icelandic glacier to lose its status as a glacier. Scientists agree that glaciers have disappeared from Iceland before, none as ceremoniously as Okjökull though. The once-iconic glacier melted away throughout the 20th century and was formally declared dead in 2014 by glaciologist Oddur Sigurðsson. The glacier’s demise is not just a matter of shrinking area, although by 2019, less than a square kilometre remained of the more than 38 square kilometres estimated in 1901. Glaciers form from snow that becomes compacted into ice over time and the ice slowly creeps downslope under its own weight, helped along by gravity. Ok thinned so much that by 2014 it no longer had enough mass to move and became stagnant. And according to some definitions, a stagnant glacier is a dead glacier. In 2018, anthropologists Cymene Howe and Dominic Boyer of Rice University filmed a documentary about the demise of Ok (‘Not Ok’) and proposed that a commemorative plaque be placed to memorialize the loss as a reminder of the impact of climate change. The plaque was installed at the location of the former glacier in August 2019, with an inscription titled ‘A letter to the future’. The letter to our future reads as follows:

*Ok is the first Icelandic glacier to lose its status as a glacier.
In the next 200 years all our glaciers are expected to follow the same path.
This monument is to acknowledge that we know
what is happening and what needs to be done.
Only you know if we did it.*



Photograph by Rice University¹ of the plaque placed at the former location of the Okjökull glacier in Iceland

¹https://commons.wikimedia.org/wiki/File:Okj%C3%B6kull_glacier_commemorative_plaque.jpg

President's Corner *(continued)*

The placement of the plaque and the letter to the future is akin to the two cartographers walking into our global village and declaring our mountain to be a hill. In the story of the Garw Mountain, in the end, the villagers prevailed; they delayed the departure of the surveyors and raised the height of the hill by working together on what seemed to be an unsurmountable problem. They succeeded because they cared and actively worked to achieve their purpose. It is said that about five years after the event when the new edition of the relevant map, which showed Ffynnon Garw Mountain at 1002 feet, was published, all the residents of the village on which the movie story was based had a copy in their homes. And for interest, according to the current Ordnance Survey covering Cardiff and Bridgend, the height of what is now known as Garth Hill is 307 metres (1007 feet), still making it a mountain. Unfortunately for Ok, we have only a plaque to remind us of what it once was, namely a majestic glacier. But we know what to do.

We hear about environmental, social, and governance (ESG) in boardrooms, at conferences, indabas, and in corporate governance reports, webinars, the press, blogs, and the SAIMM Journal's Presidential Corners. The term ESG was first coined in 2005 in a landmark study by the International Finance Corporation entitled 'Who Cares Wins'. The study made the case that embedding environmental, social, and governance factors in capital markets makes good business sense and leads to more sustainable markets and better outcomes for societies. Nearly two decades later, one may argue that we are still struggling to agree on rules, definitions, and criteria. While we grapple with definitions ('how high is a mountain?' or 'when is a glacier dead?') and whether you believe that Ok is dead, or Garth Hill is a mountain or a hill, our responsibility to the future cannot be denied and goes beyond definitions. Ultimately, whether we cared enough to succeed (who cares wins) will be measured by future generations when they come down from either a hill or a mountain. The words of Lyndon B. Johnson (36th American President) eloquently sum up what we want to achieve through the principles of ESG: *'If future generations are to remember us more with gratitude than sorrow, we must achieve more than just the miracles of technology. We must also leave them a glimpse of the world as it was created, not just as it looked when we got through with it.'*

I.J. Geldenhuys
President, SAIMM

Obituary

Darius Muma

26 September 1976 - 20th October 2021



Darius Muma graduated from the University of Zambia (UNZA) in 2004 with a BSc Chemistry degree. He worked as an Environmental Project Assistant at UNZA School of Mines with the Advocacy for Environmental Restoration Zambia (AREZ), before joining Konkola Copper Mines (KCM) Nchanga Mine in Chingola as a Graduate Chemist. He remained with KCM for 8½ years, progressing through the ranks to Senior Chemist, Sectional Chemist, and Acting Head of Analytical Services. During this time he gained a Diploma in Business Management (Association of Business Executives, UK). In February 2014 Darius moved to Mopani Copper Mines Mufulira Mine to take up a position of Assistant Superintendent: Analytical Services. the position he held when he passed on.

Darius was very keen in advancing his scope in the science field, resulting in his obtaining several educational and professional postgraduate qualifications. While at Mufulira, he completed a Bachelor of Education in Environmental Education at UNZA, and an MSc in Sustainable Mineral Resource Development under the Education for Sustainable Development in Africa (ESDA) joint programme of the University of Cape Town's Faculty of Engineering and Built Environment and the UNZA School of Mines.

Darius had a wide range of specialized skills and training in mineral sampling and assaying, including X-ray fluorescence, fire assay and related pyrometallurgical analysis techniques, laboratory auditing, chemometrics and intelligent laboratory systems, metallurgical accounting, and laboratory information management systems and project management. He was a BSI Certified Auditor for BSI ISO 14001 and Lead Auditor for BSI ISO 9001.

He was a Member of the SAIMM and the Chairperson of the SAIMM Zambia Branch since 2015. He was also the Northern Region Vice President of the Chemical Society of Zambia, an organization tasked with building, entrenching, and promoting chemistry and its application in Zambia, and a student member of ABE, UK.

Darius initiated a number of professional and education programmes which have benefited many. He will be greatly missed by his colleagues and the chemistry fraternity.

Darius is survived by his wife Priscilla, and his three children; Martin, Precious, and Gracious.

O. Mahenga
S. Moolla



The effect of non-standard loading platen usage on point load index value of rocks

by D. Akbay¹ and R. Altındağ²

Affiliation:

¹Çanakkale Onsekiz Mart University, Çan Vocational School, Department of Mining and Mineral Extraction, Çan, Çanakkale, Turkey.

²Süleyman Demirel University, Faculty of Engineering, Department of Mining Engineering, Isparta, Turkey.

Correspondence to:

D. Akbay

Email:

denizegeakbay@hotmail.com

Dates:

Received: 2 Feb. 2021

Revised: 1 Apr. 2021

Accepted: 13 Oct. 2021

Published: November 2021

How to cite:

Akbay, D. and Altındağ, R. 2021 The effect of non-standard loading platen usage on point load index value of rocks . Journal of the Southern African Institute of Mining and Metallurgy, vol. 121, no. 11, pp. 565–572

DOI ID:

<http://dx.doi.org/10.17159/2411-9717/1502/2021>

ORCID:

D. Akbay
<https://orcid.org/0000-0002-7794-5278>

R. Altındağ

<https://orcid.org/0000-0002-5397-7312>

Synopsis

The point load index is a simple, fast, and inexpensive method for determining rock strength and can be applied both in the field and in the laboratory. There are, however, some disadvantages and limitations to the method, and the test results can be affected by the person carrying out the test, the rock characteristics, or the test device. In this study we describe an investigation into how the point load index value is affected by the shape of the conical platens used in the test. Point load index tests were carried out using different devices fitted with conical platens of different spherical radii, and on a modified device which circumvented the limitations/disadvantages. It was seen that the point load index value increased as the platen radius increased, as expected. In the case of testing using non-standard conical platens, an equation is proposed to normalize the point load index value with respect to the standard spherical radius value.

Keywords

point load strength index, rock strength, limitations, test device.

Introduction

The point load index (PLI) is regarded as a valuable index test that gives a good initial indication of the rock strength in rock mechanics. The PLI test is simple, fast, and inexpensive. One of the biggest advantages of the PLI test is that it can be applied to irregular samples in the field. Many researchers have carried out detailed studies on the PLI test procedure, the effect of different loading configurations, sample size and shape, *etc.* During these studies, some limitations and errors associated with PLI devices have been identified. To date, these limitations and errors have been neglected in studies related to PLI because the purpose of the test is to find only an index value. However, the results of studies related to PLI demonstrate how important testing is in determining the strength of rocks, especially if the samples cannot be prepared to the required size for the uniaxial compressive strength (UCS) test. In such cases, the PLI test is inevitably used to determine the strength of the rocks.

The first studies related to the PLI are based on studies conducted to determine the tensile strength (TS) of rocks (Hiramatsu and Oka 1966; Reichmuth 1967; Franklin, Broch, and Walton, 1971). The method that was later developed by Broch and Franklin (1972) is still in use today. When the related literature is examined, it is seen that many studies examine the relationship between PLI and the physical and mechanical properties of rocks. The PLI has been the most researched test method for indirectly estimating the UCS of rocks (Bieniawski 1974, 1975; Bowden, Lamont-Black, and Ulliyott 1998; Hawkins 1998; Rusnak and Mark 2000; Tsiambaos and Sabatakakis 2004; Akram and Bakar 2007; Sundara 2009; Singh, Kainthola, and Venkatesh, 2012; Alitalash, Mollaali, and Yazdani, 2015; Elhakim 2015; Karaman, Kesimal, and Ersoy, 2015; Sheshde and Cheshomi 2015; Armaghani *et al.*, 2016; Ferentinou and Fakir 2017; Kabilan, Muttharam, and Elamathi. 2017). Researchers have also carried out studies to estimate both UCS and TS using the PLI (Wijk, Reh binder, and Lögdstrom, 1978; Panek and Fannon 1992; Butenuth 1997; Heidari *et al.*, 2012; Li and Wong 2013; Khanlari, Rafiei, and Abdilor, 2014; Momeni *et al.*, 2015; Minaeian and Ahangari 2017).

Many studies have been done on the relationships between the point load strength and some physical and mechanical properties of rocks. However, there are very few studies investigating the limitations and errors of the PLI test (Aston, MacIntyre, and Kazi, 1991; Topal 2000; Akbay and

The effect of non-standard loading platen usage on point load index value of rocks

Altindag 2020). Aston, MacIntyre, and Kazi (1991) investigated the effect of worn and chipped conical platens used in PLI test devices on the PLI value. In the tests, they used concrete samples to represent a medium-hard sandstone. To assess the effect of wear (well-worn and chipped platens), a pair of conical platens were ground down to give a surface contact area 16 times greater than new ex-factory conical platens. Another pair of conical platens had 50% of the tip removed. Aston, MacIntyre, and Kazi determined that the PLI values obtained from the worn conical platens were approximately 40% higher than the values obtained from the standard conical platens, and the values obtained from the chipped conical platens were about 30% lower than from the standard platens.

In this study, we aimed to determine the effect of the conical platens spherical radius (r) on PLI value. PLI tests were carried out on 13 different test devices using conical platens with different spherical radius values between 2.2 and 6.2 mm. Further tests were carried out using a modified PLI test device that eliminated the effect of all variables except platen shape on the test result, with platens of $r = 3$ mm, 5 mm, and 5.5 mm. The modified test device is computer-controlled where the loading is automatic, thus eliminating the human factor from the tests. The test device and all its associated apparatus has been technically checked for compliance with the relevant standards. By this means it was possible to determine the specific effect of the conical platen on the PLI value. The tests were carried out on seven different rock types (three sedimentary, one metamorphic, and three igneous).

Point load index

The PLI test is based on breaking the specimen by compressing it between a pair of spherical conical platens. Specimens in the form of cores, blocks, or irregular lumps can be used (Figure 1). The specimen dimensions and limits are clarified in detail in the methods published by the International Society for Rock Mechanics and Rock Engineering (ISRM, 1985) and American Society for Testing and Materials (ASTM, 1995).

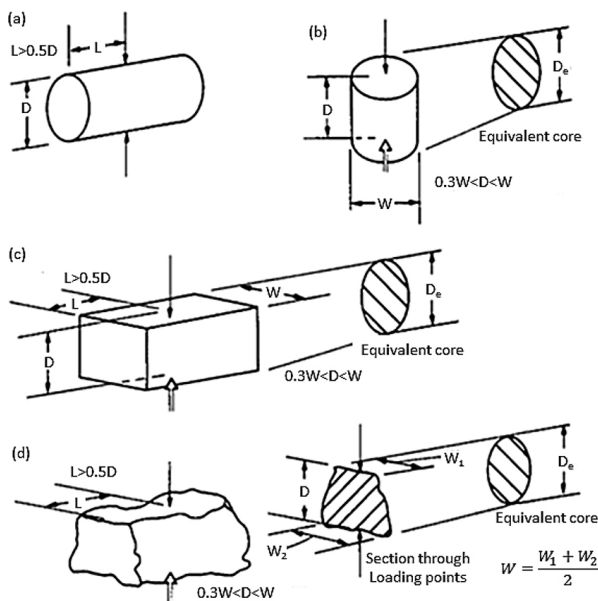


Figure 1—Specimen dimensions and limits for (a) diametral test specimen, (b) axial test specimen, (c) block specimen, and (d) an irregular lump (ISRM, 1985; ASTM, 1995)

In this study, block specimens were used. Blocks of 50 ± 35 mm size are suitable for testing. The D/W ratio should be between 0.3 and 1.0. Rock failure should occur within 10–60 seconds for the test to be considered valid. Valid and invalid failure modes are depicted in Figure 2 (ISRM 1985; ASTM 1995).

Preferably, at least 10 tests should be done per sample. If the sample is heterogeneous or anisotropic, more tests can be done. After the test is completed, the uncorrected PLI is calculated as follows:

$$I_s = \frac{P}{D_e^2} \quad [1]$$

where

P = failure load, N

D_e = equivalent core diameter = D for diametral tests, m

$D_e^2 = D^2$ for cores, mm^2

$D_e^2 = 4A/\pi$ for axial, block, and irregular lumps, mm^2

$A = W \times D$ minimum cross-sectional area of a plane through the platen contact points (Figure 1).

I_s changes as the function of D in the diametral test and the function of D_e in the axial, block, and irregular lump tests. Thus, a size correction must be applied to obtain a unique point load strength value for the rock sample that can be used for rock strength classification. Therefore, the I_s value should be corrected for a standard core diameter ($D = 50$ mm). The size correction can be calculated using the following formula:

$$I_{s(50)} = F \times I_s \quad [2]$$

where

I_s = Uncorrected point load strength value

F = Size correction factor.

F can be obtained from the expression:

$$F = \left(\frac{D_e}{50}\right)^{0.45} \quad [3]$$

The average value of $I_{s(50)}$ should be calculated by discarding the two highest and two lowest values obtained from ten valid tests and by calculating the average of the remaining six values. If fewer samples are tested, only the highest and lowest values are discarded (ISRM 1985; ASTM 1995).

PLI test device

The most widely used (classical) PLI test devices consist of a

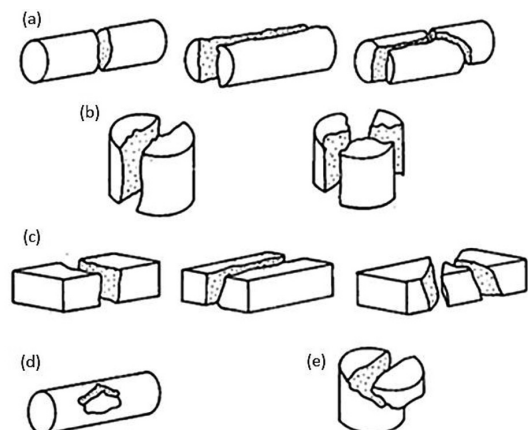


Figure 2—Failure modes for valid tests (a, b, c) and invalid tests (d, e) (ISRM, 1985; ASTM, 1995)

The effect of non-standard loading platen usage on point load index value of rocks

loading system (hydraulic piston), loading (pressure) gauge, and conical platens (Figure 3). The 60° cone and 5 mm radius spherical conical platens should be used (Figure 4). The platens shall be of hard material (Rockwell 58 HRC) such as tungsten carbide or hardened steel (ISRM, 1985; ASTM, 1995) so they remain undamaged during testing. The use of non-standard conical platens causes the results of the test to differ from the actual value. If a conical platens' tip has a spherical radius of more than 5 mm, it is expected the PLI will be higher than normal, otherwise, lower. The degree of influence is unknown and difficult to predict.

To determine the degree of influence of the spherical radius of the conical platen, a modified PLI test device was used in this study to circumvent the well-known limitations and errors of the classical PLI test device (Figure 5). The modified PLI device was manufactured with the ability to perform computer-controlled automatic loading according to the test conditions and standards recommended by the ISRM (1985) and ASTM (1995). The loading process is computer-controlled to ensure that the conical platen is the only variable. Thus, discrete loading and the effect of the user are eliminated. Each rock sample was tested using three different conical platens, and the influence of the platen spherical radius on the PLI determined.

Materials and method

The cone angle, spherical radius, and hardness of conical platens

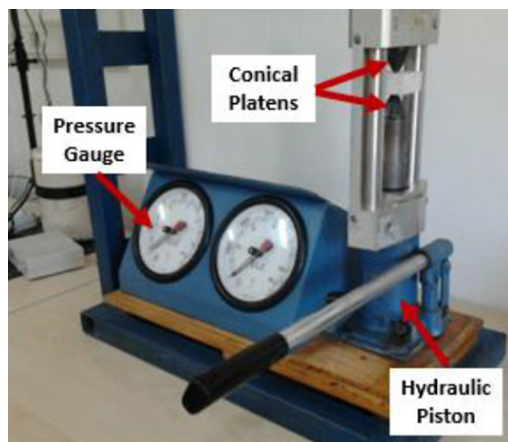


Figure 3—Example of a conventional PLI test device

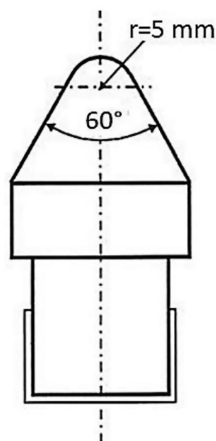


Figure 4—Platen dimensions suggested by the ISRM (1985) and ASTM (1995)

of 13 different PLI test devices were measured. The 60° cone and 5 mm spherical radius conical platens should be used in the PLI test method (ISRM, 1985; ASTM, 1995) and as shown in Figure 4. To control this, a simple mechanism was designed in the laboratory. The platens were placed on this mechanism so that the axis was horizontal and photographed from vertically above. The cone angles and the spherical radius values were measured by AutoCAD. Hardness values of the platens were measured with a hardness tester in the test device. The angle and hardness values, presented in Table I, were almost the same as, or very close to, the standard values. Therefore, it was decided to investigate how the spherical radius value affected the strength value. The PLI tests were carried on the 13 different test devices on the same seven rock samples.

Seven different types of rocks were selected to represent a strength scale from low to high, and were supplied in the form of plates from various marble processing plants. Samples as homogenous as possible were selected (Table II). To avoid variations in the test results caused by depth, the specimens were prepared from the 30 mm thick plates obtained from the rock block in the horizontal direction (Figure 6). The specimens were prepared with the dimensions (50 × 50 × 30 mm) and volume (75 cm³) specified in ISRM (1985), taking into account their planar position. For each pair of conical platens, 10 specimens were prepared from each rock sample. Diagonal lines were drawn on the prismatic specimens to ensure loading at the midpoint (Figure 7).

To determine the effect of the spherical radius (r) of the conical platens on the PLI, the PLI tests were performed on the

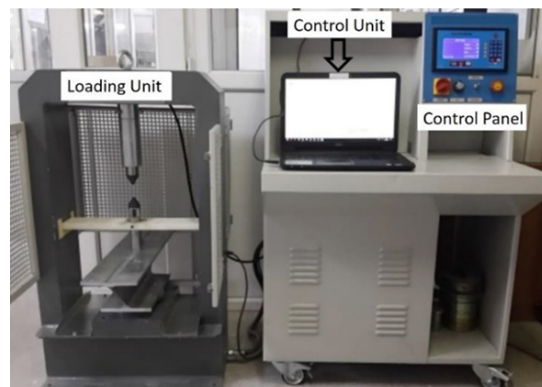


Figure 5—The modified PLI test device (Akbay, 2018)

Table I

The measured characteristics of the devices

Device No.	Radius (mm)	Cone angle (°)	Hardness (HRc)
1	5.8	60	63
2	5.2	61	59
3	2.2	60	53
4	6.2	61	59
5	4.4	63	56
6	5.9	60	51
7	5.6	60	64
8	4.0	63	57
9	5.6	60	61
10	5.6	61	60
11	5.0	60	58
12	3.9	60	63
13	5.4	61	62

The effect of non-standard loading platen usage on point load index value of rocks

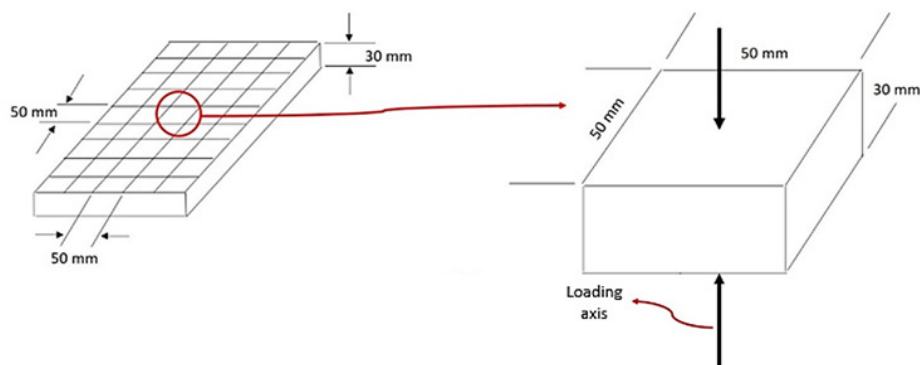


Figure 6—Preparation of specimen from the plates

Table II

Geological type and sources of the rocks used in the study

Sample	Sample code	Type	Source
Limestone-1	L-1	Sedimentary	Isparta
Limestone-2	L-2	Sedimentary	Isparta
Limestone-3	L-3	Sedimentary	Antalya
Marble	M	Metamorphic	Muğla
Andesite	A	Igneous	Isparta
Granite	G	Igneous	Aksaray
Diabase	D	Igneous	Kayseri

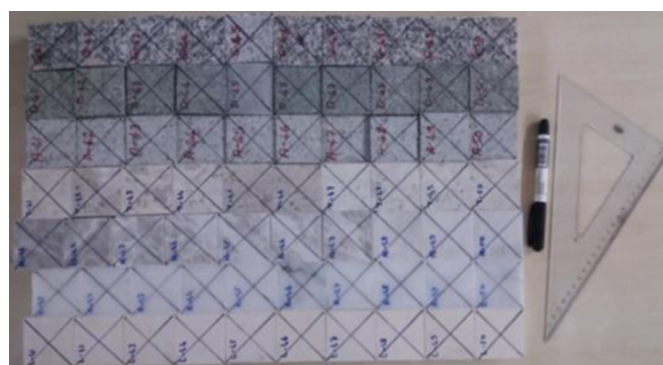


Figure 7—A group of specimens prepared for PLI tests

same samples in the modified device using three different pairs of conical platens with different spherical radius values ($r = 3$ mm, 5 mm, and 5.5 mm) (Figure 8). The cone angle, spherical radius, and hardness values of the conical platens are given in Table III. The only difference between the conical platens was the spherical radius value.

Results

Physical and mechanical properties of rock samples

The physical and mechanical properties of the rocks used in this study were determined according to the standards suggested by the ISRM and the Turkish Standards Institute (TSE). Unit volume weight (TS EN 1936 2010), water absorption percentage by weight (TS EN 13755 2014), apparent and total porosity (TS EN 1936 2010), density (TS EN 1936 2010), seismic velocity (TS EN 14579 2006), and uniaxial compressive strength (TS EN 1926 2013) tests were performed in the laboratory. At least 10 samples were used in the tests and the results calculated by taking the

arithmetic average of these 10 values. The results are given in Table IV.

PLI tests on different test devices fitted with conical platens of different spherical radii

PLI tests were carried out on different PLI test devices fitted with conical platens with different spherical radius values. The results are presented in Table V. The distribution of PLI values corresponding to the spherical radii was plotted and the relationships between them examined. Correlation coefficients of the relationships were determined by adding trend lines. There is no significant relationship between the PLI value and the spherical radius of the conical platen. However, when the situations where the spherical radius is smaller or greater than the standard value are evaluated separately, it is noticed that there are significant relationships between PLI and the spherical radius (Figures 9–15). The tests were carried out by the same operator and the test specimens were prepared from the same rock samples. This means the failure mechanism changes with radii less than or greater than 5 mm, but this change cannot be explained by the change in radius alone because the uncontrollable machine parameters and rock properties that affect the PLI value are ignored here. The correlation coefficients (r) are under 0.50 for the L-2 and M samples. This is probably due to geological defects in the rocks.

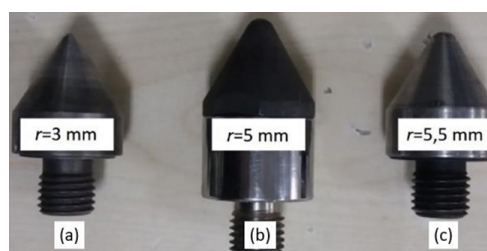


Figure 8—Conical platens with different spherical radii

Table III

Specifications of the conical platens

Platen code	Radius (mm)	Cone angle (°)	Hardness (HRC)
(a)	3.0	60	>58
(b)	5.0	60	>58
(c)	5.5	60	>58

The effect of non-standard loading platen usage on point load index value of rocks

Table IV

Physical and mechanical properties of rock samples

Sample code	d_0 (g/cm ³)		UVW (g/cm ³)		WAW (%)	AP (%)	TP (%)	V_p (m/s)		σ_c (MPa)	
	μ	SD	μ	SD	μ	μ	μ	μ	SD	μ	SD
L-1	2.770	0.007	0.124	0.053	0.343	0.148	0.484	6627	38	110.6	11.1
L-2	2.851	0.009	1.173	0.119	3.183	0.313	4.788	5456	688	103.9	12.3
L-3	2.734	0.005	2.375	0.290	6.081	0.720	9.311	5038	451	64.2	10.8
M	2.725	0.002	0.076	0.015	0.206	0.040	0.440	6144	723	72.1	5.0
A	2.608	0.002	3.281	0.297	7.552	0.632	11.704	4875	91	102.4	11.5
G	2.673	0.005	0.218	0.004	0.576	0.011	1.082	5367	156	154.0	8.6
D	2.994	0.012	0.656	0.076	1.902	0.204	3.011	5101	152	144.5	15.8

d_0 : density; UVW: unit volume weight; WAW: water absorption percent by weight; AP: apparent porosity; TP: Total porosity; V_p : seismic velocity; σ_c : uniaxial compressive strength

Table V

PLI values obtained from test devices fitted with conical platens with different spherical radius values

Device no.	Radius (mm)	L-1	L-2	L-3	M	A	G	D
1	5.8	4.33	2.87	3.96	3.04	6.69	6.75	8.26
2	5.2	3.08	2.35	2.83	2.72	4.64	5.82	6.92
3	2.2	3.11	2.53	3.01	2.77	4.59	5.47	6.7
4	6.2	5.1	4.95	4.56	3.59	7	8.08	9.1
5	4.4	3.59	3.45	3.79	2.76	5.71	6.38	7.25
6	5.9	4.34	3.17	4.73	3.79	7.44	8.04	9.21
7	5.6	3.9	3.85	4.03	2.2	6.23	7.36	8.44
8	4.0	3.18	2.37	3.98	2.4	5.16	5.55	7.14
9	5.6	4.78	3.51	3.87	3.29	6.42	7.01	8.74
10	5.6	4.74	4.58	4.44	3.52	7.06	7.53	8.76
11	5.0	3.55	3.97	3.26	3.08	4.55	5.98	6.05
12	3.9	4.08	3.15	3.72	2.92	5.76	6.05	7.58
13	5.4	3.82	2.79	4.26	2.63	4.89	5.9	7.71
Average	4.99	3.97	3.35	3.88	2.98	5.86	6.61	7.84

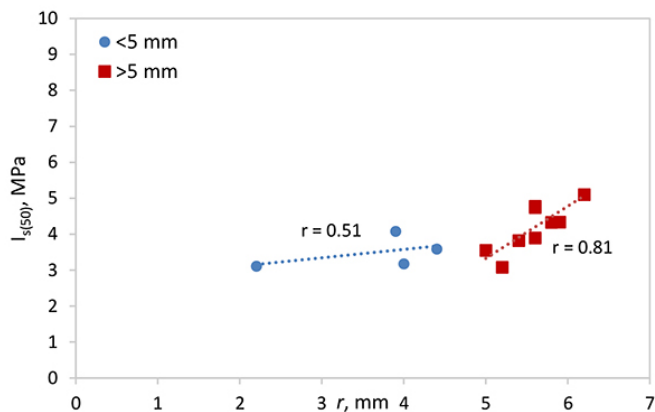


Figure 9—PLI values of sample L-1 vs. spherical radius of conical platen

Effect of the conical platen's spherical radius (r) on PLI value

The PLI values obtained from the modified PLI test device are plotted against the radius values in Figure 16. It is seen that the PLI increases as the spherical radius increases. The slope values (m_r) of the trend lines in Figure 16 were determined to ascertain by how much the PLI values for the various rock types were affected by the change in the spherical radius of the platen (Table III). The ratios of the PLI values obtained from the tests using different conical platens to the values obtained with the standard platen are given in Table VI. A 0.5 mm change (increase

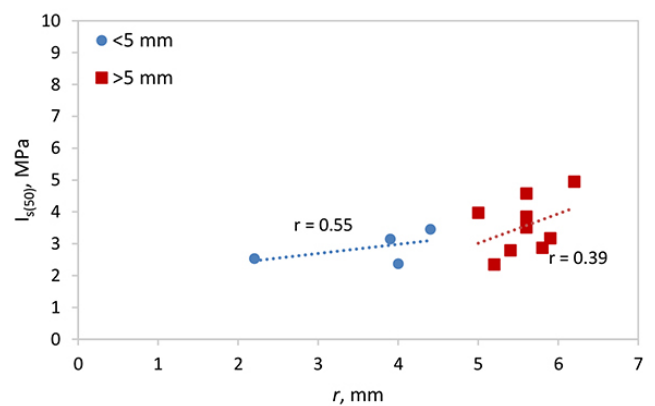


Figure 10—PLI values of sample L-2 vs. spherical radius of conical platen

or decrease) in the radius of the conical platen changed the strength value of the rock by 4%. The slope values indicate that the change in the radius of the platen had the most effect on the PLI value of the G-coded sample, and the least on the M-coded sample.

In the case of testing using conical platens with spherical radius values other than 5 mm, an equation is proposed to normalize the PLI values according to $r = 5$ mm (Equation [4]). The values obtained from the PLI tests and the normalized values are given in Table VII. Figure 16 shows a graph of the PLI values obtained from the tests using $r = 5$ mm platens corresponding

The effect of non-standard loading platen usage on point load index value of rocks

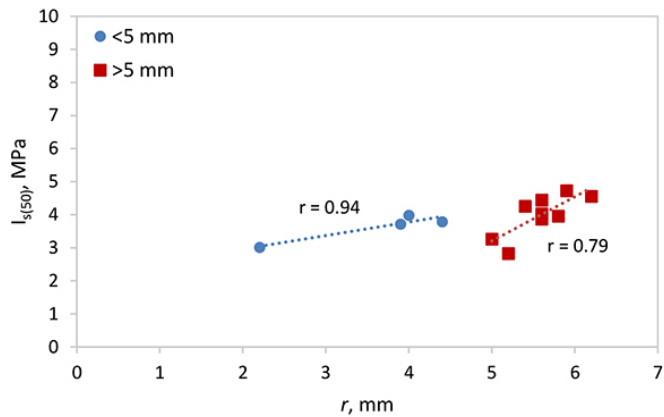


Figure 11—PLI values of sample L-3 vs. spherical radius of conical platen

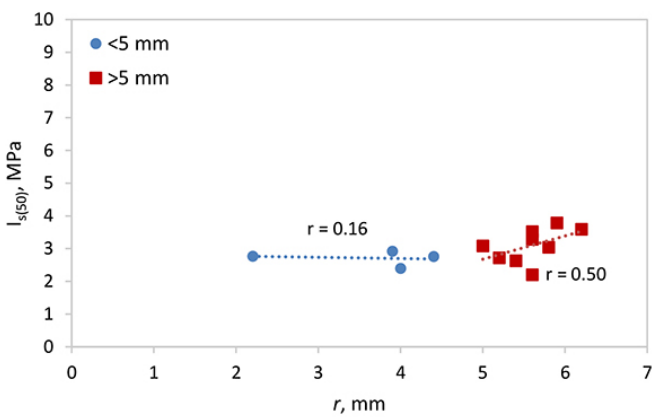


Figure 12—PLI values of sample M vs. spherical radius of conical platen

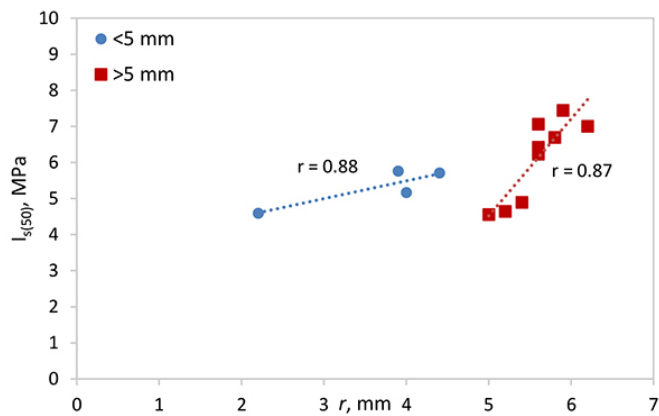


Figure 13—PLI values of sample A vs. spherical radius of conical platen

with the normalized PLI values from the tests using $r = 3$ mm and $r = 5.5$ mm platens. The PLI values using platen $r = 5$ mm and normalized PLI values using platens $r = 3$ mm and $r = 5.5$ mm were examined and a strong linear relationship was determined between them.

$$I_{s(50)r5} = I_{s(50)r_i} \times \left(1 - \frac{r_i - 5}{0.1}\right) \times 0.008 \quad [4]$$

where

$I_{s(50)r5}$ = Normalized PLI value according to spherical radius $r = 5$ mm, MPa

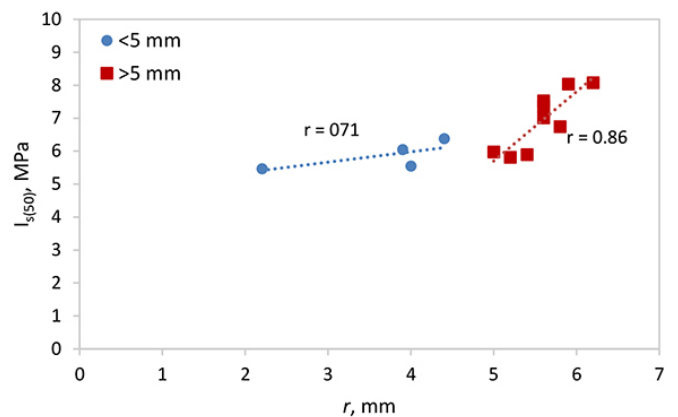


Figure 14—PLI values of sample G vs. spherical radius of conical platen

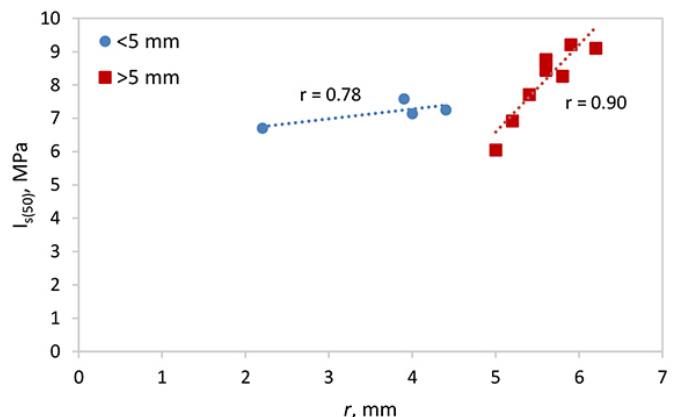


Figure 15—PLI values of sample D vs. spherical radius of conical platen

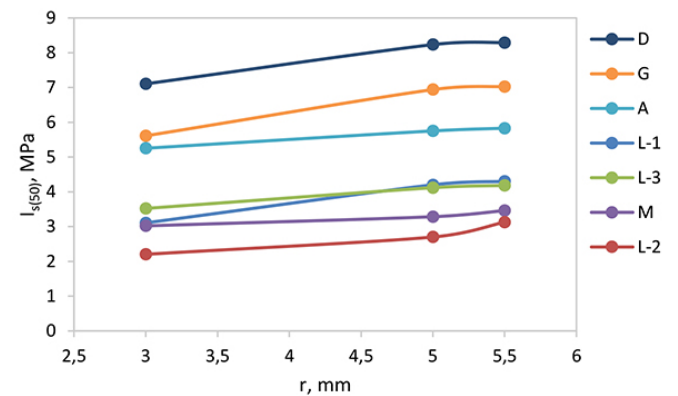


Figure 16—PLI values obtained from the modified PLI test device vs. spherical radius of conical platen

$I_{s(50)r_i}$ = PLI value for spherical radius $r \neq 5$ mm ($r < 5$ mm or $r > 5$ mm), MPa

r_i = Spherical radius value of conical platen, mm

In this study, each conical platen was used to break 70 rock specimens. The cone angle, spherical radius, and hardness of the conical platens were measured both before and after the tests. Table VIII show that there was no change in the measured properties of the conical platens.

Conclusions

PLI tests were carried out on the same rock samples using different test devices fitted with conical platens with different

The effect of non-standard loading platen usage on point load index value of rocks

Table VI

PLI results obtained from tests performed with different conical platens, and slope values obtained from Figure 16

Sample code	r = 3 mm		r = 5 mm $I_{s(50)}$ (MPa)	r = 5.5 mm		Slope value (m) (%)
	$I_{s(50)}$ (MPa)	Difference compared to r = 5 mm (%)		$I_{s(50)}$ (MPa)	Difference compared to r = 5 mm	
K-1	3.13	-25.8	4.22	4.32	2.3	0.496
K-2	2.23	-19.2	2.76	3.15	12.4	0.339
K-3	3.55	-14.3	4.14	4.21	1.7	0.273
M	3.04	-8.2	3.31	3.48	4.9	0.164
A	5.27	-8.7	5.77	5.85	1.4	0.237
G	5.63	-19.1	6.96	7.05	1.3	0.596
D	7.13	-13.6	8.25	8.31	0.7	0.497

$I_{s(50)}$: point load strength index; m_i : slope value; r : spherical radius of conical platen

Table VII

Comparison of uncorrected and normalized PLI values

Sample code	r = 3 mm		r = 5 mm $I_{s(50)}$ (MPa)	r = 5.5 mm	
	$I_{s(50)}$ (MPa)	$I_{s(50)r5}$ (MPa)		$I_{s(50)}$ (MPa)	$I_{s(50)r5}$ (MPa)
K-1	3.13	3.63	4.22	4.32	4.15
K-2	2.23	2.59	2.76	3.15	3.02
K-3	3.55	4.12	4.14	4.21	4.04
M	3.04	3.53	3.31	3.48	3.34
A	5.27	6.11	5.77	5.85	5.62
G	5.63	6.53	6.96	7.05	6.77
D	7.13	8.27	8.25	8.31	7.98

$I_{s(50)}$: point load strength index; $I_{s(50)r5}$: normalized point load strength index according to $r = 5$ mm; r : spherical radius of conical platen

Table VIII

Specifications of conical platens before and after the tests

Platen code	Before			After		
	r (mm)	A (°)	H (HRc)	r (mm)	A (°)	H (HRc)
(a)	3.0	60	>58	3.0	60	>58
(b)	5.0	60	>58	5.0	60	>58
(c)	5.5	60	>58	5.5	60	>58

r : spherical radius; A : cone angle; H : Rockwell hardness

spherical radii. There is no overall significant relationship between the PLI value and the spherical radius of the conical platen, but there are relationships between PLI and radius when radii of less than 5 mm and greater than 5 mm are considered separately. This indicates that the failure mechanism of the specimens changes, but this change cannot be explained by the radius alone, because there are variations in machine parameters and rock properties.

PLI tests were carried out on the same rock samples using a modified PLI test device, which is computer-controlled to eliminate the human factor (the loading is automatic), using three different pairs of conical platens with different spherical radii (3 mm, 5 mm, and 5.5 mm), to determine the effect of the spherical radius (r) of the conical platens on the PLI. The main conclusion arising from this study is that the PLI value increases as the spherical radius of the conical platen increases, but it is very difficult to determine the rate of this change. As the spherical radius decreases, the conical platen easily penetrates the rock sample and a lower PLI value is measured. As the r -value increases, the surface area of the platen in contact with the

sample increases and the platen encounters greater resistance, thus the PLI value measured is higher than the actual value. When the radius of the platen becomes too large (contact area), the system switches from point load strength to compressive strength, because the load is applied to an area rather than a point, and the test then loses its validity.

Each ± 0.1 mm change in radius value caused a change of $\pm 0.8\%$ in the value of the PLI according to the direction of change.

In the case of tests using conical platens with spherical radius values different from 5 mm, an equation is proposed to normalize the PLI values with respect to $r = 5$ mm.

The results of this study can be interpreted easily as slightly worn platens do not appear to alter the data significantly, especially when the data scatter due to different rock types is considered.

Breaking of a total of 210 rock samples did not cause any significant wear or damage to the conical platens in this study.

Acknowledgment

This study was supported by Süleyman Demirel University OYP Coordination Unit Project OYP-05286-DR-13 and the Scientific and Technological Research Council of Turkey (TUBITAK) Project 116R070. The authors thank TUBITAK and SDU OYP Project Coordination Unit.

Conflict of interest

The authors declare that they have no conflict of interest.

References

AKBAY, D. 2018. Designing A New Testing Apparatus For Preventing The Errors in Point Load Index Test. PhD thesis, Süleyman Demirel University, Turkey.

The effect of non-standard loading platen usage on point load index value of rocks

- AKBAY, D. and ALTINDAG, R. 2020. Reliability and evaluation of point load index values obtained from different testing devices. *Journal of the Southern African Institute of Mining and Metallurgy*, vol. 120, no. 3. pp. 181–190.
- AKRAM, M. and BAKAR, M.Z.A. 2007. Correlation between uniaxial compressive strength and point load index for salt-range rocks. *Pakistan Journal of Engineering and Applied Sciences*, vol. 1, no. 50. pp. 1–8.
- ALITALESH, M., MOLLAALI, M., and YAZDANI, M. 2015. Correlation between uniaxial strength and point load index of rocks. *Proceedings of the 15th Asian Regional Conference on Soil Mechanics and Geotechnical Engineering*. <https://doi.org/10.3208/jgssp.itm-08>
- ARMAGHANI, D.J., FOR, M., AMIN, M., YAGIZ, S., FARADONBEH, R.S., and ABDULLAH, R.A. 2016. Prediction of the uniaxial compressive strength of sandstone using various modeling techniques. *International Journal of Rock Mechanics and Mining Sciences*, vol. 85. pp. 174–186. <https://doi.org/10.1016/j.ijrmms.2016.03.018>
- ASTM. 1995. Standard test method for determination of the point load strength index of rock. *American Society for Testing and Materials*. <https://doi.org/10.1520/D5731-08.2>
- ASTON, T.R.C., MACINTYRE, J.S., and KAZI, H.A. 1991. The effect of worn and chipped points on point load indices. *Mining Science and Technology*, vol. 13. pp. 69–74.
- BIENIAWSKI, Z.T. 1974. Estimating the strength of rock materials. *Journal of the South African Institute of Mining and Metallurgy*, vol. 74, March. pp. 312–320. [https://doi.org/10.1016/0148-9062\(74\)91782-3](https://doi.org/10.1016/0148-9062(74)91782-3)
- BIENIAWSKI, Z.T. 1975. The point-load test in geotechnical practice. *Engineering Geology*, vol. 9, no. 1. pp. 1–11. <https://doi.org/10.1016/0013>
- BOWDEN, A.J., LAMONT-BLACK, J., and ULLYOTT, S. 1998. Point load testing of weak rocks with particular reference to chalk. *Quarterly Journal of Engineering Geology*, vol. 31. pp. 95–103. <http://citeseerx.ist.psu.edu/viewdoc/download?doi=10.1.1.967.5931&rep=rep1&type=pdf>
- BROCH, E. and FRANKLIN, J.A. 1972. The point-load strength test. *International Journal of Rock Mechanics and Mining Sciences*, vol. 9. pp. 669–697.
- BUTENUTH, C. 1997. Comparison of tensile strength values of rocks determined by point load and direct tension tests. *Rock Mechanics and Rock Engineering*, vol. 30. pp. 65–72.
- ELHAKIM, A.F. 2015. The use of point load test for Dubai weak calcareous sandstones. *Journal of Rock Mechanics and Geotechnical Engineering*, vol. 7, no. 4. pp. 452–457. <https://doi.org/10.1016/j.jrmge.2015.06.003>
- FERENTINOU, M. and FAKIR, M. 2017. An ANN approach for the prediction of uniaxial compressive strength, of some sedimentary and igneous rocks in eastern KwaZulu-Natal. *Procedia Engineering*, vol. 191. pp. 1117–1125. <https://doi.org/10.1016/j.proeng.2017.05.286>
- FRANKLIN, J.A., BROCH, E., and WALTON, G. 1971. Logging the mechanical character of rock. *Transactions of the Institution of Mining and Metallurgy*, vol. 80A. pp. 1–9.
- HAWKINS, A.B. 1998. Aspects of rock strength. *Bulletin of Engineering Geology and the Environment*, vol. 57, no. 1. pp. 17–30. <https://doi.org/10.1007/s100640050017>
- HEIDARI, M., KHANLARI, G.R., KAVEH, M.T., and KARGARIAN, S. 2012. Predicting the uniaxial compressive and tensile strengths of gypsum rock by point load testing. *Rock Mechanics and Rock Engineering*, vol. 45, no. 2. pp. 265–273. <https://doi.org/10.1007/s00603-011-0196-8>
- HIRAMATSU, Y. and OKA, Y. 1966. Determination of the tensile strength of rock by a compression test of an irregular test piece. *International Journal of Rock Mechanics and Mining Sciences & Geomechanics Abstracts*, vol. 3, no. 2. pp. 89–90.
- ISRM. 1985. Suggested method for determining point load strength. *International Journal of Rock Mechanics and Mining Sciences & Geomechanics Abstracts*, vol. 22, no. 2. pp. 51–60.
- KABILAN, N., MUTTHARAM, M., and ELAMATHI, V. 2017. Prediction of unconfined compressive strength for jointed rocks using point load index based on joint asperity angle. *Geotechnical and Geological Engineering*, vol. 35. 2625–2636. <https://doi.org/10.1007/s10706-017-0266-0>
- KARAMAN, K., KESIMAPP, I.A., and ERSOY, H. 2015. A comparative study of Schmidt hammer test methods for estimating the uniaxial compressive strength of rocks. *Bulletin of Engineering Geology and the Environment*, vol. 74, no. 8. pp. 2393–2403. <https://doi.org/10.1007/s10064-014-0617-5>
- KHANLARI, G., RAFIEI, B., and ABDILOR, Y. 2014. Evaluation of strength anisotropy and failure modes of laminated sandstones. *Arabian Journal of Geosciences*. pp. 3089–3102. <https://doi.org/10.1007/s12517-014-1411-1>
- LI, D. and WONG, L.N.Y. 2013. Point load test on meta-sedimentary rocks and correlation to UCS and BTS. *Rock Mechanics and Rock Engineering*, vol. 46, no. 4. pp. 889–896. <https://doi.org/10.1007/s00603-012-0299-x>
- MINAEIAN, B. and AHANGARI, K. 2017. Prediction of the uniaxial compressive strength and Brazilian tensile strength of weak conglomerate. *International Journal of Geo-Engineering*, vol. 8, no. 1. <https://doi.org/10.1186/s40703-017-0056-9>
- MOMENI, A.A., KHANLARI, G.R., HEIDARI, M., SEPAHI, A.A., and BAZVAND, E. 2015. New engineering geological weathering classifications for granitoid rocks. *Engineering Geology*, vol. 185. pp. 43–51. <https://doi.org/10.1016/j.enggeo.2014.11.012>
- PANEK, L. A. and FANNON, T.A. 1992. Size and shape effects in point load tests of irregular rock fragments. *Rock Mechanics and Rock Engineering*, vol. 25, no. 2. pp. 109–140. <https://doi.org/10.1007/BF01040515>
- REICHMUTH, D.R. 1967. Point load testing of brittle materials to determine tensile strength and relative brittleness. *Proceedings of the 9th U.S. Symposium on Rock Mechanics*, Golden, CO, 17–19 April 1967. American Rock Mechanics Association, Alexandria, VA. pp. 134–160.
- RUSNAK, J. and MARK, C. 2000. Using the point load test to determine the uniaxial compressive strength of coal measure rock. *Proceedings of the 19th International Conference on Ground Control in Mining*, Morgantown, West Virginia, 8–10 August 2000. West Virginia University. pp. 362–371.
- SHESHDE, E.A. and CHESHOMI, A. 2015. New method for estimating unconfined compressive strength (UCS) using small rock samples. *Journal of Petroleum Science and Engineering*, vol. 133. pp. 367–375. <https://doi.org/10.1016/j.petrol.2015.06.022>
- SINGH, T.N., KAINTHOLA, A., and VENKATESH, A. 2012. Correlation between point load index and uniaxial compressive strength for different rock types. *Rock Mechanics and Rock Engineering*, vol. 45, no. 2. pp. 259–264. <https://doi.org/10.1007/s00603-011-0192-z>
- SUNDARA, P.A. 2009. Correlation between uniaxial compressive strength and point-load index strength. <https://doi.org/10.1017/CBO9781107415324.004>
- TOPAL, T. 2000. Nokta yüklemeye deneyi ile ilgili uygulamada karşılaşılan problemler. *Jeoloji Mühendisliği*, vol. 24, no. 1. pp. 73–86.
- TS EN 13755, 2014. Natural stone test methods - Determination of water absorption at atmospheric pressure. TSE, Ankara.
- TS EN 14579, 2006. Natural stone test methods - Determination of sound speed propagation. TSE, Ankara.
- TS EN 1926, 2013. Natural stone test methods - Determination of uniaxial compressive strength. TSE, Ankara.
- TS EN 1936, 2010. Natural stone test methods - Determination of real density and apparent density and of total and open porosity. TSE, Ankara.
- TSIAMBAS, G. AND SABATAKAKIS, N. 2004. Considerations on strength of intact sedimentary rocks. *Engineering Geology*, vol. 72, no. 3–4. pp. 261–273. <https://doi.org/10.1016/j.enggeo.2003.10.001>
- WIJK, G., REHBINDER, G., and LÖGDSTRÖM, G. 1978. The relation between the uniaxial tensile strength and the sample size for bohus granite. *Rock Mechanics Felsmechanik Mecanique Des Roches*, vol. 10, no. 4. pp. 201–219. <https://doi.org/10.1007/BF01891959> ◆



Local magnitude calibration of seismic events in the West Rand, Far West Rand, and Klerksdorp–Orkney–Stilfontein–Hartebeesfontein gold mining areas

by M.B.C. Brandt

Affiliation:

¹Council for Geoscience
Engineering and Geohazards,
Unit, South Africa.

Correspondence to:

M.B.C. Brandt

Email:

mbrandt@geoscience.org.za

Dates:

Received: 29 Jul. 2021

Revised: 11 Oct. 2021

Accepted: 15 Oct. 2021

Published: November 2021

How to cite:

Brandt, M.B.C. 2021

Local magnitude calibration
of seismic events in the West
Rand, Far West Rand, and
Klerksdorp–Orkney–Stilfontein–
Hartebeesfontein gold mining
areas.

Journal of the Southern African
Institute of Mining and Metallurgy,
vol. 121, no. 11, pp. 573–580

DOI ID:

<http://dx.doi.org/10.17159/2411-9717/1301/2021>

Synopsis

Richter magnitudes for seismic events were calibrated for use as a Local magnitude scale in the West Rand (WR), Far West Rand (FWR), and Klerksdorp–Orkney–Stilfontein–Hartebeesfontein (KOSH) gold mining areas. Richter magnitudes are currently calculated from seismograms recorded by local surface cluster networks using tabulated calibration values for Southern California, published in 1958. The Richter (1958) model is incorrect for distances of less than 30 km and should be applied only to crustal earthquakes in regions with similar attenuation properties to those of Southern California. When compared to the South African National Seismograph Network (SANSN), the cluster networks, on average, overestimate seismic event magnitudes by approximately 0.1 of a magnitude unit. A calibrated Local magnitude scale was derived by means of a multiple regression analysis between the Local magnitudes reported by the SANSN and the largest zero-to-peak trace amplitudes measured on the cluster network horizontal seismograms, after modelling the attenuation of the seismic waves as these progress from the epicentre to the station position. Magnitudes reported by individual stations for the same event show a significant scatter around the average magnitude owing to the near-surface amplifications of the seismic waves at the recordings sites. Average magnitude should be estimated using as many magnitudes of individual stations as possible to ensure an accurate estimate. Larger event magnitudes should be compared with those recorded by the SANSN.

Keywords

Richter magnitude, local magnitude calibration, seismic event, Witwatersrand Basin.

Introduction

Magnitude in seismology is a concept that describes the size of a seismic event based on instrumental measurements of some kind. The first magnitude scale was introduced by Richter (1935) for Southern California, USA. This scale only requires the location of the seismic event to be known and the ground motion amplitudes to be recorded by a standard Wood-Anderson seismograph. The maximum zero-to-peak trace amplitudes of the earthquake signals are measured on both horizontal-component seismograms (NS and EW) and the magnitude is calculated using the greater of the two measurements. Richter (1935) quantified the scale as follows: *'The magnitude of any shock is taken as the logarithm of the maximum trace amplitude, expressed in microns, with which the standard short-period torsion seismometer... would register that shock at an epicentral distance of 100 km.'*

To calculate magnitudes for other distances, Richter (1958) provided tabulated attenuation corrections (calibration values) for distances from 0–600 km, assuming a focal depth of 18 km. Accordingly, Richter magnitude M_L is calculated using the equation:

$$M_L = \log_{10}(A_{\max}) - \log_{10}(A_0) \quad [1]$$

where A_{\max} is the largest measured zero-to-peak trace amplitude in millimetres on a Wood-Anderson recorded horizontal seismogram, A_0 represents the trace amplitudes in millimetres from an earthquake of $M_L=0$, and $-\log_{10}(A_0)$ represents the tabulated calibration values (Richter, 1958). Hutton and Boore (1987) derived the following parametric equation for the calibration values:

$$-\log_{10}(A_0(R)) = 1.11 \cdot \log_{10}(R) + 0.00189 \cdot R - 2.09 \quad [2]$$

where R is the hypocentral distance in kilometres.

Local magnitude calibration of seismic events in the West Rand, Far West Rand

In Equation [2], the largest trace amplitude is measured in nanometres on a synthetic seismogram recorded by a modern horizontal-component seismograph. The seismogram is filtered so that the response of the seismograph and filter system replicates that of a standard Wood-Anderson seismograph, but with a static $1 \times$ magnification. Modern synthetic seismograms more closely resemble the signal recordings than the actual standard Wood-Anderson seismograph because the manufacturer specifications for magnification published in the 1930s were found to be inaccurate (Uhrhammer and Collins, 1990).

Standard Equation [2] should be used when calculating Richter magnitudes for crustal earthquakes in regions with attenuation properties similar to those of Southern California. For regions with different attenuation properties, the standard equation is of the form:

$$M_L = \log_{10}(A_{\max}) + C(R) + D \quad [3]$$

where A_{\max} and R are the same as in Equations [1] and [2] and where $C(R)$ and D need to be calibrated to adjust for the different regional attenuation. The maximum amplitude may be measured on a vertical-component seismogram after adjusting for any systematic differences between the amplitudes recorded by the horizontal seismographs and the vertical seismographs (Bormann, 2012).

The South African national geological survey (the Council for Geoscience) is mandated to operate the South African National Seismograph Network (SANSN). A calibrated Richter magnitude scale, referred to as a Local magnitude scale, was derived using vertical-component seismographs for the SANSN (Saunders *et al.*, 2008; 2012):

$$-\log_{10}A_0(R) = 1.149 \cdot \log_{10}(R) + 0.00063 \cdot R - 2.04 \quad [4]$$

where A_0 and R are the same as before. Vertical-component maximum amplitudes were selected for continuity because, until the 1990s, the SANSN comprised mostly vertical-component seismometers. Dissimilarities in the coefficients for $\log_{10}(R)$ and R in Equations [2] and [4] reflect the different attenuation properties between Southern California and South Africa.

In addition to the SANSN, the Council for Geoscience also operates cluster networks of dense local, surface stations within the Far West Rand (FWR), West Rand (WR), Central Rand, and the Klerksdorp–Orkney–Stilfontein–Hartebeesfontein (KOSH) gold mining areas. The magnitudes reported by the cluster networks have not yet been calibrated. Richter magnitudes are currently calculated using Equation [1] and the tabulated values of Richter (1958) for Southern California. This causes discrepancies between the Local magnitudes reported by the SANSN and Richter magnitudes reported by the cluster networks. On average, the cluster networks overestimate seismic event magnitudes by approximately 0.1 of a magnitude unit. The seismograms recorded by the stations of the cluster networks are automatically processed and manually re-analysed using Antelope 5.4 software (2018). This software calculates Richter magnitudes with the largest zero-to-peak trace amplitudes measured on the horizontal-component seismograms with Equation [1], identical to the original method of Richter (1935). The calibration values in Equation [4] for the vertical-component seismograms of the SANSN that resemble a synthetic Wood-Anderson seismograph with a static magnification $1 \times$ can therefore not be simply transferred to the cluster network.

The purpose of this article is to derive tabulated calibration values for $\log_{10}(A_0)$ in Equation [1] for the cluster network horizontal components such that, on average, the Local magnitudes reported by the cluster networks have the same sizes as those reported by the SANSN. This will be accomplished by means of a multiple regression analysis between the Local magnitudes reported by the SANSN, the largest zero-to-peak trace amplitudes measured on the cluster network horizontal seismograms, where $-\log_{10}(A_0)$ is modelled using Equation [3] and where $C(R) + D$ have the same respective variables as in Equation [2].

Richter magnitudes currently reported by surface mine cluster networks

The Council for Geoscience operates three mine surface cluster networks, and the event origin times, epicentres and magnitudes may be obtained from the web page <<http://196.38.235.147:8070/livemines/>>. The mine and environmental water management programme (MEWMP) network consists of ten stations across the West, Central, and East Rand. The purpose of this network is to monitor seismicity that may be linked to the ingress of water into abandoned mines in and around the City of Johannesburg. The FWR network comprises 11 stations situated in the Carletonville region. The network was installed as part of a research project initiated by the Japanese International Cooperation Agency. The KOSH network consists of 19 stations installed in the Klerksdorp–Orkney–Stilfontein–Hartebeesfontein region, as part of a project sponsored by the Mine Health and Safety Council.

The positions of stations and the seismic events for the period 1 January 2019 to 19 June 2020 used in this study are shown in Figures 1 and 2. The tight clustering of seismic events detected by both the SANSN and the surface cluster network is an artefact of the event density; in other words, most of the events were located at the centre of the cluster. The Richter magnitudes in Figures 1 and 2 were calculated by means of Antelope 5.4 software (2018) using Equation [1] and the calibration values for $\log_{10}(A_0)$, listed in Table I. The calibration values in Table I, as well as those for Equations [2] and [4], are graphically depicted in Figure 3. Richter's equation for the tabulated calibration function $-\log_{10}A_0(\Delta)$ in Table I is derived (Figure 3) by means of a multiple regression analysis for an equation with the same variables as Equation [2]:

$$-\log_{10}A_0(\Delta) = 0.961 \cdot \log_{10}(\Delta) + 0.00272 \cdot \Delta + 0.00272 \cdot \Delta + 0.787 \quad R^2 = 0.983 \quad [5]$$

R^2 is the goodness-of-fit measure where $0 < R^2 < 1$ for the linear regression model, and 1 indicates a perfect fit.

There is a significant offset between the constant value 0.787 and the constants -2.09 and -2.04 in Equation [2] (Hutton and Boore, 1987) and Equation [4] (Saunders *et al.*, 2012), respectively. This is because Richter (1935) measured the largest trace amplitude in millimetres as recorded by a standard Wood-Anderson seismograph, whereas modern simulated Wood-Anderson seismograms have a static amplification of $\times 1$. Unit amplification implicitly means that true ground motion amplitudes in nanometres are measured for the recorded frequency range. Hutton and Boore (1987) updated the coefficients for $\log_{10}(R)$ and R in Equation [2] and determined that Richter's (1958) calibration values for near distance Δ

Local magnitude calibration of seismic events in the West Rand, Far West Rand

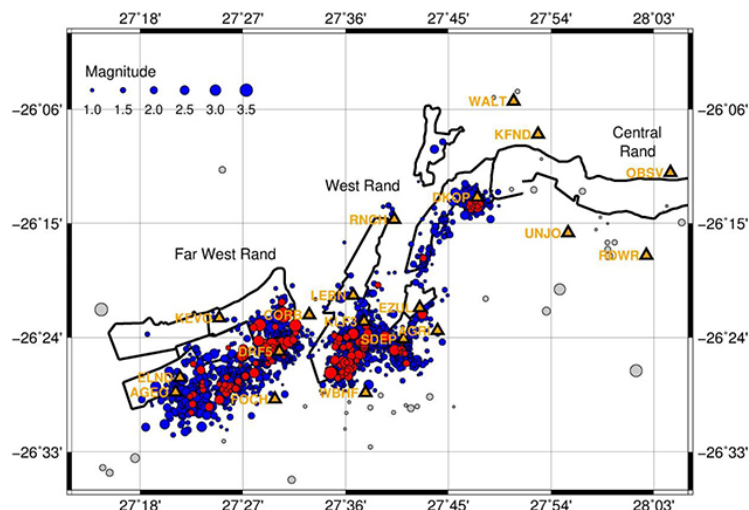


Figure 1—Map of seismograph stations around the WR and FWR and the western part of the Central Rand gold mining areas. Eleven triangles depict the stations of the FWR cluster network and eight triangles depict the WR and western Central Rand's stations of the MEWM cluster network. Station codes are listed in orange. Blue dots represent events from 2019 01 01 to 2020 06 19 located by the two cluster networks in the WR and FWR, and red dots represent events that were also detected by the SANSN. Events outside the mining areas that were rejected from this study are greyed out. Mines are delineated by thick, black lines

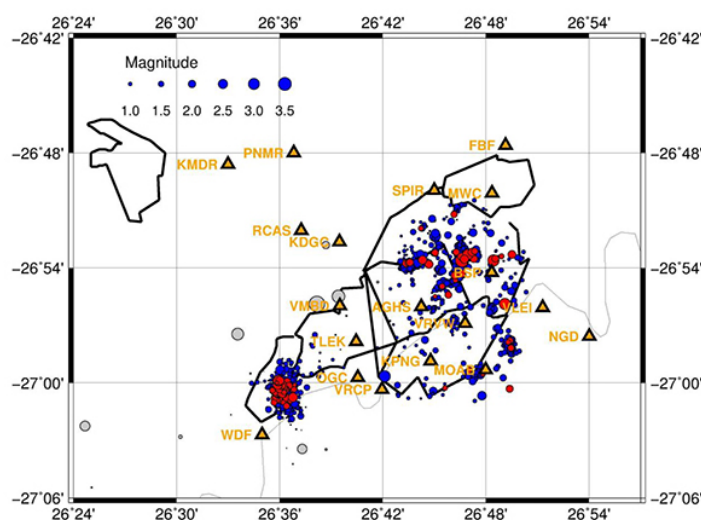


Figure 2—Map of seismograph stations around the KOSH area. The stations are depicted by nineteen triangles. Station codes are listed in orange. Blue dots represent events from 2019 01 01 to 2020 06 19 located by the cluster network in the KOSH area and red dots represent events that were also detected by the SANSN. Events outside the mining area that were rejected from this study are greyed out. Mines are delineated by thick, black lines and the Vaal River is depicted by a thin grey line

<30 km are incorrect (Figure 3). Bakun and Joyner (1984) drew the same conclusion for near-distance weak events recorded in Central California. Richter's 1958 calibration values causes magnitude estimates from nearby stations to be smaller than those from more distant stations (Bormann, 2012). Hutton and Boore (1987) further suggested deriving calibration values based on a shallow focal depth of 0 km for crustal earthquakes, as values measured in this way provide a better fit than those calculated using the 18 km focal depth proposed by Richter (1958).

An orthogonal regression between 256 Local magnitudes reported by the SANSN (Saunders *et al.*, 2012) and the Richter magnitudes reported by the surface cluster networks (Richter, 1958) in Figure 3 produces the equation:

$$M_L(\text{SANSN}) = 0.99 * M_L(\text{cluster}) - 0.12 \quad R^2 = 0.93 \quad [6]$$

where R^2 is defined as before. The cluster networks, on average, overestimate seismic event magnitudes by approximately 0.1 of a magnitude unit. Even though the goodness-of-fit is high and the 95% confidence level indicates a credible match, the scatter of the magnitudes around the best fit orthogonal relation is significant. The scatter is investigated in the histograms and bar graph in Figures 5 and 6. The differences between the Richter magnitudes observed by individual stations of the cluster networks and the average Richter magnitudes calculated for the respective seismic events have a standard deviation of 0.56 (Figure 5). The frequency bar graph in Figure 6 for stations with magnitude differences of more than 0.56 revealed incorrectly calibrated stations AGRI and ELND. The magnitude differences, excluding recordings from stations AGRI and ELND, have a standard deviation of only 0.48. The rejected magnitudes reported by AGRI and ELND cause the distribution of

Local magnitude calibration of seismic events in the West Rand, Far West Rand

Table I

Interpolated tabulated calibration function $-\log_{10}A_0(\Delta)$ to calculate Richter magnitudes using Antelope 5.4 software (2018). The classical values derived by Richter (1958) are shown in bold. A_0 represents the maximum horizontal trace amplitudes in millimetres recorded by a standard Wood-Anderson seismometer from an earthquake of $M_L=0$ at an epicentral distance of Δ km

Δ (km)	$-\log_{10}A_0(\Delta)$						
0	1.4	95	3.0	270	3.9	450	4.6
5	1.4	100	3.0	280	3.9	460	4.6
10	1.5	110	3.1	290	4.0	470	4.7
15	1.6	120	3.1	300	4.0	480	4.7
20	1.7	130	3.2	310	4.1	490	4.7
25	1.9	140	3.2	320	4.1	500	4.7
30	2.1	150	3.3	330	4.2	510	4.8
35	2.3	160	3.3	340	4.2	520	4.8
40	2.4	170	3.4	350	4.3	530	4.8
45	2.5	180	3.4	360	4.3	540	4.8
50	2.6	190	3.5	370	4.3	550	4.8
55	2.7	200	3.5	380	4.4	560	4.9
60	2.8	210	3.6	390	4.4	570	4.9
65	2.8	220	3.65	400	4.5	580	4.9
70	2.8	230	3.7	410	4.5	590	4.9
80	2.9	240	3.7	420	4.5	600	4.9
85	2.9	250	3.8	430	4.6		
90	3.0	260	3.8	440	4.6		

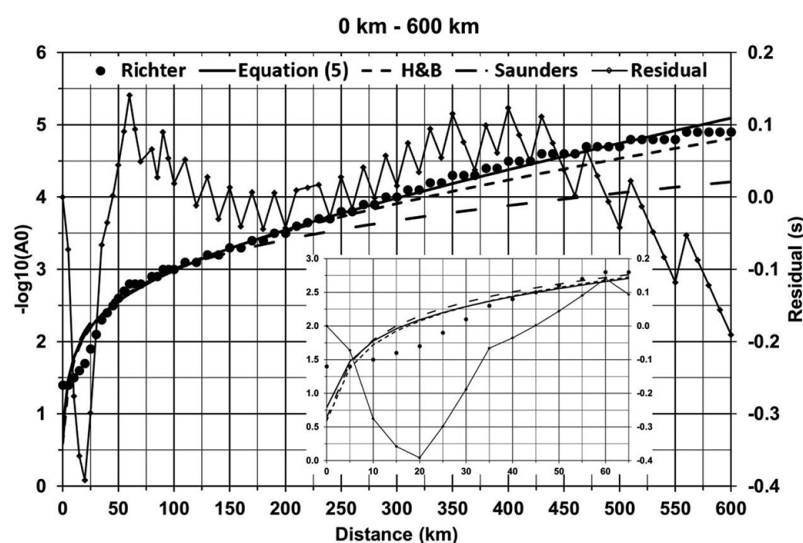


Figure 3—Richter's equation (Equation [5]) (thick solid curve, scale on the left axis) for the tabulated calibration function $-\log_{10}A_0(\Delta)$ in Table I (dots) derived by means of a multiple regression analysis for a model with the same respective variables as in Equation [2]. Residual values between $-\log_{10}A_0(\Delta)$ in Table I and Richter's equation are shown as thin dotted lines with scale on the right axis. This is compared to Equation [2] (Hutton and Boore, 1987), displayed as a short dashed curve and Equation [4] (Saunders et al., 2012), shown as a long dashed curve. Equations [2] and [4] are normalised to $-\log_{10}A_0(\Delta) = 3$ at 100 km distance for direct comparison with Equation [5]. Distances between zero and 65 km are enlarged at the bottom right

the histogram to become more symmetrical in regard to positive magnitude differences, especially for those >0.6 . However, magnitude differences <0.6 also decrease, indicating that stations AGRI and ELND were not malfunctioning throughout the whole study period. Hence, for the remainder of this article, only observations where the Richter magnitude difference is <0.56 will be used.

Next, we investigate whether the finding by Hutton and Boore (1987) and by Bakun and Joyner (1984), that Richter's (1958) calibration values for near distance $\Delta < 30$ km in California are incorrect, can be extrapolated to the WR, FWR, and KOSH mining areas. To accomplish this we plot the Richter magnitude differences (<0.56) as a function of distance in Figure

7. A comparison between the Richter magnitude differences and the residual values between $-\log_{10}A_0(\Delta)$ in Table I and Richter's equation (Figure 3) confirms that Richter's (1958) calibration values are indeed also incorrect for the WR, FWR, and KOSH mining areas for near distances. We conclude that the calibration values for $\log_{10}(A_0)$ should be modelled with Equation [3], where $C(R) + D$ have the same respective variables as in Equation [2]. However, calculating Richter magnitudes with incorrect calibration values for near distances of $\Delta < 30$ km is not the only cause of the large scatter in magnitudes around the best fit orthogonal relation in Figure 4 and the large scatter in the histogram of Richter magnitude differences (Figure 5). The rapid changes of the nine-point running average window

Local magnitude calibration of seismic events in the West Rand, Far West Rand

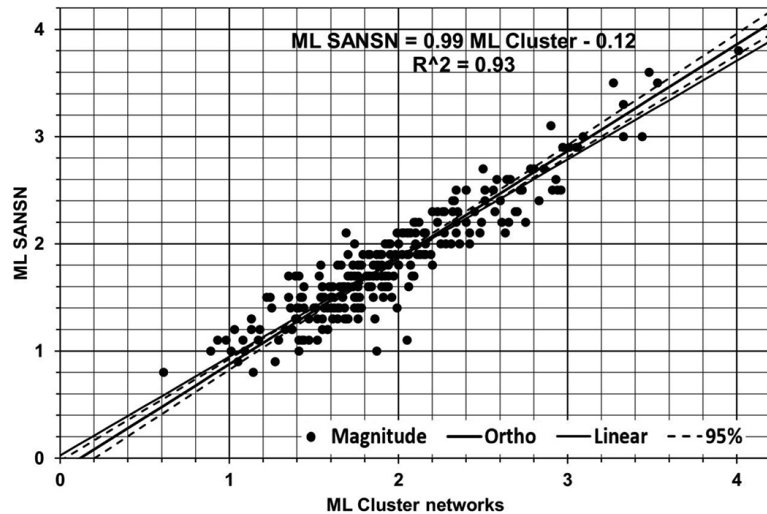


Figure 4—Local magnitudes in the WR, FWR, and KOSH areas reported by the SANSN (Saunders et al. 2012) as a function of Richter (1958) magnitudes reported by the surface cluster networks (dots). The seismic events plotted in this graph correspond to the red dots on the maps in Figures 1 and 2. The equation at the top fits the magnitudes by means of an orthogonal regression (thick line) with goodness-of-fit of 0.93 where the dashed curves represent the 95% confidence interval. This is compared with a linear regression (thin line)

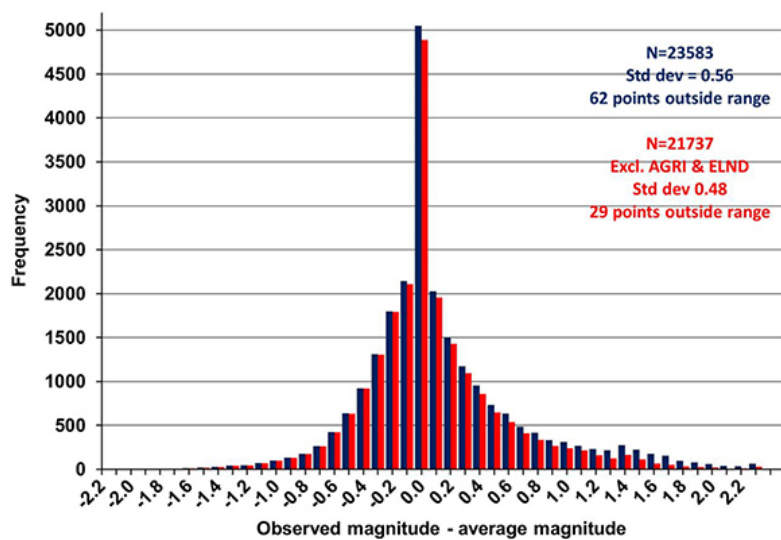


Figure 5—Histogram of the differences between Richter magnitudes observed by individual stations of the cluster networks and the average Richter magnitude calculated for the respective seismic events. The 23 583 magnitude differences used in this study (blue bars) have a standard deviation of 0.56. The 21 737 magnitude differences, excluding recordings from stations AGRI and ELND (red bars – and also see Figure 6) have a standard deviation of 0.48

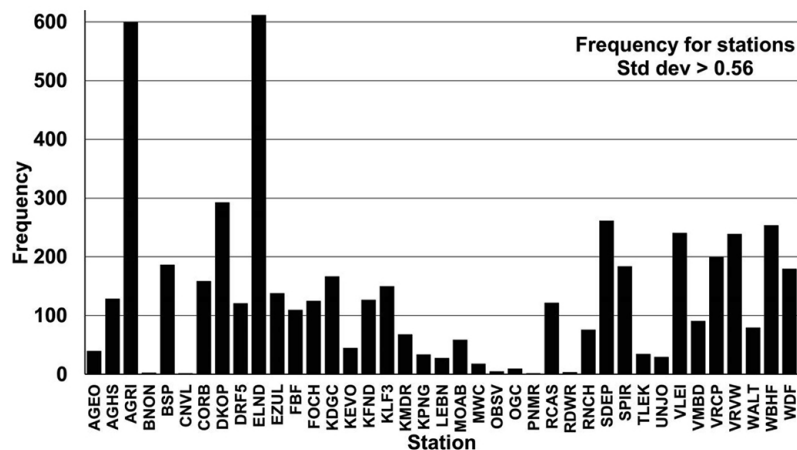


Figure 6 – Frequency of the stations (see maps in Figures 1 and 2, and Figure 5) with magnitude differences >0.56

Local magnitude calibration of seismic events in the West Rand, Far West Rand

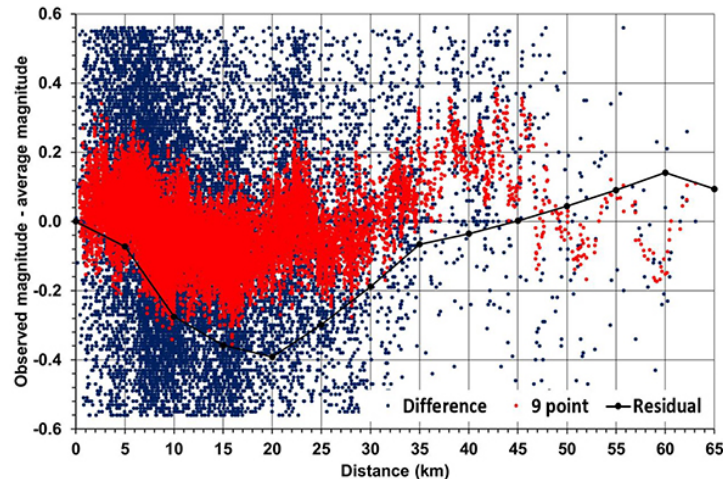


Figure 7—Differences between Richter magnitudes observed by individual stations of the cluster networks and the average Richter magnitude calculated for the respective seismic events as a function of distance (blue dots). Red dots represent a nine-point running average window of the magnitude differences and are compared to the residual values between $-\log_{10}A_0(\Delta)$ in Table I and Richter's equation (Figure 3), which is depicted as thin dotted lines. Richter magnitude differences of more than 0.56 have been excluded from the graph

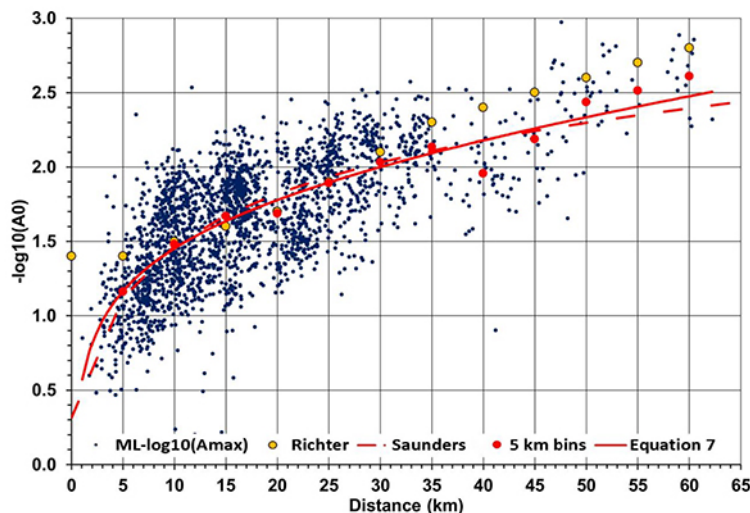


Figure 8—Newly derived calibration function $-\log_{10}A_0(\Delta)$ (red curve), specified in Equation [7] derived by means of a multiple regression for $-\log_{10}A_0(\Delta) = ML - \log_{10}(A_{max})$ (blue dots) for a model with the same variables as in Equation [2]. The average values of $-\log_{10}A_0(\Delta)$ in 5 km bins are shown as large, red dots and Richter's (1958) tabulated values, listed in Table I, as large, orange dots. This is compared with Equation [4] (Saunders et al., 2011), shown as a red, long dashed curve. The constant in Equation [4] was adjusted for an optimum least-squares fit to the values of $-\log_{10}A_0(\Delta)$

between about -0.18 and $+0.1$ at distances of 47 km, 51 km, 55 km and 59 km in Figure 7 indicate that neighbouring stations have observed significantly different magnitudes for the same seismic event. These rapid changes are not visible at shorter distances owing to the many observed magnitudes that plot on top of one another, but which probably also exist. These rapid changes provide evidence of near-surface amplifications where a seismometer has not been installed on competent bedrock. Bormann (2012) reports that the closely spaced stations of a seismic array may measure relative amplifications to one another in ground amplitudes of 10 to 30 times when installed on soft soil such as alluvium. Security is the primary criterion for the selection of a site to install a seismograph station in a mining area as a result of the high risk of theft or vandalism. Many of the seismometers are therefore not installed on competent bedrock, thus providing the option of relocating a station if the security situation worsens or if the host mine or landowner closes or suspends operations. However, magnitude differences

of >0.56 are likely the result of equipment malfunction or processing errors. Antelope 5.4 software (2018) rejects outliers when calculating the average magnitude, and weighs individual magnitude observations according to the signal-to-noise ratio of the maximum measured amplitude.

Local magnitude calibration

Calibration values for $-\log_{10}(A_0)$ in Equation [1] for the cluster networks are derived by means of a multiple regression analysis between the Local magnitudes reported by the SANSN, ML, and the largest zero-to-peak trace amplitudes measured on the cluster network horizontal seismograms, A_{max} , and are shown in Figure 8, with the tabulated values in Table II. The attenuation of the seismic waves as these progress from the epicentre to the station position is modelled with Equation [3] and where $C(R) + D$ have the same variables as in Equation [2]. Values for A_{max} , where the Richter magnitude difference in Figure 5 is >0.56 , were excluded from the analysis.

Local magnitude calibration of seismic events in the West Rand, Far West Rand

Table II

Newly derived tabulated calibration function – $\log_{10}A_0(\Delta)$ obtained from Equation [7] in Figure 8, which was derived by means of a multiple regression analysis. Change reflects the adjustment made to Richter's (1958) tabulated calibration function – $\log_{10}A_0(\Delta)$ listed in Table I

Δ (km)	$-\log_{10}A_0(\Delta)$	Change	Δ (km)	$-\log_{10}A_0(\Delta)$	Change
0	0.55	-0.85	35	2.09	-0.21
5	1.16	-0.24	40	2.18	-0.22
10	1.45	-0.05	45	2.26	-0.24
15	1.64	0.04	50	2.33	-0.27
20	1.78	0.08	55	2.41	-0.29
25	1.90	0.00	60	2.48	-0.32
30	2.00	-0.10			

The derived equation is:

$$0.547 R^2 = 0.473$$

$$-\log_{10}A_0(\Delta) = 0.831 \cdot \log_{10}(\Delta) + 0.00753^* \quad [7]$$

$$\Delta + 0.547 R^2 = 0.473$$

where distance $0 < \Delta < 60$ km and R^2 indicates a poor fit to the large scatter of the values for $-\log_{10}A_0(\Delta) = M_L - \log_{10}(A_{max})$ around the model. The poor fit is unsurprising, given the large scatter of the magnitudes around the best fit orthogonal (Equation [6]) in Figure 4 and the large scatter in Richter magnitude differences (within one standard deviation of 0.56) in Figure 5. However, the average values of $-\log_{10}A_0(\Delta)$ in 5 km bins (Figure 8) compare well with Equation [7] except for the 40 km bin, which may indicate a significant near-site amplification at that distance station compared to most of the seismic events. This shows that good estimates of Local magnitudes by the cluster networks are possible if outliers are rejected and a sufficient number of measurements with appropriate weights for signal-to-noise ratios are averaged, as is currently the practice with Antelope 5.4 software (2018). Most of Richter's (1958) tabulated calibration values are adjusted downward to account for the magnitude overestimate of approximately 0.1 of a unit established in Equation [6] when taking the incorrect model into consideration. This is as expected, since seismic waves show less attenuation with distance in South Africa than is the case in Southern California (Brandt, 2015). The largest adjustment is made at the epicentre, at 0 km distance, in line with the proposal by Hutton and Boore (1987) to derive calibration values for a surface focal depth of 0 km for shallow events as these will provide a better fit for crustal events. This is especially relevant in respect of mine seismic events, where the typical focal depth is 2 km (Brandt, 2014). The newly derived calibration values are similar to those in Equation [4] (Saunders et al., 2012) when adjusted for the constant difference between amplitudes recorded by horizontal seismographs and vertical seismographs.

Discussion and conclusions

Tabulated calibration values $-\log_{10}(A_0)$ were derived for the cluster network horizontal components, such that the Local magnitudes reported by the cluster networks on average have the same sizes as the Local magnitudes reported by the SANSN. This is an improvement on the current situation where the cluster networks, on average, overestimate seismic event magnitudes by approximately 0.1 of a magnitude unit.

The large scatter in magnitudes reported by individual stations for the same event is accounted for by the near-surface amplifications of the seismic waves at the recording sites. Antelope 5.4 software (2018) does not allow for the application of static corrections to the magnitudes of an individual station to compensate for its systematic over- or underestimation in comparison to the average magnitude of an event. The software was selected for its ability to automatically locate large numbers of mining events and to undertake a quick magnitude assessment. This is followed by manual re-analysis with a user-friendly graphical interface and is suitable for processing a large number of events. Even if it were possible to apply a static correction this would not be practical, because stations are re-located if the security at a site deteriorates. Hence, average magnitudes should be calculated from as many as possible individual stations to ensure the best possible magnitude estimates.

Magnitudes for larger events recorded by both the SANSN and cluster networks should be compared to one another. The seismometers of the SANSN are installed on bedrock inside high-quality vaults at sites with low background noise. The SANSN estimates of magnitudes for larger events should therefore be more accurate than those reported by the cluster networks.

Acknowledgements

This research was funded as part of the operation and data analysis of the South African National Seismograph Network and Cluster Mine Networks. The multiple regression analyses for this article were generated by means of the Real Statistics code (Zaiontz, 2020) in Microsoft® Excel® 2016. The maps were drafted using generic mapping tools (Wessel *et al.*, 2013) and graphs were prepared using Microsoft® Excel® 2016. I wish to thank the Council for Geoscience for permission to publish my results. Zahn Nel undertook the language editing. Two anonymous reviewers are thanked for their suggestions to improve the article.

References

- ANTELOPE. 2018. Boulder Real Time Technologies Incorporated. Antelope 5.4. <http://www.BRTT.com>
- BAKUN, W.H. and JOYNER, W. 1984. The ML scale in Central California. *Bulletin of the Seismological Society of America*, vol. 74, no. 5. pp. 1827–1843.
- BORMANN, P. (ed.), 2012. New Manual of Seismological Observatory Practice (NMSOP-2), IASPEI, GFZ German Research Centre for Geosciences, Potsdam. <http://nmsop.gfz-potsdam.de> doi: 10.2312/GFZ.NMSOP-2
- BRANDT, M.B.C. 2014. Focal depths of South African earthquakes and mine events. *Journal of the Southern African Institute of Mining and Metallurgy*. vol. 114. pp. 1–8.
- BRANDT, M.B.C. 2015. Qc and Qs wave attenuation of South African earthquakes. *Journal of Seismology*. doi 10.1007/s10950-015-9536-6
- HUTTON, L.K. and BOORE, D.M. 1987. The ML scale in Southern California. *Bulletin of the Seismological Society of America*, vol. 77. pp. 2074–2094
- RICHTER, C.F. 1935. An instrumental earthquake magnitude scale. *Bulletin of the Seismological Society of America*, vol. 25. pp. 1–32.
- RICHTER, C.F. 1958. *Elementary Seismology*. W. H. Freeman, San Francisco and London. 768 pp.
- SAUNDERS, I., BRANDT, M.B.C., STEYN, J., ROBLIN, D.L., and KIJRO, A. 2008. The South African National Seismograph Network. *Seismological Research Letters*, vol. 79. pp. 203–210. doi: 10.1785/gssrl.79.2.203
- SAUNDERS, I., OTTEMÖLLER, L., BRANDT, M.B.C., and FOURIE, C.J.S. 2012. Calibration of an ML scale for South Africa using tectonic earthquake data recorded by the South African National Seismograph Network: 2006 to 2009. *Journal of Seismology*. doi 10.1007/s10950-012-9329-0
- URHAMMER, R.A. and COLLINS, E.R. 1990. Synthesis of Wood-Anderson seismograms from broadband digital records. *Bulletin of the Seismological Society of America*, vol. 80. pp. 702–716.
- WESSEL, P., SMITH, W.H.F., SCHARROO, R., LUIS, J.F., and WOBBE, F. 2013. Generic Mapping Tools: Improved version released. *EOS Transactions of the American Geophysical Union*, vol. 94. pp. 409–410.
- ZAIONTZ, C. 2020. Real statistics using Excel. <http://www.real-statistics.com> ◆



Drill and Blast Short Course 2022

23-24 FEBRUARY 2022

ONLINE VIA ZOOM

VENUE: WITS CLUB, JOHANNESBURG

CPD Points

0.1 CPD points for every 1 hour event attended
online or contact

BACKGROUND

There has been a significant change in the explosives and initiating systems used in the mining, quarrying and civil blasting applications both on surface and underground. This short course will provide and align the delegates with some basic principles, tools, examples and understanding of the leverage of these products. Whether you are new to the industry or a seasoned user or find yourself in the position of an explosive manager or supervisor to a regulator, the course will enable some debate, rules and questions you should be asking of your explosive OEM.

The importance of improved safety standards, cost effectiveness and productivity has driven mining management and operators to examine all facets of their operations. Increasingly it has been realised that an efficient drilling and blasting program can impact positively throughout the mining operation from loading to maintenance, hauling to crushing, ground support to scaling and grade control to recovery. We will also test the concepts and increasing challenges of blasting in the vicinity of local communities.

PROGRAMME

'What is an explosive?'

- We will look at the evolution and properties of explosives from Black powder to Ammonium Nitrate, adding fuel oil to make ANFO, packaged explosives and the modern bulk or pumpable technology.

Requirements of an Initiating System

- Where have we come from, safety fuse and how do pyrotechnic detonators (Shock tube) fit to Electronic detonators and their impact on blast design.

Drilling and Blast Design principles

- Reviewing the principles that a well drilled hole is key to a successful blast and what is the relationship to blast geometry.

Blast design principles

- Some simple tools to use, review and calculate your blast design.

Initiation and Timing of Blasts

- Understanding the principles of timing and how this enables us to shape and move the blast muckpile. The addition of control to both manage the uniformity and fragmentation as well as environmental control using electronics.

Specialised Blasting Techniques

- A look into the world of specialised blasting, highwall stability, secondary breaking & demolition.

Environmental and Health

- Managing the community and avoiding the issues of ground vibration, noise & airblast.

PRESENTER



Simon Tose is an expert in Blast Design from AECI and will be sharing his expertise on this subject.

Simon Tose is an established industry recognised consultant, registered professional engineer and leader in technology, mining, explosives and blasting science. Holding a BSC Hons Mining Engineering degree, management and explosive qualifications. Extensive experience in mining methods, education and management of projects and blast investigations. He has written papers, articles and presented at a number of International and Local conferences. Current board member of the IOQSA & ISEE and regular contributions to the SAIMM & AusIMM.

With a strength in project design he leads the Blast Consult team with a strong passion for the development of environmental and blast monitoring, measurement and investigation, consulting, management and financial analysis for AECI

FOR FURTHER INFORMATION, CONTACT:

Camielah Jardine, Head of Conferencing

E-mail: camielah@saimm.co.za | Tel: +27 11 834-1273/7 | Web: www.saimm.co.za



SAIMM
THE SOUTHERN AFRICAN INSTITUTE
OF MINING AND METALLURGY



Comparison of normalized and non-normalized block caving comminution models

by R. Gómez¹, R. Castro^{2,3}, F. Betancourt¹, and M. Moncada¹

Affiliation:

¹Department of Metallurgical Engineering, University of Concepción, Concepción, Chile.

²Advanced Mining Technology Center, University of Chile, Santiago, Chile.

³Department of Mining Engineering, University of Chile, Santiago, Chile.

Correspondence to:

R. Gómez

Email:

regomez@udec.cl

Dates:

Received: 3 Mar. 2021

Revised: 4 Aug. 2021

Accepted: 10 Aug. 2021

Published: November 2021

How to cite:

Gómez, R., Castro, R., Betancourt, F., and Moncada, M. 2021 Comparison of normalized and non-normalized block caving comminution models. *Journal of the Southern African Institute of Mining and Metallurgy*, vol. 121, no. 11, pp. 581–588

DOI ID:

<http://dx.doi.org/10.17159/2411-9717/1150/2021>

ORCID:

R. Gómez
<https://orcid.org/0000-0003-4273-0522>

Synopsis

In block cave mining, rock fragmentation is a key parameter that influences the production level design and mine planning. Fragmentation occurs mainly by natural breakage during the caving process and in the draw column. The breakage that occurs within the column is known as secondary fragmentation. Secondary fragmentation has been successfully described using the block caving comminution model, which replicates the fragmentation mechanics between particles under drawn and vertical loads in a draw column. This model is based on a kinetic and population balance approach, in which non-normalized and normalized assumptions can be used depending on material and comminution system behaviour. In this paper, the non-normalized and normalized approaches are applied and compared to laboratory data to determine which assumption should be used for secondary breakage in block caving. Approaches are compared graphically, with the mean square error and the Fisher test with a false-rejection probability of 0.05. Based on a statistical analysis, the results show that the normalized model can be applied to all the rock types tested.

Keywords

block caving, breakage, comminution, mass balance, secondary fragmentation, modelling.

Introduction

The block caving method has been widely used in the mining industry for over 30 years. In this process, three stages can be identified: *in-situ* fragmentation, and primary and secondary fragmentation. The rock size obtained after secondary fragmentation has a strong influence on design stages, ore extraction and haulage, and mineral processing (Laubscher, 1994, 2000; Eadie, 2003; Brown, 2004). Particularly, in cave mining, the process is also influenced by the geometry of draw zones, which defines the drawpoint spacing, draw control, rate of draw, and secondary breakage (Laubscher 1994; Kurniawan and Setyoko, 2008). During ore draw, the rock fragment size can cause operational problems such as hangups, oversized material, fine material migration, inrush of fines, and mudrush events. These are some of the main reasons to study and estimate the rock fragmentation in block caving mines.

During block caving, fragmentation of the ore column occurs mainly by natural breakage induced by mining or by blasting applied in the base of the ore column from the undercut level or production level (Paredes *et al.*, 2020). Additionally, preconditioning can be used to create new fractures or expand existing ones by hydraulic fracturing, confined blasting, or both. However, the fragmentation of the ore occurs mainly during caving and ore draw.

Fragmentation takes place in three stages. *in-situ* fragmentation is the natural fragmentation in the rock mass prior to mining activity, and which can be modified using preconditioning (Brzovic *et al.*, 2016). Primary fragmentation occurs during caving, where the rock around the cave back is fragmented and then falls. Secondary fragmentation occurs in the broken column during draw and is the last stage of fragmentation before extraction at the drawpoint. In this stage the rock fragmentation is due mainly to compression and abrasion (splitting and attrition). Some authors also include impact fragmentation, which is highly influenced by the air gap height, as a mechanism of secondary fragmentation (Laubscher, 2000; Brown 2004; Pierce, Weatherley, and Kojovic, 2010; Dorador, 2016).

The breakage of the granular material under stress depends on various factors such as particle size distribution (PSD), particle shape, the state and trajectory of effective stresses, void ratio, material strength, presence of water, and extraction rate (Hardin, 1985; Brown, 2004; Liu *et al.*, 2018). Among these factors, strength is one of the most relevant. Low rock strength implies early breakage of the

Comparison of normalized and non-normalized block caving comminution models

rock block under a stress arch (Laubscher, 2000). Conversely, increasing strength decreases the amount of fragment breakage under a given stress (Lade, Yamamuro, and Bopp, 1996). Similarly, for an individual block, it is well known that strength decreases as size increases (Brady and Brown, 2004; Cundal, Pierce, and Mas Ivars, 2008). Particularly in block caving, where large volumes of rock are common, rock strength is a consequence of the intact rock strength, the presence of discontinuities, and the deformation capacity (Brady and Brown, 2004). Dorador (2016) observed that rock strength has more influence on fragmentation than parameters such as shape and size distribution. On the other hand, it has been reported that the strength ratio between large and small blocks plays an important role in crushing (McDowell and Bolton, 1998; Wood and Maeda, 2008). Furthermore, strength has been shown to decrease in the presence of moisture, as seen during crushing tests on individual particles (Manso, Marcelino, and Caldeira, 2021). An explanation for this phenomenon is that the infiltration of water into microcracks increases the pressure on the rock, facilitating its rupture (Miura and Yamanouchi, 1975; Lee and Farhoomand, 1967; Lee and Coop 1995).

In terms of material shape, angular particles suffer greater breakage than rounded or cubic ones of equal size and under similar levels of stress (Lee and Farhoomand, 1967; Dorador, 2016). This behaviour is explained by the load concentration in small areas of the particles, increasing the stress and facilitating fracture (Lade, Yamamuro, and Bopp, 1996). Another possible explanation is that angular particles fracture preferentially by abrasion (breaking of the edges), while rounded ones fracture by compression, presenting a greater apparent resistance (Nakata *et al.*, 1999).

Breakage is also affected by fine material transported through the extraction column via the voids between the larger blocks, with fines more concentrated towards the base of the mineral column (Hashim, Sharrock, and Saydam, 2008; Dorador *et al.*, 2014). This fine material imparts a cushioning effect to the coarse material, thus reducing the degree of breakage (Brown, 2004). Such a phenomenon occurs because the presence of fine material prevents direct contact between coarse blocks, increasing the number of contacts and reducing their probability of breakage by avoiding a high concentration of stresses in a small area of the block (McDowell, 2002).

The extraction rate determines the residence time of a block in the column of broken material. Increasing the extraction rate decreases the magnitude of the shear stresses, thus reducing fragmentation (Sainsbury, 2010). At low extraction rates, fracturing of the material depends on the effective time during which it is under stresses associated with caving and/or under arc conditions (Laubscher, 2000). Another relevant aspect in fragmentation is material transport through the ore pass. The impact of the distance travelled during transfer through the ore pass has been quantified – Landriault (2001) cites a 78% decrease in the average size (d_{50}) after travelling 257 m. A similar result was obtained in Brunswick and Kidd Creek mines, where the maximum particle size was reduced by 50% after travelling 300 m of vertical distance (Yu, 1989).

Various models can be used to estimate the fragmentation in block caving, in particular the secondary fragmentation reported as the final fragmentation at the drawpoint (*e.g.* Merino, 1986; Nicholas and Srikant, 2004; Esterhuizen, 2005; Pierce, 2009; Rogers *et al.*, 2010; Dorador, 2016; Gómez *et al.*, 2017). The

Block Cave Fragmentation (BCF) Model (Esterhuizen, 2005) is probably the most widely used in industry. This approach estimates primary and secondary fragmentation based on empirical rules. The REBOP (Rapid Emulation based on PFC) secondary fragmentation model is based on Bridgewater's attrition model (Bridgewater *et al.*, 2003). Srinkant and Rachmandl (2004) combined CoreFrag2 (to estimate primary fragmentation) and BCF (for secondary fragmentation), obtaining good results in medium and coarse sizes (d_{50} and d_{80}). Dorador (2016) divided the broken column into a far field, characterized by plug flow, and a near field, characterized by mixed flow, to estimate secondary fragmentation. In the Block Caving Comminution Model (Gómez *et al.*, 2017), the rock flow is simulated considering compression and abrasion, the main fragmentation mechanisms during secondary fragmentation, and is validated through experiments. In this work we extend the model by Gómez *et al.* (2017) by studying a hypothesis about the model and performing experiments with different types of rock. An example in which the extended model is applied to real data is given in the Appendix.

Block Caving Comminution Model

Block caving is widely used in massive underground mining because of the high production rates and low operational costs. With this method, rock fragmentation occurs naturally during ore extraction while caving propagates to the surface. Thus, fragmentation is determined mainly by rock mass properties, stress fields, and draw policies. Here we focus our analysis on a model used to estimate the secondary fragmentation presented as the Block Caving Comminution Model (BCCM) (Gómez *et al.*, 2017).

The BCCM in its batch version is determined by the following mass conservation equation:

$$\frac{df_i(t)}{dt} = -S_i f_i(t) + \sum_{j=1}^{i-1} b_{ij} S_j \quad [1]$$

where f_i is the solid mass fraction of size interval i , S_i is breakage velocity of the i^{th} interval, and b_{ij} is the breakage function and represents the fraction of the primary breakage product of material in the j^{th} interval, which appears in the i^{th} interval after fragmentation. Extraction in block caving is a continuous process that is usually modelled by plug flow. Then, incorporating this plug flow assumption in Equation [1] and using the Reid solution for the batch population balance (Reid, 1965), we obtain

$$m_i = \sum_{j=1}^i A_{ij} e^{-S_j \tau} \quad [2]$$

where m_i is the mass in the i^{th} interval, τ is the residence time and A_{ij} is given by

$$A_{ij} = \begin{cases} 0 & \text{if } i < j \\ f_{i0} - \sum_{k=1}^{i-1} A_{ik} & \text{if } i = j \\ \sum_{k=j}^{i-1} \frac{b_{ik} S_k}{S_i - S_j} A_{kj} & \text{if } i > j \end{cases} \quad [3]$$

where f_{i0} is the initial particle size distribution.

In order to compute Equation [2] it is necessary to know the values of the functions B_{ij} and S_j . The common way to determine these functions is by assuming a constitutive parametric form

Comparison of normalized and non-normalized block caving comminution models

and performing a back-calculation from experimental data (Klimpel and Austin, 1977). In this work we consider for S_j the parametric expression proposed by Herbst and Fuerstenau (1980) and later modified by Gómez *et al.* (2017):

$$S_j = S_1 \exp \left\{ Z_1 \ln \left(\frac{d_i}{d_1} \right) + Z_2 \left[\ln \left(\frac{d_i}{d_1} \right) \right]^2 \right\} \sigma_v \quad [4]$$

Here Z_1 and Z_2 are parameters depending on the material properties, and σ_v is a variable that represents the mean vertical load. It is common to use the cumulative fraction of breakage product $B_{ij} = \sum_{k=i}^n b_{kj}$ (instead of b_{ij}) as $b_{ij} = B_{ij} - B_{i+1,j}$, the so-called *normalized* expression for B_{ij} is given by

$$B_{i1} = \alpha_1 \left(\frac{x_i}{x_2} \right)^{\alpha_2} + (1 - \alpha_1) \left(\frac{x_i}{x_2} \right)^{\alpha_3} \quad [5]$$

where α_1 , α_2 , and α_3 are model parameters ($0 < \alpha_1 < 1$; $\alpha_2 < \alpha_3$), is the mesh size for the i^{th} interval, and x_2 , which corresponds to the second mesh size interval, is the normalizing parameter. We remark that in the normalized expression Equation [5], it is assumed that all particles have a rupture distribution with dimensional similarity.

The *non-normalized* model raises this hypothesis, which is given by the expression (Austin and Luckie, 1972):

$$B_{ij} = \alpha_j \left(\frac{x_i}{x_j} \right)^{\alpha_2} + (1 - \alpha_j) \left(\frac{x_i}{x_j} \right)^{\alpha_3} \quad [6]$$

where

$$\alpha_j = \alpha_1 \left(\frac{x_j}{x_1} \right)^{-\delta} \quad [7]$$

and δ is a new parameter to be adjusted ($\delta > 0$) for $0 < \alpha_j < 1$. For $I > j$, it must be noted that the normalized expression presented in Equation [5] is a simplified case of Equation [6] when $\delta = 0$ and $x_j = x_2$. According to the constitutive expressions selected in this work, the back-calculation method yields a nonlinear optimization problem with six parameters ($S_1^E, Z_1, Z_2, \alpha_1, \alpha_2, \alpha_3$) in the normalized framework and seven parameters ($S_1^E, Z_1, Z_2, \alpha_1, \alpha_2, \alpha_3, \delta$) in the non-normalized framework.

In milling processes, normalized models are typically suitable (Austin and Concha, 1994), but in the block caving process the normalization of the model has not been studied. The aim of this paper to compare the normalized and non-normalized models using statistical analysis of a variety of rock types to identify which approach should be used with block caving methods.

Methodology

Laboratory set-up

The confined flow model set-up consisted of a steel cylinder able to retain rock fragments while vertical pressure was applied through a hydraulic press machine. The model geometry consisted of an inside diameter of 0.34 m, height of 0.70 m, and steel width contour of 0.03 m. Fragmented material was drawn from a drawbell at the bottom, emulating a block caving mine extraction system using a scaled LHD to draw the material. A constant vertical pressure was applied in each test.

Material was drawn from the bottom until the flow reached the top of the fragmented material (around 10% of the total fragmented material in over two hours). Then all material was homogenized, and the fragment size distribution was measured by sieving.

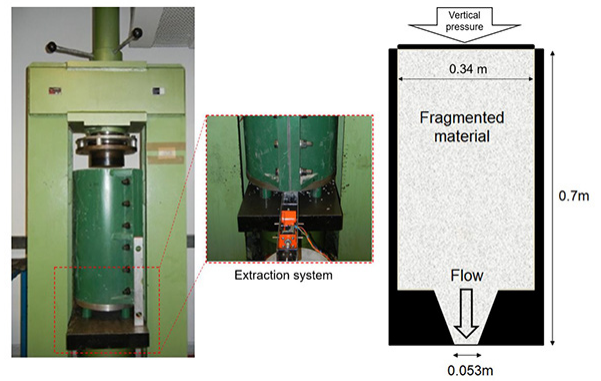


Figure 1—Confined flow system used in fragmentation tests (left, Gómez *et al.*, 2017) and a side view inside the model (right)

Table I

Rock characteristics summary

Rock type	Density (t/m ³)	$I_{s,50}$ (MPa)	Sphericity	Roundness	Friction angle (°)
A	2.62	5.93	0.58	0.25	39
B	2.60	1.25	0.68	0.22	40
C	2.71	1.64	0.68	0.20	37
D	2.69	6.93	0.65	0.51	48

A: Primary sulphide ore composed of biotite and amphibole granitoid from Antofagasta, Chile.

B: Primary sulphide ore composed mainly of sericite from Calama, Chile.

C: Primary sulphide ore composed of quartz and ore from Calama, Chile.

D: Gravel, quarry from Santiago, Chile.

Mineral materials

Four rock types were tested in the same confined flow system. Table I shows the rock density, $I_{s,50}$ (point load index) and internal friction angle obtained through standard laboratory tests. Sphericity and roundness were determined using the methodology proposed by Cho, Dodds, and Santamarina (2006).

Tests and data fitting

The four materials with different initial size distribution curves were used with constant vertical pressures applied during the comminution tests:

- Rock type A (MPa): 0.8, 1.5, 3, 5
- Rock type B (MPa): 2
- Rock type C (MPa): 1, 2
- Rock type D (MPa): 1, 1.5, 3, 6.

The normalized and non-normalized model parameters were adjusted using the fragment size distribution curves from the comminution tests. The trust-region-reflective least squares algorithm was used to obtain the model parameters (Moré and Sorensen, 1983), minimizing the square of the difference between experimental and modelled data.

$$\min \sum_{j=1}^m \sum_{i=1}^n (f_{ij,exp} - f_{ij,mod})^2 \quad [8]$$

where $f_{ij,exp}$ and $f_{ij,mod}$ are the experimental and modelled mass fraction of size interval i at pressure j respectively. We note that the non-normalized case includes the δ parameter with the constraints ($\delta > 0$) for $0 < \alpha_j < 1$.

Comparison of normalized and non-normalized block caving comminution models

In order to evaluate whether the addition of the parameter δ is relevant, an F-test was performed. The null hypothesis is the normalized model with $\delta = 0$ nearly equal to the non-normalized model with $\delta > 0$. The F-value was calculated using Equation [9]:

$$F = \frac{\frac{MSE_{\delta=0} - MSE_{\delta>0}}{k}}{\frac{MSE_{\delta>0}}{N-M}} \quad [9]$$

where MSE is the mean square error, k is the number of conditions (here $\delta = 0$), N is the number of data points, and M is the number of parameters of the model i .

Results

In this section we present the results of the parameter identification for the normalized and non-normalized approaches, the selection and breakage functions, and the Fisher test. The complete experimental data can be found in the Appendix.

Fitted parameters

The non-normalized model parameters obtained for each rock type are summarized in Table II. In all cases the residence time τ is kept constant and equals the average residence time of the tests (approx. 0.1 day).

In general, the non-normalized and normalized model parameters do not present significant differences: for example, rock types A and C present the same α_1 . These similarities between the models are also observed in the selection and breakage functions as shown in Figures 2 and 3.

Selection and breakage functions

Figure 2 shows the rate of breakage (S^F), and Figure 3 shows the breakage functions (B_{ij}) of rock types A, B, C, and D.

The influence of fragment sizes on the rate of breakage when $\delta = 0$ is not significant. Thus, α_i (Equation [7]) could be assumed constant, depending on fragment size. This is also noticed in the breakage function in Figure 3 for $\delta > 0$, where for each rock type data-point, the breakage functions follow the same resulting fragment size distribution, independent of initial fragment size (as modelled by the normalized BCCM presented in Gómez *et al.* 2017).

Fisher test

Using a false-rejection probability of 0.05, the critical values of the F-distribution are presented in Table III. Here, all the F-values are lower than the respective critical values; therefore, the use of the simplified normalized model is recommended in these cases.

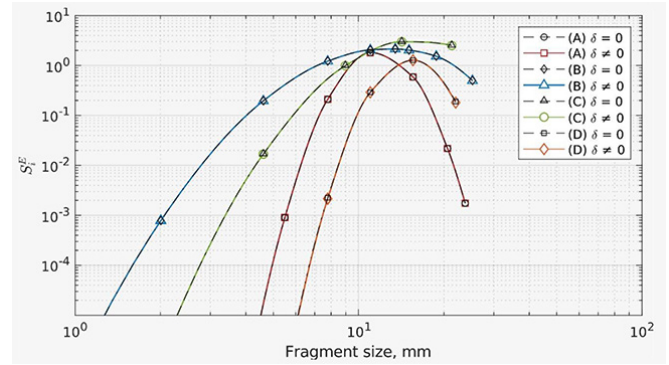


Figure 2—Selection functions

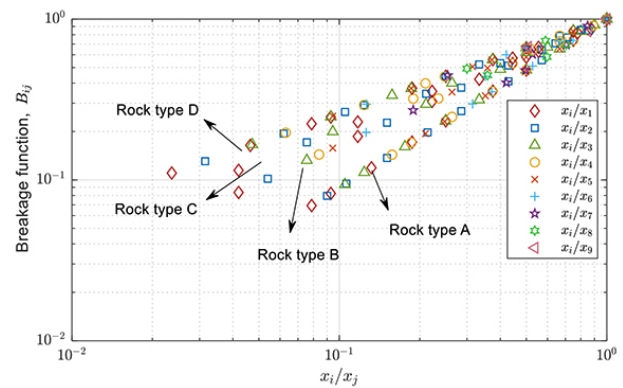


Figure 3—Breakage functions

Table III

Mean square error and F-test results

Rock type	MSE $\delta = 0$ (% ²)	MSE $\delta > 0$ (% ²)	F critical	F
A	10.62	10.35	3.97	2.01
B	2.49	2.46	18.51	0.03
C	1.03	0.96	6.61	0.27
D	3.44	3.43	3.98	0.22

Conclusions

The literature indicates that in milling systems the normalized model (Equation [5]) can be applied in almost all cases. However, this assumption cannot be considered a *priori* in the block caving method since the mechanism of breakage differs from

Table II

Normalized and non-normalized model parameters

Model	Rock type	τ	S_1^E	Z_1	Z_2	α_1	α_2	α_3	δ
Normalized	A	0.1	0.002	-19.521	-13.637	0.810	0.968	1.780	0.000
	B	0.1	0.744	-3.139	-2.310	0.098	0.569	0.779	0.000
	C	0.1	2.518	-1.762	-3.290	0.048	0.739	0.828	0.000
	D	0.1	0.190	-10.373	-14.080	0.859	0.588	0.598	0.000
Non-normalized	A	0.1	0.002	-19.517	-13.635	0.810	1.050	1.060	0.079
	B	0.1	0.744	-3.139	-2.310	0.467	0.779	0.789	0.096
	C	0.1	2.518	-1.763	-3.290	0.048	0.680	0.690	0.830
	D	0.1	0.182	-10.567	-14.265	0.683	0.588	0.598	0.102

Comparison of normalized and non-normalized block caving comminution models

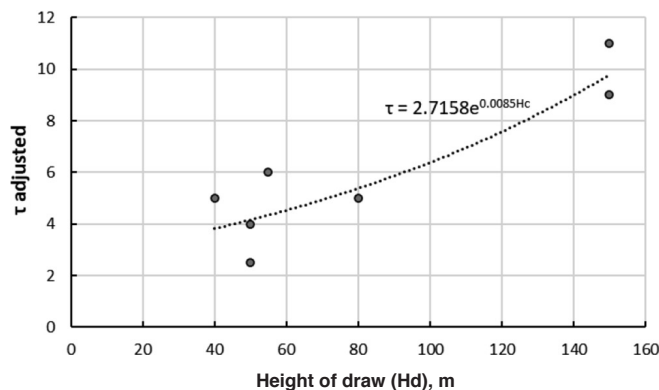


Figure 4—Residence time based on study cases

that in the milling process. The non-normalized model implies that in the breakage function, B_j , the resulting fragment size distribution depends on the original fragment size. According to the experimental results and parameter fitting, we found that the fragment size distribution is independent of the initial fragment sizes. Thus, for the materials and confined flow system examined here, a simplified normalized model should be used, independent of the material.

It must be noted that abrasion and compression are the fragmentation mechanisms observed in the experiments, but compression is probably the dominant mechanism. Compression generates a narrow particle size distribution with relatively low quantities of fine and large particles, which we speculate explains the results of this work. It is well known that the stress over the rock depends on the height at which it is located. In the present model, this stress is supposed to be constant throughout the column, which can lead to differences with respect to experimental data. In a later work, we will extend the present model by incorporating this dependence into the governing equations.

Acknowledgments

This work was funded by the CONICYT PFCHA/DOCTORADO BECAS CHILE/2018 – 21180046. The Block Caving Laboratory and the Advanced Mining Technology Center of the University of Chile, CONICYT project FB0809. F.B. acknowledges the support of ANID/PIA/AFB170001 and ANID/FONDAP/15130015.

Conflict of Interest

The authors declare that they have no conflict of interest.

Appendix A: BCCM applications

First, it is necessary to determine the parameters of the model

($S_i^F, Z_1, Z_2, a_1, a_2, a_3$) to apply the BCCM, by making an adjustment from experimental laboratory tests. Subsequently, it is possible to solve the governing equations of the model if we know the input curve (primary fragmentation), physical characteristics of the column, and the operational conditions.

The model was evaluated for five reported mine cases. The first fragmentation reported is considered as the primary fragmentation. The laboratory calibration parameters of rock type A (Table IV), which has a strength similar to the selected mine cases, were used. The mean vertical stress in the broken column was estimated through the Janssen equation (Nedderman, 1992).

The fragmentation rate is scaled with respect to laboratory experiments so that

$$\tau_i S_i(\text{lab}) = \tau_i S_i(\text{mine}) = \text{constant} \quad [10]$$

The residence time for all cases was estimated using

$$\tau = \frac{HA\rho}{D_r} \quad [11]$$

The results obtained using the residence time calculated by the previous equation show that the model overestimates the rock fracture. This behaviour had already been reported in Gómez *et al.* (2017). These differences can be ascribed to three reasons: (i) the material suffers the greatest fractures at the beginning of the process; (ii) the vertical forces are usually low close to the movement zones, and (iii) the draw rate and vertical force are dependent on the height of the column, which changes over time. Figure 4 shows the results considering a residence time between 1.5 and 3.7% of that calculated by Equation [11]. In this case, the data provided by the model fit well to the real data of the cases studied.

Figure 5 shows the fragmentation results using the model considering the real residence time (Equation [11], blue points in Figure 5) and the adjusted residence time (red squares in Figure

Table IV

Mine cases

Mine-sector	Intact rock strength (MPa)	Vertical load, (MPa)	Draw height primary frag
DOZ-diorite (Kurniawan and Setyoko, 2008)	111	3.2	Unknown
Esmeralda-B2 (Gómez <i>et al.</i> , 2017)	100–130	2.2	0–20 m
Reno-HW (Gómez <i>et al.</i> , 2017)	115	2.5	0–50 m
Teniente 4 Sur (Hurtado, Pereira and Campos, 2007)	125	4.4	0–50 m
Ridgeway (volcanic) (Brunton, Lett, and Thronhill, 2016)	130	3.5	0–25 m

Comparison of normalized and non-normalized block caving comminution models

5). Importantly, we need to use a shorter residence time to obtain a good fitting. Also, the effect of the greater extraction height of the same mine can be observed in Figures 5C and D, and Figures 5E and F.

Appendix B: Experimental data

Experimental data used to calibrate both models is presented here.

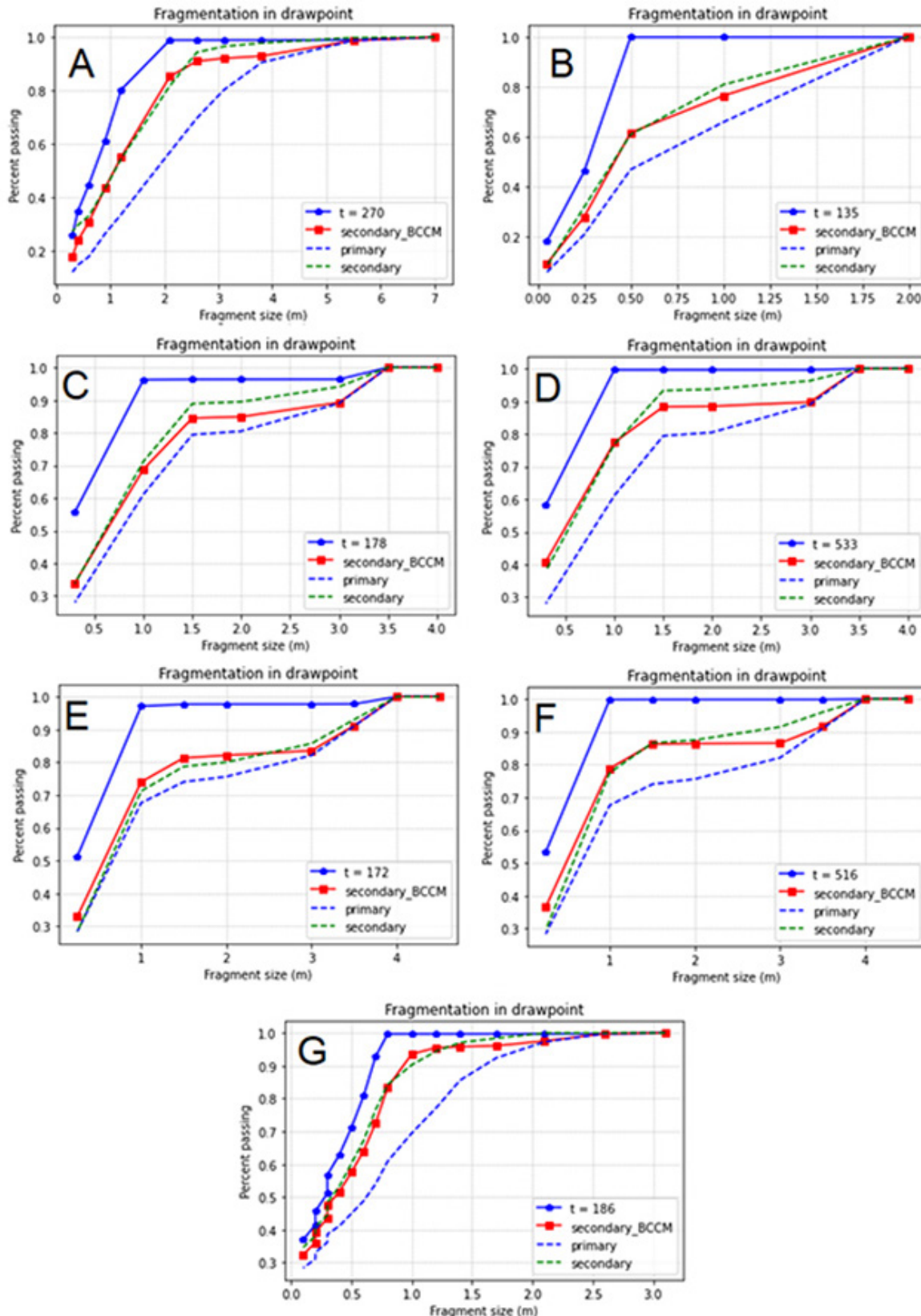


Figure 5—Estimation using BCCM at mine scale. A: DOZ-diorite. B: Esmeralda-b2, secondary (0–60 m). C: Reno-hw, secondary (0–100 m). D: Reno-hw, secondary (0–200 m). E: Teniente 4 sur, secondary (0–100 m). F: Teniente 4 sur, secondary (0–200 m). G: Ridgeway volcanic, secondary (0–75 m)

Comparison of normalized and non-normalized block caving comminution models

Table V

Fragmentation results obtained from confined flow test, rock type A

Rock type A Size (mm)	% passing				
	Initial	Test 0.8 MPa	Test 1.5 MPa	Test 3 MPa	Test 5 MPa
28.58	100.0%	100.0%	100.0%	100.0%	100.0%
25.40	97.5%	97.5%	98.0%	97.8%	98.4%
22.23	95.7%	95.8%	96.6%	96.2%	96.1%
19.05	92.4%	93.3%	93.6%	93.7%	93.7%
12.70	68.8%	75.5%	78.5%	80.2%	82.7%
9.53	39.1%	55.4%	60.7%	61.8%	62.4%
6.35	12.2%	21.3%	24.5%	26.9%	30.3%
4.75	5.0%	8.4%	10.1%	14.9%	16.2%
3.35	2.2%	3.5%	5.2%	6.4%	8.1%
2.36	1.2%	1.7%	2.8%	3.0%	4.1%
2.00	1.1%	1.1%	2.0%	1.6%	1.9%
25.40	100.0%	100.0%	100.0%	100.0%	100.0%
22.23	98.2%	98.1%	98.3%	98.2%	99.1%
19.05	96.6%	96.6%	96.7%	96.6%	97.4%
12.70	86.6%	86.7%	87.8%	90.1%	93.9%
9.53	62.8%	69.2%	74.5%	75.1%	81.0%
6.35	25.2%	35.8%	37.1%	42.6%	43.4%
4.75	10.0%	15.2%	15.2%	21.2%	22.6%
3.35	3.8%	6.5%	6.8%	10.5%	10.7%
2.36	1.7%	3.4%	3.4%	6.7%	6.7%
2.00	1.6%	2.7%	2.1%	4.4%	4.4%

Table VI

Fragmentation results obtained from confined flow test, rock type B

Rock type B Size (mm)	% passing	
	Initial	Test 2 MPa
28.58	100.0%	100.0%
22.23	97.7%	98.3%
15.88	91.0%	93.4%
14.29	86.1%	90.5%
12.70	78.0%	85.7%
9.53	51.1%	66.6%
6.35	22.0%	41.6%
3.35	5.0%	19.9%
1.20	0.0%	6.3%

Table VII

Fragmentation results obtained from confined flow test, rock type C

Rock type C Size (mm)	% passing		
	Initial	Test 1 MPa	Test 2 MPa
28.58	100.0%	100.0%	100%
15.88	91.0%	92.7%	94.0%
12.70	78.0%	81.6%	86.3%
6.35	22.0%	29.1%	37.3%
3.35	5.0%	9.4%	15.2%
1.20	0.0%	2.7%	4.0%

References

AUSTIN, L. and CONCHA, F. 1994. Discrete mill kinematic: Population mass balance of sizes. *Design and Simulation of Mill and Classification Circuits*. Austin L. and Concha F. (eds). CYTED, Concepcion, Chile. pp. 65–82 [in Spanish].

AUSTIN, L. and LUCKIE, P.T. 1972a. Estimation of non-normalized breakage distribution parameters from batch grinding. *Powder Technology*, vol. 5, no. 5. pp. 267–271.

Table VIII

Fragmentation results obtained from confined flow test, rock type D

Rock type D Size (mm)	% passing				
	Initial	Test 1 MPa	Test 1.5 MPa	Test 3 MPa	Test 6 MPa
25.40	100.0%	100.0%	100.0%	100.0%	100.0%
19.05	98.1%	98.1%	98.1%	98.8%	98.5%
12.70	77.6%	78.2%	76.3%	88.0%	89.7%
9.53	58.3%	65.5%	64.4%	68.7%	72.8%
6.35	39.0%	45.4%	45.7%	47.1%	49.6%
4.75	24.4%	30.1%	31.4%	34.9%	37.2%
2.36	9.9%	12.4%	14.2%	17.8%	17.5%
2.00	5.0%	7.1%	8.5%	11.0%	11.8%
1.18	2.0%	3.6%	4.5%	6.3%	7.3%
0.60	1.0%	1.5%	1.9%	2.5%	3.0%
25.40	100.0%	100.0%	100.0%	100.0%	100.0%
19.05	98.1%	98.5%	98.1%	97.7%	98.5%
12.70	77.6%	82.9%	84.5%	82.4%	87.7%
9.53	58.3%	63.0%	63.3%	59.6%	69.8%
6.35	39.0%	39.1%	40.3%	38.4%	48.9%
4.75	24.4%	24.5%	26.1%	25.8%	34.2%
2.36	9.9%	9.8%	10.7%	10.4%	17.3%
2.00	5.0%	5.1%	5.9%	6.8%	11.0%
1.18	2.0%	2.2%	2.8%	3.5%	6.5%
0.60	1.0%	1.0%	1.2%	1.5%	2.7%

BRADY, B.H.G. and BROWN, E.T. 2004. *Rock Mechanics for Underground Mining*. Springer.

BROWN, E.T. 2004. Fragmentation assessment. *Block Caving Geomechanics*. 2nd edn. Brown, E.T. (ed.). JKMR, Queensland. pp. 184–227

BRUNTON, I., LETT, J., and THORNHILL, T. 2016. Fragmentation prediction and assessment at the Ridgeway Deeps and Cadia East cave operations. *Proceedings of the 7th International Conference & Exhibition on Mass Mining: Massmin 2016*. Australasian Institute of Mining and Metallurgy, Melbourne. pp. 151–160.

BRZOVIC, A., VALLEJOS, A., ARANCIBIA, E., BURGOS, L., DELONCA, A., GAETE, M., and BARRERA, V. 2016. Analysis and modelling of the fragmentation process – Case studies at El Teniente mine. *Proceedings of the 7th International Conference & Exhibition on Mass Mining*. Australasian Institute of Mining and Metallurgy, Melbourne. pp. 305–310.

CUNDALL, P.A., PIERCE, M.E., and MAS IVARS, D. 2008. Quantifying the size effect of rock mass strength. *Proceedings of the First Southern Hemisphere International Rock Mechanics Symposium*. Australian Centre for Geomechanics, Perth. pp. 3–15.

CHO, G., DODDS, D., and SANTAMARINA, J.C. 2006. Particle shape effects on packing density, stiffness and strength: natural and crushed sands. *Journal of Geotechnical and Geoenvironmental Engineering*, vol. 132, no. 5. pp. 591–602.

DORADOR L. 2016. Experimental investigation of the effect of broken ore properties on secondary fragmentation during block caving. PhD thesis, University of British Columbia.

DORADOR, L., EBERHARDT, E., ELMO, D., and AGUAYO, A. 2014. Influence of secondary fragmentation and column height on block size distribution and fines migration reaching drawpoints. *Proceedings of the 3rd International Symposium on Block and Sublevel Caving*, Santiago, Chile. Castro, R. (ed.). Universidad de Chile. pp. 5–6.

EADIE, B.A. 2003. A framework for modelling fragmentation in block caving. PhD thesis, University of Queensland.

GÓMEZ, R., CASTRO, R., CASALI, A., PALMA, S., and HEKMAT, A. 2017. A comminution model for secondary fragmentation assessment for block caving. *Rock Mechanics and Rock Engineering*, vol. 50. pp. 3073–3084.

HARDIN, B.O. 1985. Crushing of soil particles. *Journal of Geotechnical Engineering*, vol. 111, no. 10. pp. 1177–1192.

Comparison of normalized and non-normalized block caving comminution models

- HASHIM, M.H.M., SHARROCK, G.B., and SAYDAM, S. 2008. A review of particle percolation in mining. *Proceedings of the First Southern Hemisphere International Rock Mechanics Symposium*. Australian Centre for Geomechanics, Perth. pp. 273–284.
- HERBST, J.A. AND FUERSTENAU, D.W. 1980. Scale-up procedure for continuous grinding mill design using population balance models. *International Journal of Mineral Processing*, vol. 7, no. 1. pp. 1–31.
- HURTADO, J.P., PEREIRA, J., and CAMPOS, R. 2007. Pre-feasibility study project NNM - NNM-ICO-GEO-INF N° 003. Teniente, Internal Report.
- KLIMPEL, R.R. and AUSTIN, L.G. 1977. The back-calculation of specific rates of breakage and non-normalized breakage distribution parameters from batch grinding data. *International Journal of Mineral Processing*, vol. 4, no. 1. pp. 7–32.
- KURNIAWAN, C. and SETYOKO, T.B. 2008. Impact of rock type variability on production rates and scheduling at the DOZ-ESZ block cave mine. *Massmin 2008. Proceedings of the 5th International Conference and Exhibition on Mass Mining*, Luleå, Sweden, 9–11 June 2008. Luleå University of Technology.
- LADE, P.V., YAMAMURO, J.A., and BOPP, P.A. 1996. Significance of particle crushing in granular materials. *Journal of Geotechnical Engineering*, vol. 122, no. 4. pp. 309–316.
- LANDRIAULT, D. 2001. Backfill in underground mining. *Underground Mining Methods, Engineering Fundamentals and International Case Studies*. Hustrulid, W.A. and Bullock, R.L. (eds). SME. pp. 601–614.
- LAUBSCHER, D.H. 1994. Cave mining – The state of the art. *Journal of the South African Institute of Mining and Metallurgy*, vol. 94, no. 10. pp. 279–293.
- LAUBSCHER, D.H. 2000. Secondary fragmentation. *A Practical Manual on Block Caving*. <https://www.resolutionmineeis.us/sites/default/files/references/laubscher-2000.pdf>
- LEE, K.L. and FARHOOMAND, I. 1967. Compressibility and crushing of granular soil in anisotropic triaxial compression. *Canadian Geotechnical Journal*, vol. 4, no. 1. pp. 68–86.
- LEE, I.K. and COOP, M.R. 1995. The intrinsic behaviour of a decomposed granite soil. *Géotechnique*, vol. 45, no. 1. pp. 117–130.
- LIU, H., XIA, Z., REN, F., and HE, R. 2019. Study on discrete element simulation of secondary rock failure characteristics in granular media. *Geotechnical and Geological Engineering*, vol. 37, no. 4. pp. 2503–2511.
- MANSO, J., MARCELINO, J., and CALDEIRA, L. 2021. Single-particle crushing strength under different relative humidity conditions. *Acta Geotechnica*, vol. 16, no. 3. pp. 749–761.
- MCDOWELL, G.R. and BOLTON, M.D. 1998. On the micromechanics of crushable aggregates. *Géotechnique*, vol. 48, no. 5. pp. 667–679.
- MCDOWELL, G.R. and HUMPHREYS, A. 2002. Yielding of granular materials. *Granular Matter*, vol. 4, no. 1. pp. 1–8.
- MERINO, L. 1986. Predicting the size distribution of ore fragments in block caving mines. MSc thesis, Imperial College, London.
- MIURA, N. and YAMANOUCHI, T. 1975. Effect of water on the behavior of a quartz-rich sand under high stresses. *Soils and Foundations*, vol. 15, no. 4. pp. 23–34.
- MORÉ, J.J. and SORENSEN, D.C. 1983. Computing a trust region step. *SIAM Journal on Scientific and Statistical Computing*, vol. 3. pp. 553–572.
- NAKATA, Y., HYDE, A.F.L., HYODO, M., and MURATA, H. 1999. A probabilistic approach to sand particle crushing in the triaxial test. *Géotechnique*, vol. 49, no. 5. pp. 567–583.
- NEDDERMAN, R.M. 1992. *Statics and Kinematics of Granular Materials*. Cambridge University Press.
- NICHOLAS, D. and SRIKANT, A. 2004. Assessment of primary fragmentation from drill core data. *Proceedings of Massmin 2004*. Instituto de Ingenieros de Chile. pp. 55–58.
- PIERCE, M., WEATHERLEY, D.K., and KOJOVIC, T. 2010. A hybrid methodology for secondary fragmentation prediction in cave mines. *Proceedings of Caving 2010*. Australian Centre for Geomechanics, Perth. pp. 567–582.
- REID, K.J. 1965. A solution to the batch grinding equation. *Chemical Engineering Science*, vol. 20, no. 11. pp. 953–963.
- YU, T.R. 1989. Some factors relating to the stability of consolidated rockfill at Kidd Creek. *Innovations in Mining Backfill Technology. Proceedings of the 4th International Symposium on Mining with Backfill*, Montreal, 2–5 October 1989. Vol. 4. Hassani, F.P., Scobie, M.J., and Yu, T.R. (eds). Balkema, Rotterdam. pp. 279–286.
- WOOD, D.M. and MAEDA, K. 2008. Changing grading of soil: Effect on critical states. *Acta Geotechnica*, vol. 3, article no. 3. ◆



Improving productivity at an open-pit mine through enhanced short-term mine planning

by T.J. Otto¹ and G.C. Lindeque¹

Affiliation:

¹Anglo American Kumba Iron Ore, South Africa.

Correspondence to:

T.J. Otto

Email:

theunis.otto@angloamerican.com

Dates:

Received: 16 Aug. 2021

Revised: 29 Sep. 2021

Accepted: 30 Sep. 2021

Published: November 2021

How to cite:

Otto, T.J. and Lindeque, G.C. 2021

Improving productivity at an open-pit mine through enhanced short-term mine planning.

Journal of the Southern African Institute of Mining and Metallurgy, vol. 121, no. 11, pp. 589–598

DOI ID:

<http://dx.doi.org/10.17159/2411-9717/1710/2021>

ORCID:

T.J. Otto

<https://orcid.org/0000-0002-3573-5627>

Synopsis

Productivity is improved by increasing the ratio of output to input. In an operating open-pit mine, improving the productivity of heavy mining equipment (HME) enables the unit cost of production to be reduced. To optimize HME productivity, the Kolomela open-pit iron ore mine transitioned to an enhanced short-term mine planning (STMP) process that supports the application of a manufacturing-type operating model. At the core of the enhanced STMP process is a focus on integration across the open-pit mining value chain. The interdependencies between mining activities are highlighted and emphasized, thus ensuring that mining activities are synchronized.

The improvements related to HME productivity were monitored from 2019 to 2020. The utilization of mining area in the Leeuwfontein pit improved from 71% to 90%, and the blasting frequency reduced by 14% while the average blast size increased by 17%. The distance travelled during shovel relocations between mining phases reduced by 16%, and the lost time associated with drills relocating reduced by 53%. These productivity improvements resulted in an 11% increase in the loading rate of the main waste shovel at Kolomela from 0.9 Mt/month in 2019 to 1.0 Mt/month in 2020. The enhanced STMP process can be adapted to other open-pit mining operations.

Keywords

open-pit mining, productivity, heavy mining equipment, short-term mine planning.

Introduction

One of the major objectives of mining companies is to minimize the unit cost of production at their operations. Lumley and McKee (2014) indicated that mining companies adopt one of two operational strategies to achieve this goal. The first strategy is a volume strategy, where the unit cost is reduced by increasing output (potentially at increased marginal cost). The second strategy is a cost reduction strategy, where the production output is stable but cost is minimized. Many open-pit mining operations have limited scope to increase output due to downstream constraints such as logistics and market demand. Therefore, a cost reduction strategy is often pursued.

Productivity improvement

According to Neingo and Tholana (2016), productivity is measured in different ways, which include indicators such as unit cost, output per employee, and output per unit capital equipment. In this paper the productivity indicator adopted is the output per unit capital equipment, *i.e.*, heavy mining equipment (HME) productivity. For the management of an operating open-pit mine, improving the productivity of the mining equipment is a major enabler for executing a cost reduction strategy. Productivity is improved when the ratio of output to input is increased. This could be achieved through more production output for a fixed input, the same production output for less input (a cost reduction strategy), or more production output for less input (Mitchell, 2017). Fundamentally, the goal is to get the maximum return from the capital invested in mining assets.

Lumley and McKee (2014) argued that for productivity improvements to be realized, open-pit mining operations need to pay attention to the efficiency of their HME fleets. The HME fleets represent a major capital investment and typically consist of rope and/or hydraulic shovels, front end loaders, haul trucks, blast-hole drills, and ancillary equipment. The aim of productivity improvements at many open-pit mining operations is to maximize the tons mined by the existing mining equipment fleet over a certain period in a safe and sustainable manner, while effectively executing the underlying mine plan. 'This means digging and hauling more dirt with each shovel and truck' (Lala *et al.*, 2016, p. 7).

Improving productivity at an open-pit mine through enhanced short-term mine planning

Between 2016 and 2020 many major mining companies turned their focus to a cost reduction strategy underpinned by productivity improvement as the preferred approach to reduce unit costs. The mining industry's focus on productivity improvements is delivering results. For example, the relationship between productivity improvements and unit cost reduction is clearly illustrated in the Anglo American 2019 interim results presentation. In the first half of 2019, Anglo American reported a 103% improvement in productivity and a resultant 27% reduction in unit cost from a 2012 base (Anglo American, 2019).

How did mining companies respond to the productivity improvement challenge and manage to improve the productivity of their open-pit mining operations? Broadly, two approaches were taken. Firstly, operational excellence programmes were rolled out with the aim of optimizing and improving processes across the open-pit mining value chain. Secondly, investments were made in technology and digitalization; this further enhanced the ability of open-pit mines to deliver reliable performance in line with productivity improvement targets. Mining companies followed diverse implementation methodologies, and some combined the two approaches. This paper focuses on the operational excellence approach.

Short-term mine planning

Mine planning, and specifically short-term mine planning (STMP), supports productivity improvements at open-pit mines. STMP plays a critical role in operational excellence programmes, which in turn results in improved HME productivity.

Mine planning can be defined as a process in mining engineering which transforms a mineral resource into the best productive mining business (Morales and Rubio, 2010). The mine planning process is cyclical, and mine plans are regularly updated to incorporate the latest available information and changes in the macro-economic environment (Vivas and Nava, 2014).

Most open-pit mining operations follow a systematic and disciplined mine planning process involving three distinct levels or horizons of planning, namely the long-term (strategic), medium-term (tactical), and short-term (operational) planning horizons (L'Heureux, Gamache, and Soumis, 2013). Each of these horizons represents a different level of risk and has different objectives. The planning horizons are nested in each other, and the mining plans with a longer timeframe pass down guidance and restrictions in decisions to the shorter-term plans. The main objectives at each of the planning horizons are firstly, to provide appropriate mine designs, and secondly, to determine the sequence in which material should be mined and processed to ensure that volume, blending, and equipment utilization targets are met (Burt *et al.*, 2015).

According to Blom, Pearce, and Stuckey (2019) long-term and short-term planning at open-pit mines differ in several dimensions. The main differences include:

- ▶ The level of detail modelled. Long-term plans use a grid of equally-sized blocks to define the orebody and typically do not consider the full suite of mining operational activities, while short-term plans are more practical, use irregularly-shaped blast blocks, and consider the precedence in the operational activities such as block preparation, drilling, blasting, loading, and hauling.
- ▶ The timeframe considered. Long-term plans cover the life-of-mine of an open-pit mine using quarterly to yearly

increments, while short-term plans cover a period of up to three months in daily and weekly periods.

- ▶ The level of decision-making. Long-term plans provide inputs to strategic decision-making such as the placement of major infrastructure and the timing of expansions, while short-term plans contribute to operational decisions such as plant throughput, feed quality, and blending considerations as well as the placement and utilization of HME.

STMP is important in that it provides a link between the guidance provided by the longer-term mining plans and the execution thereof. According to Upadhyay and Askari-Nasab (2018) the whole planning process at open-pit mines is ineffective when STMP is not done well. 'Short-term planning thus may be regarded as critical to achieve the mine's operational objectives and strategic targets.' (Upadhyay and Askari-Nasab, 2018, p. 153).

The STMP process consists of two main components. Firstly, the mine design component provides detailed designs for the mining activities within a phase or pushback of an open-pit mine. A high level of detail is important to ensure the planned excavations are safe and provide sufficient operating space. Access to the phase and mining benches must also be considered. This is achieved by designing mining blocks, access ramps, and infrastructure considering all the mining activities and the interactions between these activities in detail. Secondly, the mine scheduling component considers the sequence and timing of mining activities.

The time horizon for STMP spans several weeks to months. Blom, Pearce, and Stuckey (2017) referred to a STMP horizon of 13 weeks, and this is a typical duration for STMP at large open-pit mining operations. STMP is a rolling schedule that is updated weekly, fortnightly, or monthly, depending on the complexity and scale of the operation. STMP is typically conducted in detail on a day-to-day basis. The mining activities considered include access ramp construction, infrastructure establishment (such as electricity distribution and dewatering), block preparation, drilling, blasting, loading, and hauling.

Although the specific objectives prioritized and optimized by the STMP horizon vary from site to site and across various commodities, there are four main objectives for STMP that are defined as follows (Blom, Pearce, and Stuckey, 2019, 2017; Upadhyay and Askari-Nasab, 2018, 2017; Burt *et al.*, 2015; Vivas and Nava, 2014; De Souza e Silva, Moura, and Lanna, 1999):

- ▶ The effectiveness of the STMP, indicated by the plan's ability to achieve the production throughput and quality targets set by the longer-term plans
- ▶ The spatial alignment of the STMP to longer-term plans, considering deployment priorities for resources, thus ensuring spatial compliance to the longer-term planning horizon
- ▶ The way the STMP enables efficiency by optimizing (or maximizing) the productivity of HME
- ▶ Practical executability of the STMP through including a high level of detail in the STMP process, which contributes to the plan being realized in the field.

Ultimately, the aim of STMP is to ensure a detailed understanding of the critical mining path, related HME interactions and other constraints, and risks and opportunities that will result in achieving the four objectives of throughput and quality, alignment with longer-term plans, HME productivity,

Improving productivity at an open-pit mine through enhanced short-term mine planning

and executability. When an open-pit mine has an effective STMP process in place, accurate and detailed mine plans can be produced, communicated, and executed. This paper explores how a well-developed STMP process supports the implementation of operational excellence programmes at open-pit mines.

Manufacturing-type operating models underpinned by STMP

One of the key pathways to achieving operational excellence at open-pit mines is the implementation of manufacturing-type operating models. This reduces variability, leading to increased predictability. Wessels (2009) describes the implementation of a manufacturing-type operating model, referred to as the Business Process Framework (BPF), at AngloGold Ashanti. Figure 1 shows the major elements of this operating model.

The green block identifies the elements associated with STMP. The importance of planning ahead of execution is highlighted

by Wessels (2009, p. 18): ‘... if the work is planned, scheduled and properly resourced ahead of execution, the desired outcome will be achieved more consistently and at lower cost’. According to Wessels (2009), the BPF starts off by setting the strategy, business expectations, and performance targets, then planning and scheduling, followed by the execution of the work, and finally measuring and analysis of the results. This process design is also referred to as the ‘Plan, Do, Check, Act’ improvement cycle.

The Management Operating System (MOS) is another example of a manufacturing-type operating model. The operational systems map shown in Figure 2 represents the various elements of the MOS and how these elements are connected.

The MOS is a model used to manage people and processes to deliver results by reducing variability and steadily improving process performance (Moynagh, 2014). This manufacturing-type operating model connects plans with the work that is going on at

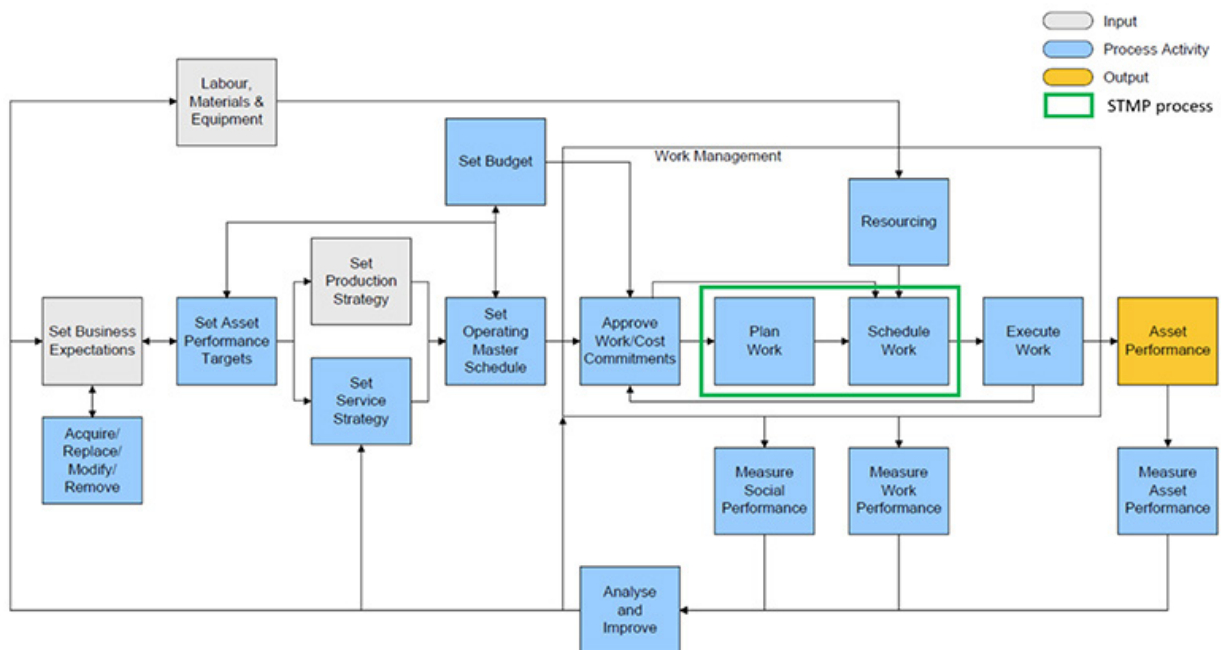


Figure 1—The major elements of the BPF manufacturing-type operating model (Wessels, 2009)

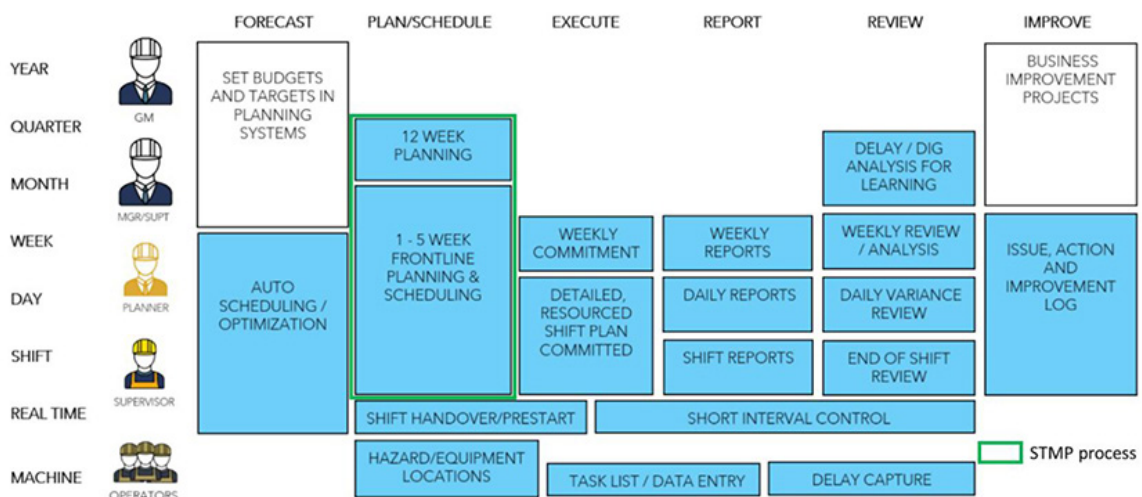


Figure 2—Operational systems map of the MOS manufacturing-type operating model (Moynagh, 2014)

Improving productivity at an open-pit mine through enhanced short-term mine planning

the front line with the aim of improving operational performance. Effective planning that connects the work to be done and the associated targets with the equipment required to achieve the planned results underpins the MOS manufacturing-type operating model (Moynagh, 2014). The green block in Figure 2 identifies the elements of the MOS associated with STMP.

Manufacturing-type operating models focus on detailed planning, standardized work, and disciplined execution (Lala *et al.*, 2016). Mysore (2019) indicated that mining companies are considering their operations as smart factories and are adopting the principles of lean manufacturing. An example of a mining company that has successfully implemented such a manufacturing-type operating model is Anglo American. In its 2019 interim results presentation, Anglo American (2019) stated that applying a manufacturing-type approach to mining had resulted in improved safety, reduced variability, and lower costs. BHP is also focusing on operational excellence in order to assist its businesses to work smarter and make its mines operate more like factories (Jurgens, 2017). Rio Tinto aims to improve productivity through focusing on operational excellence, thereby enhancing mining capacity and generating superior shareholder returns (Rio Tinto, 2016).

According to Aucamp (2020), operational excellence can be achieved by focusing on three areas – increased predictability (or reduced variability), one plan visible to all, and greater productivity. These focus areas have an optimal sequence, are interdependent, and have cause and effect relationships. Starting with one visible plan will reduce variability, which will lead to higher productivity. The optimal starting point for operational excellence programmes at open-pit mines is therefore at the mine planning stage, and specifically STMP.

Otto and Musingwini (2019) indicated that the quality and integrity of the mine planning process is of critical importance to ensure the effective operation of a large open-pit mine. Griesel *et al.* (2014) stated that the ability to generate consistent, practical, and accurate plans is central to achieving success in any mining environment. Detailed mine planning is required to mitigate variability, and reducing variability is the key to improving mining productivity (Geraghty *et al.*, 2015). A manufacturing-type approach to mining is implemented through efficient planning and execution of work (Anglo American, 2019). According to Lala *et al.* (2016), better mine planning and scheduling ensures a sustainable increase in overall equipment productivity and performance.

STMP models enable HME productivity improvements through, for example, minimizing the total mining cost considering aspects such as HME fleet utilization, haulage parameters, and re-handling cost, as well as drilling and blasting activities (Matamoros and Dimitrakopoulos, 2016; Eivazy and Askari-Nasab, 2012; L'Heureux, Gamache, and Soumis, 2013), minimizing shovel movements (Vivas and Nava, 2014; Upadhyay and Askari-Nasab, 2017), and optimizing ore and waste hauling cycles (De Souza e Silva, Moura, and Lanna, 1999). In order to achieve the HME productivity improvement objective, STMP should provide a set-up for highly efficient open-pit mining operations.

STMP should ensure a mining environment within which the operational key performance areas (KPA), such as maximizing HME fleet utilization and minimizing shovel movements, can be pursued and achieved. The creation of high-quality STMPs and the effective execution of these plans ensures that equipment

productivity at open-pit mining operations can attain its maximum potential (Vivas and Nava, 2014). Effective STMP, therefore, underpins the implementation of manufacturing-type operating models at open-pit mines with the aim of improving HME productivity.

Kolomela as a case study mine

The Kolomela iron ore mine (Kolomela) is owned and operated by Anglo American Kumba Iron Ore (Kumba). It is located in the Northern Cape Province of South Africa. Kolomela is an open-pit mining operation extracting high-grade iron ore and the associated waste material from four different pits. The mine is mainly a direct shipping ore (DSO) operation, and product size is controlled via a crushing and screening plant that receives feed from ROM buffer stockpiles and ex-pit ROM material. The final product is transported via a railway line to the Saldanha harbour for shipping to clients in Asia and Europe.

Kolomela makes a substantial contribution to the operational and financial performance of Kumba. In the 2020 financial year, the ex-pit mining tonnage at Kolomela was 71.6 Mt (approximately 200 kt/d). The total tons mined can be divided into 15.4 Mt of ex-pit ore and 56.2 Mt of ex-pit waste, resulting in a stripping ratio of about 4.6. Kolomela produced 11.7 Mt of saleable product in 2020 (Kumba Iron Ore, 2021). On 31 December 2020, Kolomela declared an Ore Reserve of 158 Mt at an average quality of 62.1% Fe. The Ore Reserve was calculated at a cut-off grade of 50% Fe and resulted in a reserve life of 12 years at the estimated production rate. The saleable product equated to 150 Mt at an average quality of 64.5% Fe (Rossouw and Nkambule, 2020). The 2020 Kolomela Reserve report was prepared in accordance with the guidelines of the SAMREC Code.

Kolomela is a conventional truck and shovel open-pit mining operation. All ex-pit material is obtained from drilling and blasting carried out on 10 m high benches. Hauling operations ensure that the ex-pit ore arrives at the correct primary crushing or ROM stockpile location, while waste is dumped on waste dumps or back into previously created voids as part of an in-pit rehabilitation process. The aim of the bulk waste mining is high mining equipment efficiency to reduce the mining cost, while the ex-pit ore mining is a selective mining process with a focus on clean extraction of the ore. A hybrid model of owner mining and contractor mining is employed, with approximately 75% of the operation conducted with the owner mining fleet. Mining activities take place in four distinct open pits called Leeuwfontein (LF), Klipbankfontein (KBF), Kapstevél-North (KSN), and Kapstevél-South (KSS). Figure 3 is a satellite image representing the layout of Kolomela, showing the four active pits, major waste dumps, and the processing facility.

The primary mining equipment deployed at Kolomela includes:

- ▶ **Drilling:** six Caterpillar MD6540 drills drilling 251 mm diameter blast-holes
- ▶ **Loading:** two Liebherr R996 hydraulic face shovels for pre-strip waste mining, four Komatsu PC3000 hydraulic face shovels for waste and ore mining, two Liebherr R9150 hydraulic excavators for selective ore mining, and four front-end loaders for flexible loading in the pit and re-handling of ROM ore stockpiles
- ▶ **Hauling:** 26 Komatsu 730E trucks (190 t capacity) and 17 trucks of 100 t capacity each, comprising a mix of Komatsu 785 and Caterpillar 777 trucks.

Improving productivity at an open-pit mine through enhanced short-term mine planning

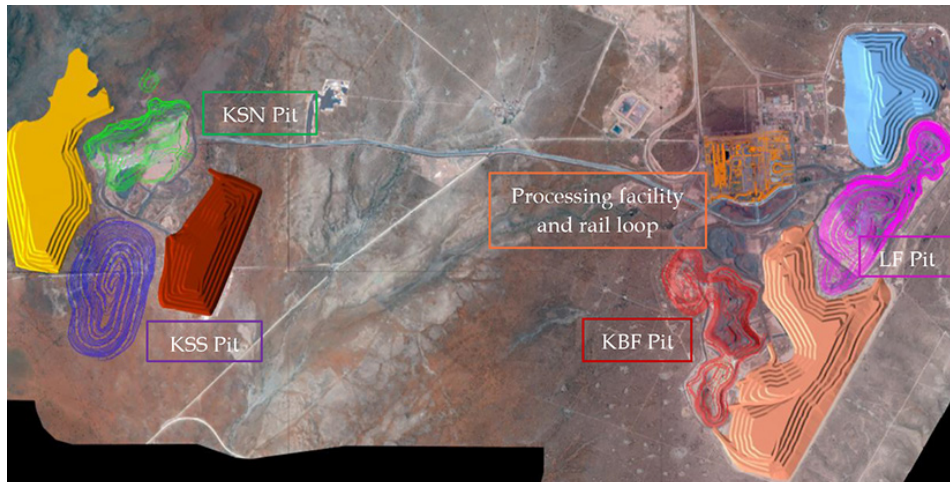


Figure 3—Satellite image of the Kolomela mine (Rossouw and Nkambule, 2020)

Currently, Kolomela's production output is limited by the mine's export rail capacity allocation. Due to this logistical constraint, Kolomela must follow a cost reduction strategy. The mine strives to reduce the unit cost of production by improving productivity across the mining value chain, including HME productivity. This is achieved by implementing a manufacturing-type operating model that enables operational excellence. Effective STMP is a key enabler for the successful implementation of the manufacturing-type operating model at Kolomela, and is therefore key in improving the HME productivity.

Short-term mine planning at Kolomela

The main objectives of STMP at Kolomela are to:

- Deliver on the requirements from the annual business plan (BP) in terms of tonnage mined and fed to the processing plant as well as product quality
- Achieve spatial compliance to the BP
- Increase HME productivity
- Provide a mine plan with a high degree of executability.

STMP therefore addresses both effectiveness and efficiency by focusing on meeting the annual BP targets and optimizing HME productivity.

To ensure HME productivity is improved, Kolomela transitioned to an integrated, highly detailed, and visual modelling-type STMP process during 2019. State-of-the-art mine planning applications were introduced to support the process by integrating STMP across the four pits and providing a visual model of mining activities and HME deployment. This STMP process contributed to reducing variability and increasing the predictability of mining execution.

Effective STMP is a key enabler for a manufacturing-type approach to mining at Kolomela that targets improvements in HME productivity. STMP increases the predictability of mining execution by identifying and mitigating HME deployment bottlenecks and spatial deployment challenges that could result in a deviation from the short-term plan. This is achieved through the high level of detail in which the STMP is developed. Seven primary and secondary mining activities are planned and scheduled as part of the STMP process at Kolomela. The STMP process provides a detailed and practically executable plan which includes all the relevant activities in the open-pit mining cycle as shown in Figure 4.

To achieve the required level of predictability in mining execution, the STMP process also utilizes visual mine planning applications and communication approaches. This ensures that the mining execution teams fully understand the mining sequence and HME productivity improvement opportunities. Communication includes aspects such as mining priorities, the location of all planned infrastructure, and access points, haulage routes, *etc.* One such communication tool is the bi-weekly pit plan as shown in Figure 5.

The short-term plan is summarized for each pit on these plans, which are widely distributed. The plan shows the designed mining blocks of active mining levels, draped over the latest aerial image of the mining area. The mining blocks are colour-coded, indicating the current stage in the mining cycle on active blocks. A block-per-block mining sequence per activity in the mining cycle is also displayed. The forward-looking view of the mining sequence ensures alignment between the execution team and the planning department regarding the direction of the short-term plan. The STMP process provides the mining execution teams with a visual step-by-step guide to achieve the BP requirements, ensuring optimal HME deployment and productivity.

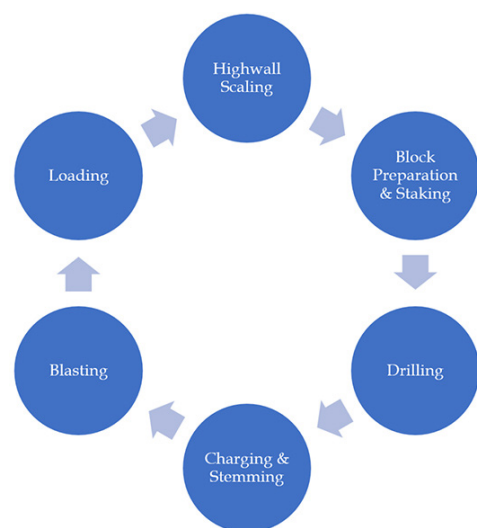


Figure 4—Open-pit mining activities scheduled as part of the STMP process at Kolomela

Improving productivity at an open-pit mine through enhanced short-term mine planning

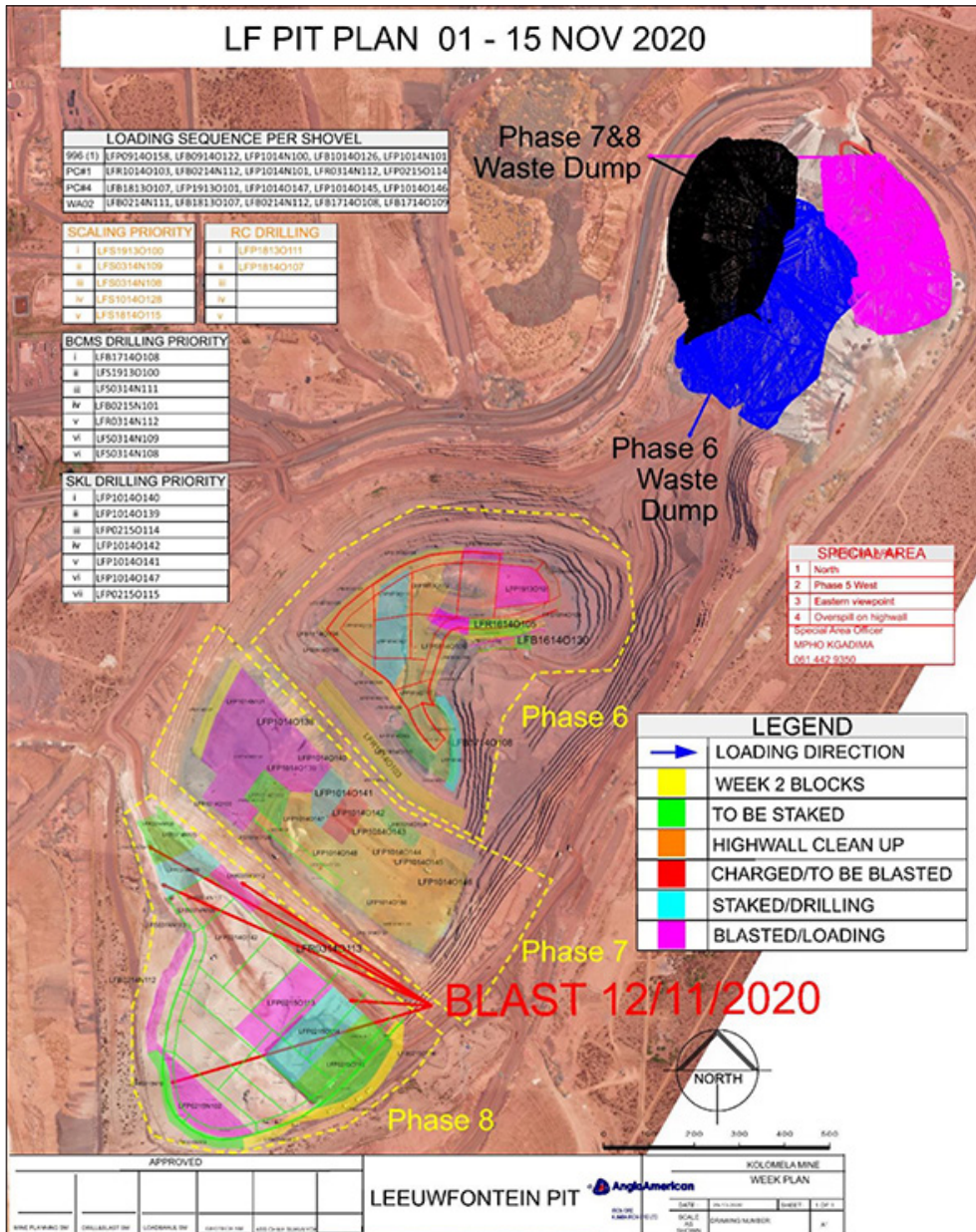


Figure 5—Bi-weekly pit plan for LF pit (Lindeque, 2020)

At the core of effective STMP is a high level of integration across the open-pit mining value chain. The interdependencies between activities in the mining cycle are highlighted and emphasised. This enables the STMP team to produce a plan in which all the mining activities are synchronized. Improved HME productivity starts with the synchronized deployment of mining equipment across the open pits at Kolomela, taking a holistic view of the mining sequence and priorities, thus ensuring that the correct areas are mined at the correct time by the correct equipment at optimal efficiencies. The mining activities at Kolomela are highly interdependent, therefore the accuracy of HME deployment and capacity assumptions is crucial to achieving a high level of synchronization between the mining activities, which in turn increases the predictability of the mining execution.

Figure 6 is an example of the mining cycle in LF Phase 7, illustrating the integrated and visual approach to STMP at Kolomela. The complete STMP is animated and the mine planner

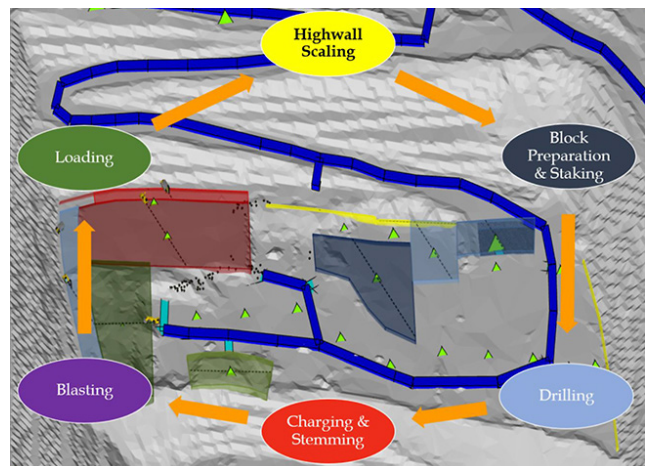


Figure 6—Example of the typical mining cycle in LF Phase 7

Improving productivity at an open-pit mine through enhanced short-term mine planning

can easily move through the schedule, visualize the deployment of HME, and confirm the synchronization between mining activities.

The STMP routines at Kolomela are standardized to fully align with the routines of the greater mining value chain. A key factor for the successful execution of the STMP is effective interaction and alignment with the mining execution teams. Figure 7 shows the key events in the STMP routine.

A new short-term plan is released bi-weekly and serves as a high-confidence forecasting tool that highlights risks and opportunities in the STMP horizon, which covers 12 weeks. At the core of the STMP routine is the bi-weekly planning meeting where a new short-term plan is presented and agreed upon. Progress against the short-term plan is tracked daily in the production meetings, where the short-term plan is used to guide the spatial mining execution and to highlight risks and opportunities. Real-time data from across the mining value chain, such as actual shovel bucket positions per load, drill-hole data, equipment positions, and maintenance schedule, is consolidated in the STMP applications. Such real-time data enables the planners to always be up to date with developments in the field and facilitates constructive discussion with the execution team in their daily interactions. This ensures that the guidance provided by the short-term plan, and the subsequent decisions made, are based on the most accurate spatial data available. On a weekly basis, the plan is discussed in the field during pit visits and reviewed during schedule review meetings to confirm continued alignment between mine planning and mining execution. Following the pit visits and schedule review meetings, which are attended by representatives from all sections in the technical and mining departments, the short-term mining plan is updated to incorporate major unforeseen changes.

The enhanced STMP process increased the predictability of open-pit mining at Kolomela between 2019 and 2020. The integrated, detailed and more visual STMP process and associated routines underpin the implementation of a manufacturing-type operating model at Kolomela, thereby reducing variability and contributing to improved HME productivity. The short-term mining plan at Kolomela outlines how HME fleets should be deployed and how planned tasks interact with each other to deliver daily, weekly, and monthly production targets.



Figure 7—Kolomela STMP routines

Impact on HME productivity

The main objective of transitioning to a more integrated and visual STMP process at Kolomela was to improve HME productivity. As discussed before, this was achieved by increasing the predictability of open-pit mining execution through detailed, more visual and integrated STMP. The direct HME productivity-related improvements that can be attributed to the enhanced STMP process are:

- Improved utilization of the mining area
- Optimal blast planning
- Reduction in HME relocations.

The improvements in HME productivity-related metrics over a period of two years, from 2019 to 2020, are discussed in the next sections. For illustrative purposes, the data presented is for Phase 7 of the LF pit, which is the main open-pit mining area at Kolomela. More than 30% of the total ex-pit waste tons at Kolomela in the two-year period under consideration were produced from LF Phase 7. The main waste stripping shovel at Kolomela, a Liebherr R996 hydraulic face shovel (996#1), was deployed in this mining area.

Improved utilization of mining area

Utilization of mining area (UMA) refers to the effective use of the available mining area per mining phase and is defined as the ratio of productive area to total available mining area (Equation [1]).

$$Utilisation\ of\ Mining\ Area\ (UMA) = \frac{Productive\ Area}{Total\ Available\ Mining\ Area} \quad [1]$$

The total available mining area is defined as the surface area per mining phase, excluding the permanent ramp system. The total available mining area can be divided into two distinct sub-areas:

- *Productive area*: any area within a mining phase where it is possible for one or more activities in the mining cycle (shown in Figure 4) to take place
- *Non-productive area*: areas within a mining phase where no activity in the mining cycle can take place – for example, areas are categorized as non-productive when used as a hauling route or a temporary ramp.

The quality of the STMP has a direct effect on the UMA. A high level of integration and synchronization between the mining activities ensures that the productive mining area is maximized, resulting in improved HME productivity. To achieve the planned ex-pit waste tons as well as the productivity targets for the 996#1 shovel, the effective utilization of available mining area in LF Phase 7 was crucial.

To demonstrate the improvement in the UMA because of the improved STMP process, Figure 8 illustrates how the available mining area in LF Phase 7 was utilized in December 2019 (left) compared to October 2020 (right). The areas are characterized as follows:

- Productive area: available drill area (blue) and drilled or blasted floor stock (green)
- Non-productive areas: temporary ramps (red) and hauling area (yellow).

A comparison of the UMA for December 2019 and October 2020 shows that the productive area increased while the non-

Improving productivity at an open-pit mine through enhanced short-term mine planning

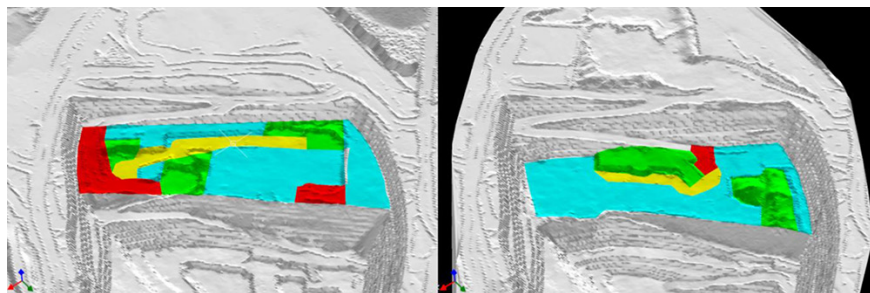


Figure 8—Leeuwfontein Phase 7 UMA: visual comparison of December 2019 and October 2020 topography

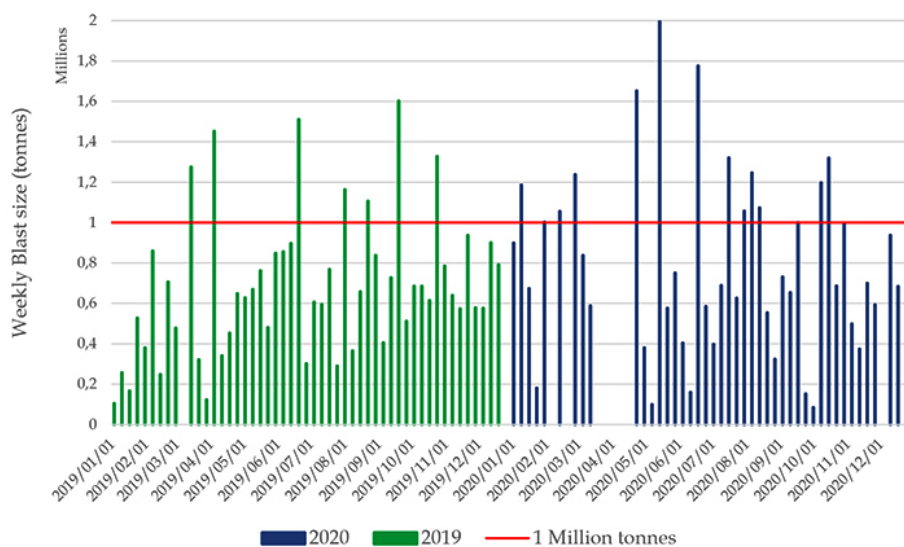


Figure 9—Leeuwfontein blast frequency and blast size – comparison of 2019 and 2020 results

productive areas decreased. The UMA increased from 71% to 90%, confirming the improved integration and synchronization of mining activities achieved through enhanced STMP.

Optimal blast planning

The blasting of ore and waste before loading is standard practise at Kolomela to ensure optimal fragmentation and high shovel productivity. To ensure safe blasting, the HME is relocated to a position outside the blasting radius of 500 m and all personnel evacuate to safe positions further than 800 m from the blast. Blasting disrupts the open-pit mining activities. For example, 4 hours of production time is typically lost at LF from the time that HME relocation starts to the point where the pit is declared safe again and the HME is back in production. Therefore, it is important that blasting activities are well planned to minimize the impact of blasting on production.

To minimize the impact of blasting on production, the frequency of blasting needs to be reduced without jeopardising the blasted floor stock levels. This is achieved by increasing the blast size and clustering the blocks to be blasted based on their location. It is best practice to blast a cluster of blocks in the same area of the pit, since this minimizes the production loss due to relocating of equipment. For example, if the blast is restricted to a specific phase of the pit, the production loss for equipment deployed in the other phases is significantly reduced. Figure 5 indicated a good example of cluster blasting by location for a weekly outlook; only blocks in Phase 8 (indicated by red arrows in Figure 5) of LF were planned for blasting during that specific week.

The enhanced STMP process at Kolomela improved blast planning, which had a positive impact on HME productivity. Figure 9 compares the number and size of weekly blasts in 2019 (green) with those in 2020 (blue) in the LF pit.

The figure indicates that there was a 14% reduction in blasting frequency from 2019 to 2020. This was possible due to a 17% increase in the average blast size; from 0.68 Mt in 2019 to 0.8 Mt in 2020. There was also a 114% increase in blasts of more than 1 Mt; from 7 blasts in 2019 to 15 blasts in 2020. The increase in average blast size ensured an increase in loading rate.

The reduction in the frequency of blasting also had a positive impact on overall productivity since less time was lost due to HME relocation associated with blasting activities. From 2019 to 2020 there was a 33% reduction in production time lost for the 996#1 shovel due to blasting activities. These productivity improvements due to improved blast planning are reflected in the improved utilization of the shovel.

Reduction in HME relocation

To achieve and maintain high HME productivity, the HME should be optimally utilized for productive activities and time associated with non-productive activities should be minimized. One of the non-productive activities in open-pit mining is the relocation or re-positioning of shovels and drills between mining areas. Excessive relocation of HME has a negative impact not only on short-term productivity, but also a longer-term impact on engineering availability due to the strain on the equipment when it is relocated over long distances. Therefore, it is important that the short-term mining plan deploys HME in such a way that

Improving productivity at an open-pit mine through enhanced short-term mine planning

relocation, and specifically relocation between mining phases, is minimized.

To illustrate how the enhanced STMP process reduced the non-productive time associated with the relocation of shovels at Kolomela, the coordinates of each bucket loaded by the 996#1 shovel over the two-year period from 2019 to 2020 were analysed. For the purpose of the analysis, all relocations of the shovel greater than 400 m were categorized as inefficient, as a relocation distance of greater than 400 m typically represents a movement of the shovel between mining phases. This constitutes non-productive relocation that effective STMP should minimize. Figure 10 shows a decrease in the frequency at which the 996#1 shovel travelled for a distance greater than 400 m between 2019 and 2020. The distance travelled is defined as the horizontal difference between the x and y coordinates of consecutive shovel bucket loads, and does not consider elevation difference or actual distance of the travelled path on haul roads and ramps. The distances in Figure 10 thus represent much larger actual distances travelled to achieve a horizontal difference in consecutive bucket loads greater than 400 m.

There was a 16% reduction in the distance travelled, which implies a reduction in time associated with non-productive activities, indicating that the enhanced STMP process improved

the productive utilization of the 996#1 shovel.

The enhanced STMP process also resulted in significant productivity improvements for the primary blast-hole drill fleet at Kolomela. This was achieved by ensuring that drill relocation is minimized. To illustrate the positive impact of the enhanced STMP process on drill productivity, the non-productive reporting time codes of Drill Relocating were analysed over the two-year period from 2019 to 2020. Figure 11 shows the cumulative downtime per month due to Drill Relocating, expressed as a percentage of the total available time for the fleet of six Caterpillar MD6540 drills at Kolomela over the two-year period.

The figure shows a gradual decreasing trend in production loss due to relocation of drills between 2019 and 2020. The percentage of total available time lost due to drill relocation reduced from 19% in 2019 to 9% in 2020. This represents a 53% reduction in production loss. This analysis points to a higher level of integration and synchronization in the mining cycle and shows the positive impact of the enhanced STMP process on drill productivity.

Conclusion

Mining companies implementing cost reduction strategies have found that improving HME productivity leads to a reduction in

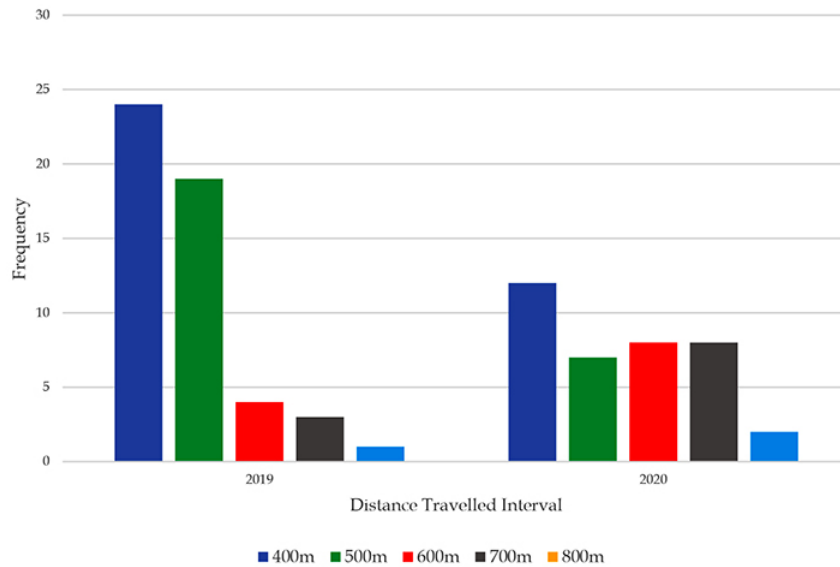


Figure 10—Frequency of travelling per non-productive distance interval (>400 m)

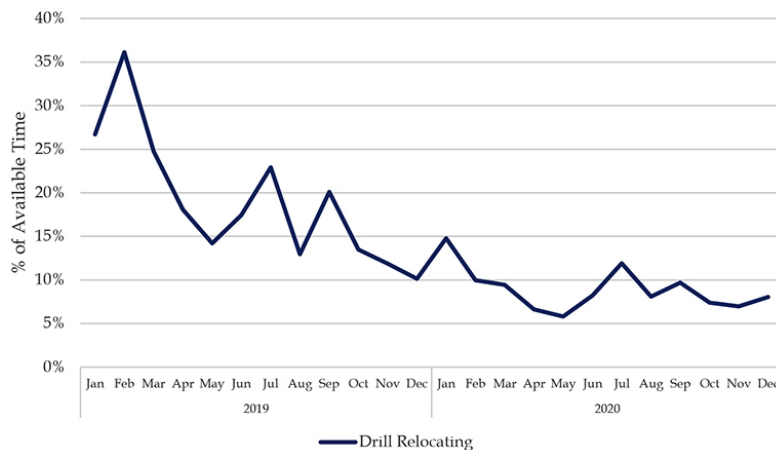


Figure 11—Downtime booking of drill fleet (2019–2020)

Improving productivity at an open-pit mine through enhanced short-term mine planning

the unit cost of open-pit mining operations. These companies often implement manufacturing-type operating models to support operational excellence programmes. These models improve HME productivity by focusing on detailed planning and reducing variability, thereby increasing the predictability of mining execution. At Kolomela, the STMP process underpins the application of a manufacturing-type operating model to mining. A detailed, integrated, and more visual STMP process increases the predictability of mining execution, thus, enabling the implementation of a manufacturing-type operating model. The short-term mining plan outlines how the HME should be deployed and how planned mining activities interact with each other. The implementation of this manufacturing-type approach to mining at Kolomela has contributed to improved HME productivity.

During 2019, enhancements were made to the STMP process at Kolomela to support the manufacturing-type approach to mining. The STMP process provides the mining execution teams with a step-by-step guide to achieve the BP requirements, while ensuring optimal HME deployment and productivity. The implementation of the enhanced STMP process at Kolomela resulted in significant HME productivity improvements. The direct impacts of the improvements from 2019 to 2020 were observed in three key drivers of HME productivity, namely:

- The UMA in Phase 7 of the LF pit improved from 71% to 90%
- The blasting frequency in the LF pit reduced by 14% and the average blast size increased by 17%, resulting in a 33% reduction in production time lost due to blasting activities for the 996#1 shovel
- A reduction in HME relocation. The distance travelled, associated with the 996#1 shovel relocating between mining phases reduced by 16%, and the lost time associated with the relocation of drills reduced by 53%.

These productivity improvements resulted in an 11% increase in the loading rate of the main waste shovel at Kolomela from 0.9 Mt/month in 2019 to 1.0 Mt/month in 2020. In addition to the quantitative HME productivity improvements, the increased predictability of mining execution contributed to the mine safely achieving production targets in line with the BP expectations. Effective STMP enables the implementation of a manufacturing-type approach to mining at Kolomela and is a key contributor to the mine delivering on BP expectations and HME productivity improvement. The approach presented in this paper can be adapted by other open-pit mining operations to improve HME productivity.

Acknowledgements

The permission granted by the management of Anglo American Kumba Iron Ore to publish this paper is gratefully acknowledged.

References

- ANGLO AMERICAN. 2019. Interim 2019 Annual Results presentation, 25 July 2019. 95 pp. <https://www.angloamerican.com/~media/Files/A/Anglo-American-Group/PLC/media/presentations/2019pres/interim-results-2019-presentation.pdf> [Accessed 28 October 2020].
- AUCAMP, J. 2020. Integrated planning and short interval control for rapid improvements in safe production. *Proceedings of the Digitalization in Mining Conference*, July 2020. Southern African Institute of Mining and Metallurgy, Johannesburg.
- BLOM, M., PEARCE, A.R., and STUCKEY, P.J. 2017. Short-term scheduling of an open-pit mine with multiple objectives. *Engineering Optimization*, vol. 49, no. 5. pp. 777–795.
- BLOM, M., PEARCE, A.R., and STUCKEY, P.J. 2019. Short-term planning for open pit mines: a review. *International Journal of Mining,*

Reclamation and Environment, vol. 33, no. 5. pp. 318–339, doi: 10.1080/17480930.2018.1448248.

- BURT, C.N., LIPOVETZKY, N., PEARCE, A.R., and STUCKEY, P.J. 2015. Scheduling with fixed maintenance, shared resources and nonlinear feedrate constraints: A mine planning case study. *Proceedings of the International Conference on Integration of Constraint Programming, Artificial Intelligence, and Operations Research (CPAIOR 2015)*. Springer. pp. 91–107.
- DE SOUZA E SILVA, K., MOURA, M.M., and LANNA, O. 1999. Short term mine planning: Selection of working sites in iron ore mines. *APCOM '99: Proceedings of the 28th International Symposium on Computer Applications in the Minerals Industry*, Colorado School of Mines, Golden, CO, 20–22 October 1999. -Colorado School of Mines. pp. 763–770.
- EIVAZY, H. and ASKARI-NASAB, H. 2012. A mixed integer linear programming model for short-term open pit mine production scheduling. *Mining Technology*, vol. 121. pp. 97–108.
- GERAGHTY, R., PUJOL, F., SELLSCHOP, R., and DURRANT-WHYTE, H. 2015. How digital innovation can improve mining productivity. *McKinsey Metals & Mining Practice*, November 2015. pp. 1–14.
- GRIESEL, L., BUXTON, C., ADAMS, C., and BERRYMAN, T. 2014. The superpit schedule model – A time-efficient data-driven estimation for short- and medium-term planning. *Proceedings of the Ninth International Mining Geology Conference*, Adelaide, SA, 18–20 August 2014. Australasian Institute of Mining and Metallurgy, Melbourne. pp. 397–409.
- JURGENS, D. 2017. BHP Which technologies will boost mining safety and productivity? <https://www.bhp.com/media-and-insights/prospects/2017/11/which-technologies-will-boost-mining-safety-and-productivity/> [Accessed 28 October 2020].
- KUMBA IRON ORE. 2021. Kumba Iron Ore 2020 Annual Results Presentation. 45 pp. <https://www.angloamericankumba.com/~media/Files/A/Anglo-American-Group/Kumba/media/annual-results-presentation-2020-v1.pdf> [Accessed 15 May 2021].
- LALA, A., MOYO, M., REHBACH, S., and SELLSCHOP, R. 2016. Productivity at the mine face: Pointing the way forward. *McKinsey & Company Metals & Mining*, August 2016. pp. 1–12.
- L'HEUREUX, G., GAMACHE, M., and SOUMIS, F. 2013. Mixed integer programming model for short term planning in open-pit mines. *Mining Technology*, vol. 122. pp. 101–109.
- LINDEQUE, G.C. 2020. November 2020 12-week mine plan for the Leeuwfontein pit, Kumba Iron Ore, November 2020. pp. 1–12.
- LUMLEY, G. and MCKEE, M. 2014. Mining for efficiency 128 pp. https://www.researchgate.net/profile/Graham-Lumley/publication/301880114_Mining_for_Efficiency/links/572a7c9e08aef7c7e2c4fb0d/Mining-for-Efficiency.pdf [Accessed 27 September 2020].
- MATAMOROS, M.E.V. and DIMITRAKOPOULOS, R. 2016. Stochastic short-term mine production schedule accounting for fleet allocation, operational considerations and blending restrictions. *European Journal of Operational Research*, vol. 255, no. 3. pp. 911–921.
- MITCHELL, P. and STEEN, J. 2017. Productivity in mining – A case for broad transformation. *EY Mining & Metals*. pp.1–8.
- MOYNAGH, P. 2014. How does a management operating system help improve performance. Management Operating System - Fewzion Work Management Software <https://fewzion.com.au/management-operating-system/> [Accessed 27 July 2021].
- MORALES, C. and RUBIO, E. 2010. Development of a mathematical programming model to support the planning of short-term mining. *APCOM 2010*. pp. 3–15.
- MYSORE, P. 2019. Lean mining and the fourth industrial revolution. *Mining Journal*. <https://www.mining-journal.com/innovation/partner-content/1371028/lean-mining-and-the-fourth-industrial-revolution> [Accessed 27 September 2020].
- NEINGO, P.N. and THOLANA, T. 2016. Trends in productivity in the South African gold mining industry. *Journal of the Southern African Institute of Mining and Metallurgy*, vol. 116, no. 3. pp. 283–290.
- OTTO, T.J. and MUSINGWINI, C. 2019. A spatial mine-to-plan compliance approach to improve alignment of short-term and long-term mine planning at open-pit mines. *Journal of the Southern African Institute of Mining and Metallurgy*, vol. 119, no. 3. pp. 253–259.
- RIO TINTO. 2016. Rio Tinto outlines new \$5 billion productivity push under long-term strategy focused on cash generation. <https://www.riotinto.com/news/releases/5bn-productivity-push-outlined> [Accessed 27 September 2020].
- ROSSOUW, N. and NKAMBULE, S. 2020. Kolomela mine: Ore reserve (and saleable product) statement 2020, 31 October 2020. 146 pp.
- UPADHYAY, S.P. and ASKARI-NASAB, H. 2017. Dynamic shovel allocation approach to short-term production planning in open-pit mines. *International Journal of Mining, Reclamation and Environment*, vol. 33, no. 1. pp.1–20. doi:10.1080/17480930.2017.1315524
- UPADHYAY, S.P. and ASKARI-NASAB, H. 2018. Simulation and optimization approach for uncertainty-based short-term planning in open pit mines. *International Journal of Mining Science and Technology*, vol. 28. pp. 153–166.
- VIVAS, R.E. and NAVA, A. 2014. An integrated mine plan - connecting long, medium- and short-term planning strategies at Goldcorp Penasquito. *Mining Engineering Magazine*, vol. 66, no. 12. pp. 29–34.
- WESSELS, S. 2009. Analysing the success and determining the key success factors of a process improvement initiative within AngloGold Ashanti Limited. MBA thesis, University of Cape Town. 149 pp. ◆



Behaviour of Cu, Fe, Ni, and PGMs during leaching of Ni-Fe-Cu-S converter matte

by A.P. Van Wyk¹, G. Akdogan¹, and S.M. Bradshaw¹

Affiliation:

¹Department of Process Engineering, Stellenbosch University, South Africa.

Correspondence to:

A.P. Van Wyk

Email:

apvanwyk@sun.ac.za

Dates:

Received: 2 Feb. 2021

Revised: 1 Apr. 2021

Accepted: 13 Oct. 2021

Published: November 2021

How to cite:

Van Wyk, A.P., Akdogan, G., and Bradshaw, S.M. 2021
Behaviour of Cu, Fe, Ni, and PGMs during leaching of Ni-Fe-Cu-S converter matte.

Journal of the Southern African Institute of Mining and Metallurgy, vol. 121, no. 11, pp. 599–606

DOI ID:

<http://dx.doi.org/10.17159/2411-9717/1608/2021>

ORCID:

A.P. Van Wyk

<https://orcid.org/0000-0003-2006-8355>

G. Akdogan

<https://orcid.org/0000-0003-1780-4075>

S.M. Bradshaw

<https://orcid.org/0000-0001-6323-8137>

Synopsis

In the mineral processing industry, Ni-Cu-Fe-S converter matte is leached to remove base metals from a concentrate containing platinum group metals (PGMs). We investigated the atmospheric leaching process to develop a better understanding of the leaching behaviour of the base metals (Cu, Fe, and Ni) and the PGMs, in particular Ru, Ir, and Rh with respect to key process variables, acid concentration, and Cu concentration under oxidative and non-oxidative conditions.

With oxidative leaching, a higher initial acid concentration resulted in higher Cu, Ni, and Fe extractions, as well as faster leaching reaction rates. A higher initial acid concentration also resulted in faster precipitation of Cu, Ru, and Ir under oxidizing conditions.

Under non-oxidative conditions, Ni and Fe extraction was much slower, and the effect of initial acid concentration on Cu precipitation was less pronounced. The initial Cu concentration had a slightly smaller effect on the leaching behaviour of Fe and Ni, as well as precipitation of Ru, Ir and Rh. Moreover, a higher initial Cu concentration suppressed both Ni and Fe leaching and had a slight inhibiting effect on the precipitation behaviour of Cu, Ru, and Ir.

Keywords

platinum group metals, converter matte, leaching, precipitation.

Introduction

The largest platinum group metal (PGM) deposit in the world, located in the Bushveld Complex in South Africa, holds half of the world's platinum group elements (PGEs) and chromium. Smelting and processing of the PGM concentrates in this region is carried out by four major companies, namely Anglo American Platinum, Impala Platinum, Sibanye-Stillwater, and Northam Platinum (Jones, 2005).

Due to their unique physical and chemical properties such as good corrosion and oxidation resistance, high melting temperatures, good conductivity, and electronic and catalytic properties, the PGMs are used for their superior performance in certain industries and markets. These applications include (i) platinum or rhodium as autocatalysts to reduce greenhouse gas emissions produced by the combustion of fossil fuels, (ii) platinum and palladium jewellery, (iii) catalysts in the chemical sector, (iv) electrical equipment and electronic devices, (v) platinum used in the manufacturing of glass, and the (vi) production of drugs in the medical sector (Creamer, 2006). Moreover, platinum-catalysed hydrogen-powered fuel cells for electric vehicles (EVs) offer the most natural solution for emission-free vehicles, discharging only water and requiring negligible changes to current driving and refuelling habits (Theron-Ord, 2017).

The Sibanye-Stillwater (formerly Western Platinum) process involves milling, flotation, and smelting followed by Peirce-Smith converting to produce a Ni-Cu-Fe-S converter matte containing PGMs. The base metals and sulphur contained in the converter matte are removed through a multi-stage leaching process. The first stage leach, also known as the atmospheric leach, serves to remove Ni from the matte, while at the same time precipitating Cu and the PGMs from the leaching solution. Due to very little insight into the mechanisms of the atmospheric leaching process, studies conducted by Hofirek and Kerfoot (1992), Lamy and Lorenzen (2006), van Schalkwyk *et al.* (2011) and Snyders *et al.* (2018) were aimed at investigating the chemistry and mechanism of the process, as well as determining the effects of Fe endpoints, initial acid and Cu concentrations of the spent electrolyte solutions, and oxidative/non-oxidative conditions on the leaching behaviour of Ni-Cu-Fe-S converter mattes.

Behaviour of Cu, Fe, Ni, and PGMs during leaching of Ni-Fe-Cu-S converter matte

The purpose of atmospheric leaching is to firstly leach the Ni from the matte, while at the same time rejecting the Cu from the solution, through metathesis reactions. Leaching takes place in five continuously stirred tank reactors (CSTRs) in series, with oxygen fed to the first three tanks only. The acid supplied to the first tank is spent electrolyte solution recycled from the copper electrowinning tankhouse and which contains 20–30 g/L Cu and 80–90 g/L sulphuric acid. Sulphuric acid make-up is only added during upset conditions on the plant. A Ni crystallizer bleed stream is added to the first stage leach in order to recovery any Cu that may have slipped through to the Ni crystallizer unit. The operating temperature of the first stage circuit is 85°C (Crundwell *et al.*, 2011). The metathesis reactions serve to exchange Cu from the solution with Ni from the alloy and nickel sulphide phases in the matte. The PGMs present in the matte, along with the Cu, report to the leach residue (van Schalkwyk *et al.*, 2011.)

In this project we investigated the first stage atmospheric leaching process of the converter matte, using base metal refinery (BMR) spent electrolyte from Sibanye-Stillwater, in order to develop a better understanding of the effect of the initial acid and Cu concentrations on the leaching behaviour of the base metals, in particular Fe and Ni, as well as Rh, Ir, and Ru, under oxidative and non-oxidative conditions. A better understanding of the process will assist in improving the process efficiency.

Experimental

Equipment

Atmospheric leaching tests were carried out in a 6 L stainless steel batch reactor with an active volume of 4 L. The reactor set-up was geometrically scaled down from the atmospheric leaching reactors used at the Sibanye-Stillwater BMR. The temperature during the experiments was kept constant at 85°C by using a PID controller. Cooling coils which provided a constant flow of cooling water were mounted inside the vessel to remove the excess heat generated by the exothermic leaching reactions. To monitor the temperature, a thermocouple was placed inside the reactor. The vessel was fitted with a liquid sampling port to draw samples at set intervals. To ensure perfect mixing of the reactor contents a stirrer fitted with two agitation blades was used, and the reactor was fitted with four baffles to promote turbulent mixing. During oxidative leaching tests, oxygen was supplied from an oxygen cylinder and delivered to the reactor contents through a stainless-steel sparger. The flow rate of oxygen was regulated by a manual flow control valve and measured by a flow meter.

Table I

Quantitative XRD analysis of the converter matte

Phase	Formula	Abundance (wt%)
Heazlewoodite	Ni ₃ S ₂	65.26
Chalcocite	Cu ₂ S	20.09
Cu-Ni alloy	CuNi	13.27
Magnetite	Fe ₃ O ₄	0.57

Table II

Bulk chemical composition of matte sample (wt%)

	Sample 1	Sample 2	Sample 3	Mean	Std. dev.
Cu	29.36	28.81	29.79	29.32	0.49
Ni	49.31	52.37	51.79	51.16	1.63
Fe	0.16	0.19	0.17	0.18	0.02
S (balance)	21.18	18.63	18.24	19.35	0.02

The sparger was designed in an 'L' shape, with small equally-spaced holes in the bottom to disperse small oxygen bubbles to the reactor contents. The oxygen entered the reactor vessel through a stainless steel tube with holes at the bottom to ensure that sufficient oxygen bubbles were provided to the reactor contents. A Liebig condenser was fitted to the reactor set-up to reduce the evaporation rate of the contents. Along with the Liebig condenser, a rubber O-ring was placed between the reactor vessel and reactor lid to ensure that vapours formed did not escape.

Materials

Granulated converter matte provided by Sibanye-Stillwater was analysed by quantitative XRD analysis to determine the mineral phases present. The results are shown in Table I and Figure 1. The bulk chemical composition is given in Table II.

The converter matte was milled using a ball mill to a particle size distribution similar to that used by Sibanye-Stillwater so as to be in line with industrial practice. The size distributions are compared in Table III.

Spent electrolyte solution, which is the return anolyte from the copper electrowinning cells, was received from the plant, and analysed by ICP-OES for base metals and PGMs. The concentrations are shown in Table IV.

The acid level was determined by precipitating out all the metals with a Na₂CO₃/NaHCO₃ buffer and analysing the solution

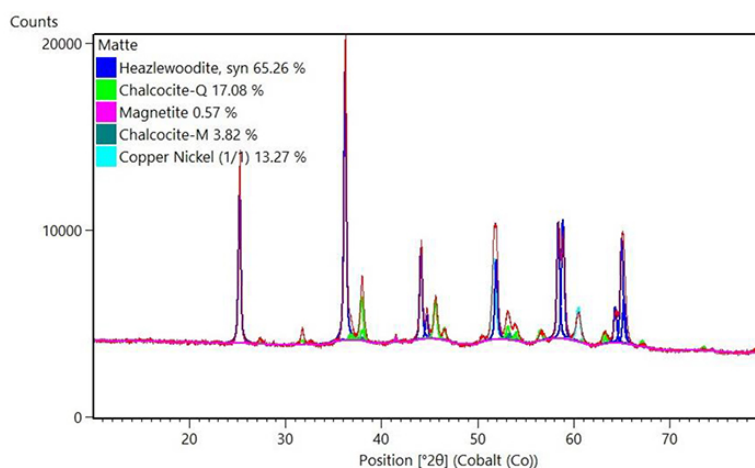


Figure 1—XRD spectrum of the matte sample

Behaviour of Cu, Fe, Ni, and PGMs during leaching of Ni-Fe-Cu-S converter matte

Table III

Particle size distributions of milled converter mattes (wt%)

Fraction (µm)	Industry	This study
-200+100	10.5	10.1
-100+80	6.5	6.3
-80+60	10.6	16.9
-60+40	16.1	14.8
-40	56.3	50.9

using high-performance liquid chromatography to determine the sulphate concentration. Four leaching solutions were prepared by diluting the concentrated spent electrolyte solution with an equal volume of distilled water. These four leaching solutions were used to investigate the effects of initial acid concentration or initial Cu concentration on the leaching kinetics of the base metals (Fe and Ni) and PGMs. For tests where a higher acid or Cu concentration was required, the desired concentrations were obtained by adding 98% sulphuric acid or copper sulphate pentahydrate crystals.

Experimental methods

The clean reactor vessel was weighed, 4 L of leaching solution added, and the vessel was weighed again to obtain the weight of the solution. The stirrer was started and set to a speed of 1100 r/min; simultaneously, the heating element was attached to the reactor vessel and the temperature on the PID controller set to 85°C. For oxidative leaching tests, the oxygen flow was turned on and the manual flow control valve set to a flow rate of 0.2 L/min. While the reactor contents were being heated to the

set-point value of 85°C, the pH and Eh probes were calibrated using pH standards of 1.69 and 4.0. The Eh probe was a platinum pin double junction Ag/AgCl electrode calibrated with ORP Quinhydrone solutions. Eh-pH stability diagrams were also depicted in Ag/AgCl (mV) used in simulations. The milled converter matte was added to the reactor once the leach solution reached the set temperature. Liquid samples were continually taken throughout the leaching tests at the 15, 30, 60, 120, 150, and 180 minute marks using syringes and 0.45 µm syringe filters.

The four leaching solutions prepared were used to investigate the effect of the initial acid concentration and initial Cu concentration on leaching behaviour, under oxidative and non-oxidative conditions. Table V summarizes the initial Cu and acid concentrations of each of the four leaching solutions used. The experiments carried out are summarized in Table VI. Three repeat experiments were conducted for each set of conditions in order to establish confidence in the results produced. The standard deviations were less than 10.

The oxygen flow rate used in this study was geometrically scaled down from the flow rate used at the BMR. Since the active volume of the laboratory-scale reactor was 4 L, the required oxygen flow rate for the oxidative leaching tests was 0.2 L/min. Van Schalkwyk *et al.* (2011) investigated three different solids to liquid ratios, namely 80 g/L, 150 g/L, and 540 g/L. It was found that at a solid to liquid ratio of 80 g/L complete Cu removal was not possible and hence in this study a solids to liquid ratio of 150 g/L was used to investigate the possibility of maximum Cu and PGE precipitation with reasonable Ni extraction using solutions with different chemical compositions.

Table IV

Composition of the spent electrolyte solution

Species	Ni ²⁺ (g/L)	Cu ²⁺ (g/L)	Fe ³⁺ (mg/L)	Co ²⁺ (mg/L)	Ir (mg/L)	Pd (mg/L)	Rh (mg/L)	Ru (mg/L)	Pt (mg/L)	H ₂ SO ₄ (g/L)
Concentration	42.36	26.77	337.77	297.8	31.49	0.0101	10.13	122.2	0.0151	100.04

Table V

Initial Cu and acid concentrations used in the experiments

Species	Solution 1 Low Cu-low acid (LCu-LA)	Solution 2 High Cu-low acid (HCu-LA)	Solution 3 Low Cu-high acid (LCu-HA)	Solution 4 High Cu-high acid (HCu-HA)
Cu (g/L)	13.385	26.77	13.385	26.77
H ₂ SO ₄ (g/L)	50	50	100	100

* Low (L), High (H) and Acid (A)

Table VI

Summary of experimental conditions

Experiment no.	Initial Cu conc. (g/L)	Initial acid conc. (g/L)	Temperature (°C)	Oxygen flow rate (L/min)
1	13.385	50	85	0
2	13.385	50	85	0.2
3	13.385	100	85	0
4	13.385	100	85	0.2
5	26.77	50	85	0
6	26.77	50	85	0.2
7	26.77	100	85	0
8	26.77	100	85	0.2
9 (repeat 1)	13.385	50	85	0
10 (repeat 6)	26.77	50	85	0.2
11 (repeat 3)	13.385	100	85	0

Behaviour of Cu, Fe, Ni, and PGMs during leaching of Ni-Fe-Cu-S converter matte

Sample analysis

Liquid samples taken during batch leaching tests were analysed immediately for pH and Eh to obtain data that was as close as possible to the conditions within the reactor. The instruments used were a HI 9321 microprocessor pH meter, capable of measuring pH at elevated temperatures, and a Eutech pH700 instrument with a platinum pin double junction Ag/AgCl electrode for Eh. Dissolved Cu, Ni, and Fe concentrations in the liquid samples from the leaching experiments, as well as in the original spent electrolyte solution, were analysed by means of atomic absorption spectroscopy (AAS) (Varian SpectrAA-250 Plus).

The dissolved PGE (Ir, Rh and Ru) concentrations in the liquid samples obtained from leaching experiments and in the original spent electrolyte solution were determined by ICP-MS. Pt and Pd were present at low concentration levels and were not considered in the study. For solid sample analysis, matte samples were digested in *aqua regia* for 24 hours to dissolve all the metals, and the resulting solutions analysed for Cu, Ni, and Fe by AAS.

Results and discussion

Previous research on the leaching behaviour of Ni-Cu-Fe-S mattes in sulphuric acid was conducted by Lamy and Lorenzen (2006), Füglerberg *et al.* (1995), Hofrek and Kerfoot (1992), Symens *et al.* (1979), and Llanos, Queneau, and Rickard (1974). Although these authors established the major features of the process, the results pertaining to the effects of different initial acid and Cu concentrations are sometimes contradictory or limited.

The Cu concentration is regarded as a leading indicator of PGE behaviour in plant operations, but this relationship has not been conclusively established. Van Schalkwyk, Eksteen, and Akdogan (2013) showed that the behaviour of Cu during

oxidative leaching may possibly be used as an indicator of whether PGEs will precipitate, but during non-oxidative tests Cu precipitation was found to be a poor indicator. Batch oxidative and non-oxidative experiments similar to those by van Schalkwyk, Eksteen, and Akdogan (2013) were therefore performed with the main aim of investigating the link between PGE and Cu behaviour, as well as establishing the conditions that promote PGE precipitation in the first-stage atmospheric leach. Here, we report the results of laboratory-scale experiments on the leaching of converter matte at atmospheric conditions to elucidate the effects of oxygen, Cu, and acid concentration on the precipitation behaviour of Cu, PGEs, and Ni extraction.

Effect of oxygen, copper, and acid concentration on PGE behaviour

The effect of oxygen is shown in Figure 2, which indicates that oxidative conditions are conducive to the precipitation of Cu, Ru, Ir and Rh. This is similar to the findings of van Schalkwyk, Eksteen, and Akdogan (2013) with respect to low-Fe mattes. Pt and Pd concentrations in the spent liquor were very low, and although some Pt and Pd precipitated out of solution, the amounts were negligible compared to those for other PGEs and these elements are therefore not included in further discussions.

Figure 3 compares Cu and Ru precipitation out of solution under oxidative and non-oxidative conditions. As seen, both Cu and PGE precipitation exhibit faster kinetics at low Cu and high acid concentrations under oxidizing conditions.

Van Schalkwyk, Eksteen, and Akdogan (2013) argued that Rh, Ru, and Ir are cemented, similarly to Cu. Dorfling (2012) agreed that the precipitation of Rh, Ir, and Ru proceeds primarily via reactions similar to the cementation and metathesis reactions of Cu precipitates (Equation [1]).

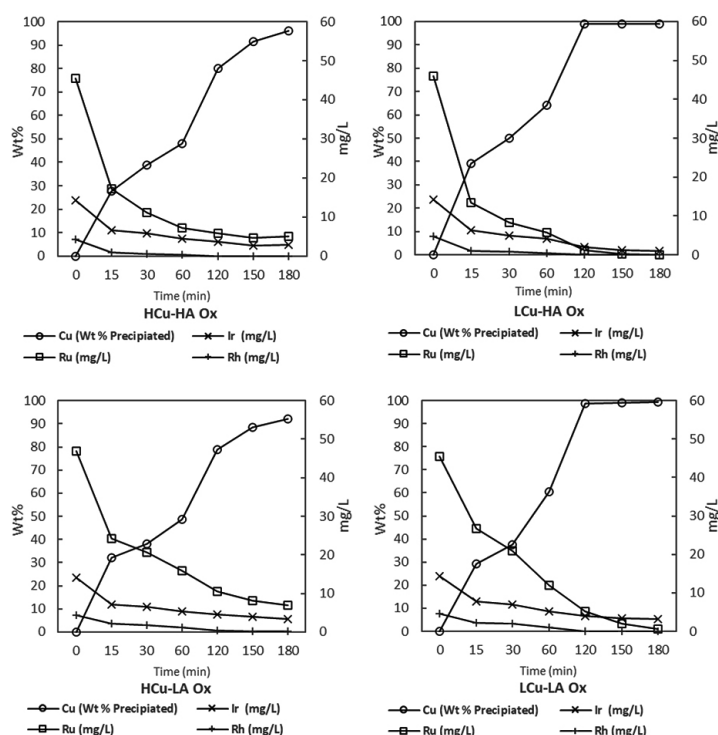
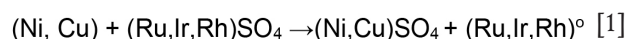


Figure 2—Precipitation kinetics of Cu, Ru, Ir, Rh, and Pt under oxidative leaching with LCu-(LA,HA) and HCu-(LA,HA) (Cu: 13.385 and 26.77 g/L, H₂SO₄: 50 and 100 g/L)

Behaviour of Cu, Fe, Ni, and PGMs during leaching of Ni-Fe-Cu-S converter matte

However, various studies propose different formulations for the precipitate, including $Ru(OH)_4$, $RuO_2 \cdot mH_2O$ and $RuO(OH)_2 \cdot H_2O$ (Baes and Mesmer, 1976).

Figures 4 and 5 depict Eh-pH measurements, monitored for a duration of 180 minutes, from each group of tests under different conditions, superimposed onto stability diagrams for Cu and Ru, Ir, and Rh.

As can be seen from Figure 4, Cu precipitated as Cu_2S in both oxidizing and non-oxidizing conditions. It is also observed that a low Cu concentration provided slightly better conditions for precipitation. Non-oxidizing conditions obviously shifted the ORP readings towards more reducing conditions closer to the Cu predominance field.

In Figure 5 one can clearly see that oxidizing conditions lead to the production of RuO_2 rather than Ru metal, perhaps closer to the postulation by Baes and Mesmer (1976). This is in contrast to non-oxidizing conditions, in which the precipitation product was Ru metal due to the prevailing reducing conditions. Figure 5 also indicates that under all conditions, Ir and Rh should precipitate

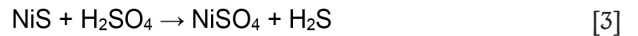
as the metals, which is in line with Dorfling's proposal (2012) summarized by Equation [1].

Effect of oxygen, copper, and acid concentration on Ni and Fe behaviour

It is generally accepted that in the presence of oxygen, leaching of the nickel sulphide phase proceeds according to Equation [2] (Llanos, Queneau, and Rickard, 1974; Plasket and Romanchuk, 1978; Hofirek and Kerfoot, 1992; Fugleberg *et al.*, 1995).



In the absence of oxygen, dissolution of the Ni from the sulphide phase takes place according to Equation [3] (Lamya, 2007);



Chalcocite (Cu_2S) leaching under atmospheric oxidative conditions proceeds by Equation [4] (Plasket and Romanchuk, 1978):

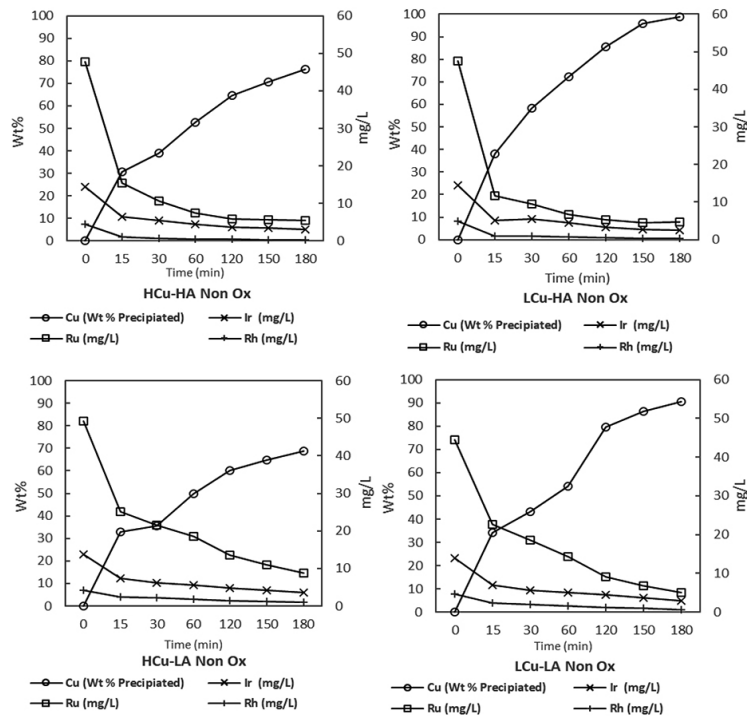


Figure 3—Precipitation kinetics of Cu and Ru under non-oxidative leaching with LCu-(LA,HA) and HCu-(LA,HA) (Cu: 13.385 and 26.77 g/L, H_2SO_4 : 50 and 100 g/L)

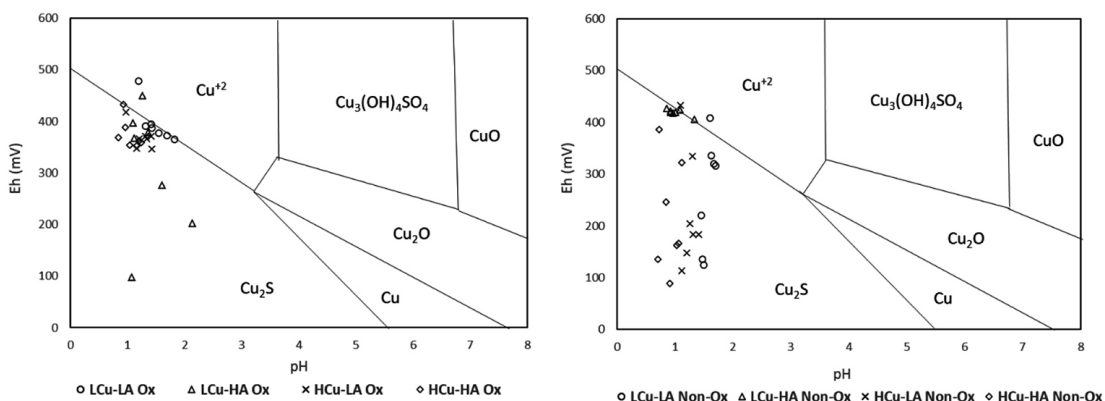


Figure 4—Stability diagrams for Cu precipitation under oxidative and non-oxidative leaching with (L,H)Cu-(L,H)A (Cu: 13.385 and 26.77 g/L, H_2SO_4 : 50 and 100 g/L) at 80°C (after Lamya, 2007)

Behaviour of Cu, Fe, Ni, and PGMs during leaching of Ni-Fe-Cu-S converter matte

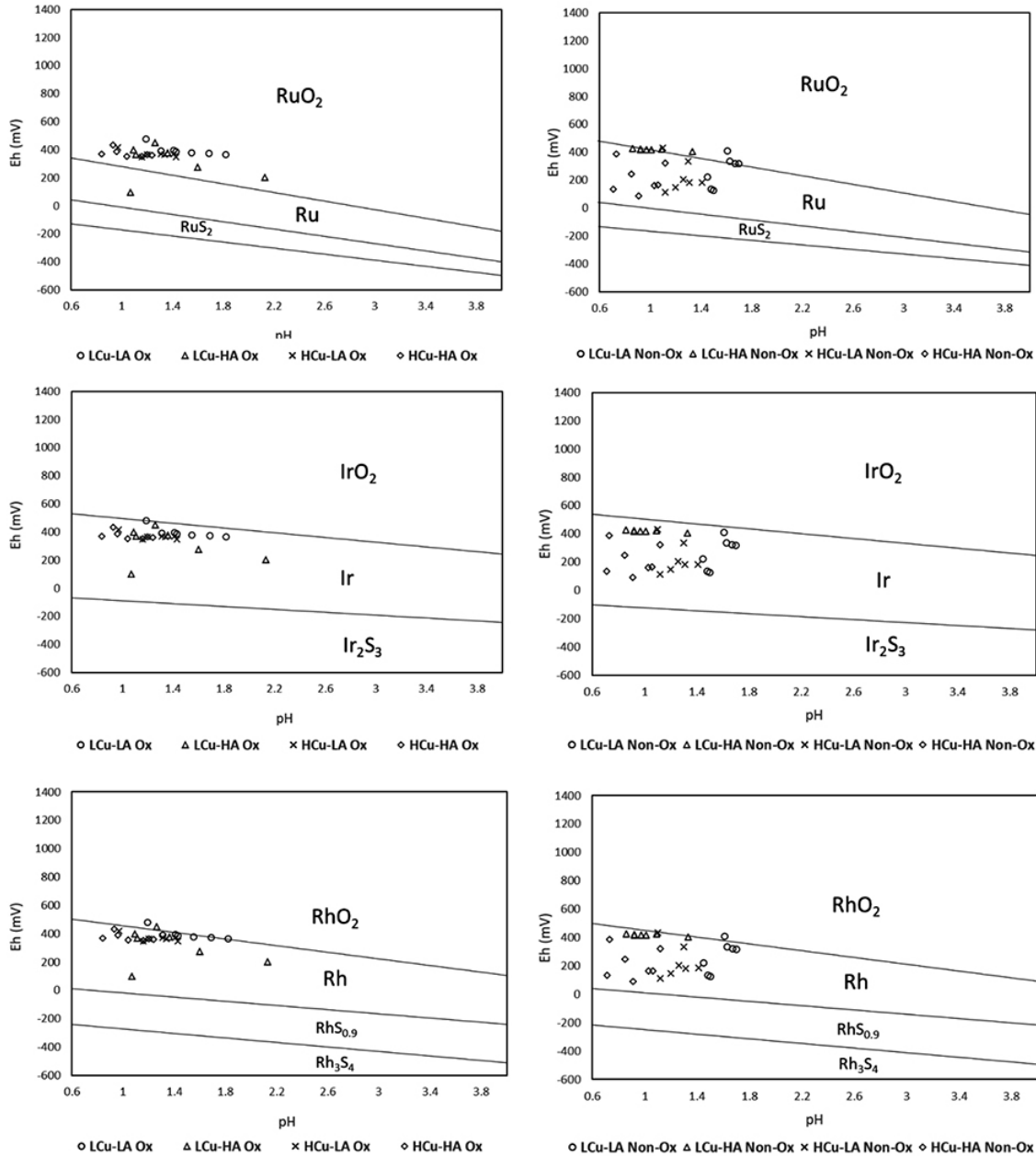
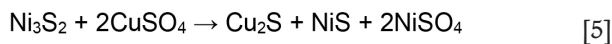


Figure 5—Stability diagrams for Ru, Ir, and Rh precipitation under oxidative and non-oxidative leaching with (L,H)Cu-(L,H)A (Cu: 13.385 and 26.77 g/L, H₂SO₄: 50 and 100 g/L), at 85°C



Being more noble than Ni, Cu from solution can exchange with Ni in the nickel sulphide matrix by metathesis (Equations [5], [6]) or with Ni from the alloy by cementation (Equation [7]).

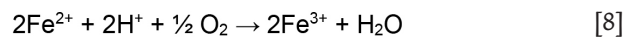


Although present in relatively small concentrations, Fe has been reported to play an important role as a catalyst and oxygen carrier to enhance the rates of the leaching reactions (Burkin, 2001; Mulak, 1987).

Figures 6 and 7 illustrate the leaching behaviour of Fe and Ni in oxidative and non-oxidative conditions in the presence of

Cu, and PGEs. It is clear from these figures that both Fe and Ni undergo greater dissolution from the matrix in the presence of high acid concentrations in an oxidative environment than in the absence of oxygen. Fe leaching proceeds much faster than Ni under both oxidative and non-oxidative conditions in low Cu-high acid conditions. However, the increase in Fe extraction and Cu precipitation coincides with diminishing Ru concentration in solution towards 20 mg/L.

(Hofirek and Kerfoot, 1992). At a low pH, ferrous ions are oxidized to ferric according to Equation [8].



Ferric ions can act as an oxidant in the leaching of heazlewoodite, which leads to ferrous ions being continuously regenerated (Equation [9]).



Behaviour of Cu, Fe, Ni, and PGMs during leaching of Ni-Fe-Cu-S converter matte

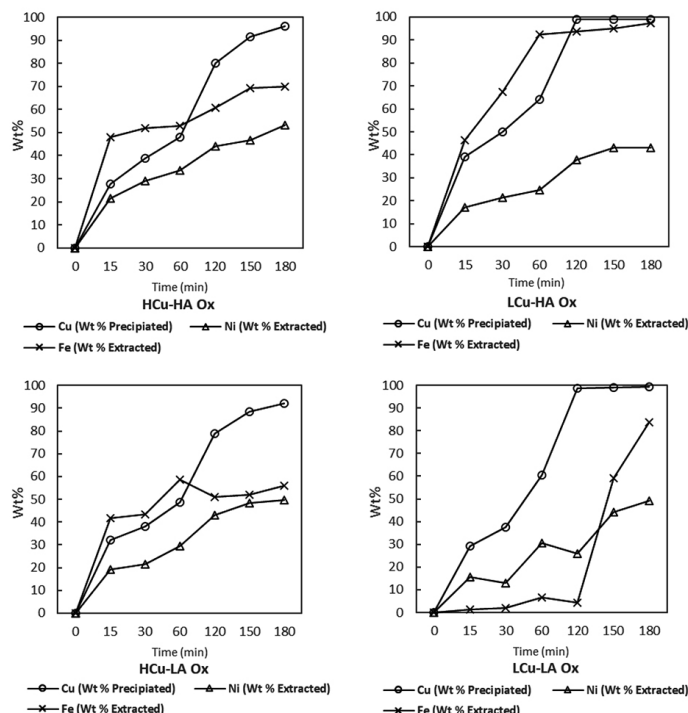


Figure 6—Leaching of Fe and Ni together with precipitation of PGEs under oxidative leaching with LCu-(LA,HA) and HCu-(LA,HA) (Cu: 13.385-26.77 g/L, H₂SO₄: 50-100 g/L)

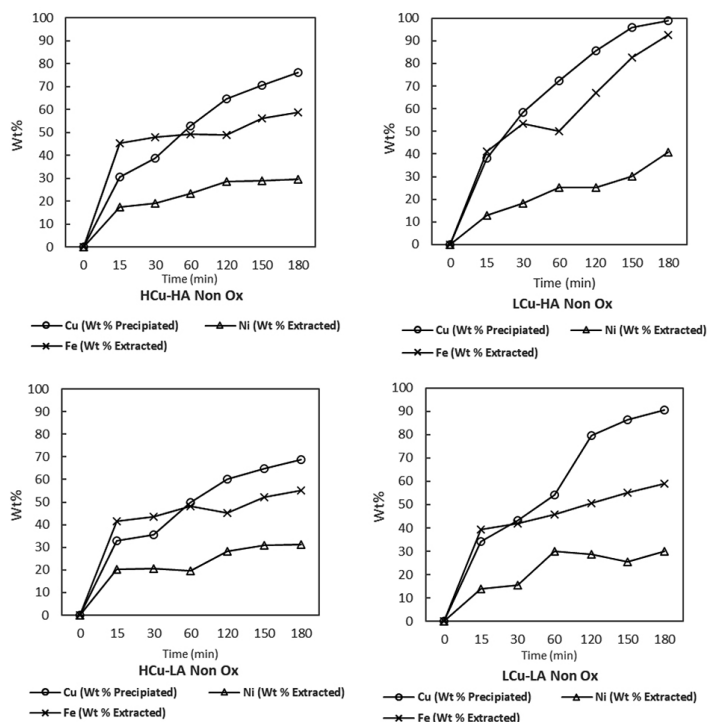


Figure 7—Leaching of Fe and Ni together with precipitation of PGEs under non-oxidative leaching with LCu-(LA,HA) and HCu-(LA,HA) (Cu: 13.385-26.77 g/L, H₂SO₄: 50-100 g/L)

The pH and Eh diagrams for Ni and Fe under both the oxidative and non-oxidative tests are shown on the Pourbaix diagrams in Figures 8 and 9. Ni and Fe are dissolved as Ni²⁺ and Fe²⁺, while Cu is precipitated as Cu₂S (refer to Figure 4).

Conclusions

The relationship between Cu, Ni, Fe, and PGE behaviour was investigated through a series of batch leaching tests replicating

the first-stage atmospheric leach in a base metal refinery. A low-Fe converter matte consisting mainly of heazlewoodite, chalcocite, Cu-Ni alloy, and minor magnetite was leached in a batch reactor under both oxidative and non-oxidative conditions at various acid and Cu concentrations.

The results revealed a higher degree of precipitation for Cu, Ru, Ir, and Rh under oxidative conditions, which agrees with the findings of van Schalkwyk, Eksteen, and Akdogan (2013)

Behaviour of Cu, Fe, Ni, and PGMs during leaching of Ni-Fe-Cu-S converter matte

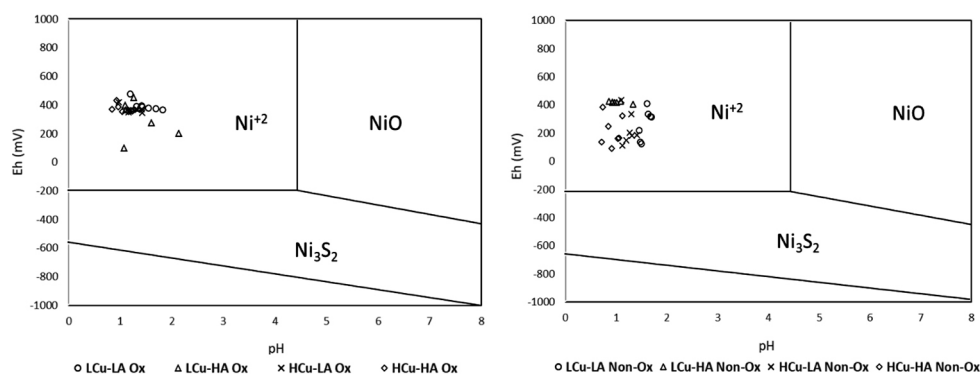


Figure 8—Stability diagrams for the Ni-S-H₂O system at 80°C (after Lamya, 2007) with the superimposed points indicating oxidative and non-oxidative leaching test results

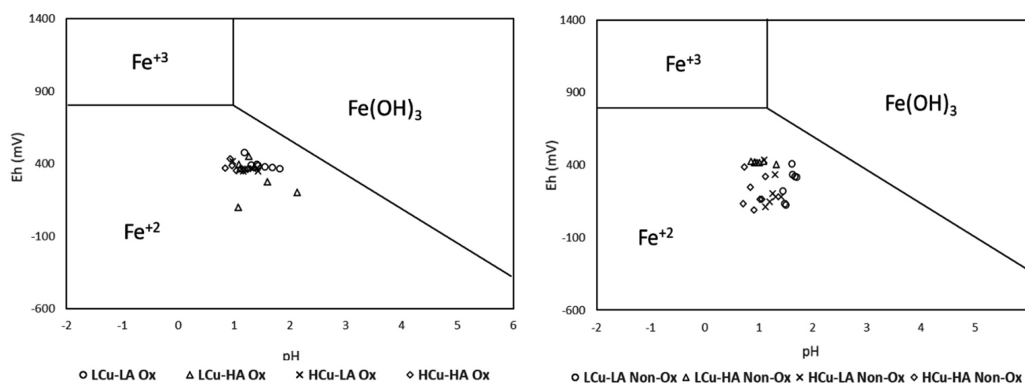


Figure 9—Stability diagrams for the Fe-S-H₂O system at 80°C (after Lamya, 2007) with the superimposed points indicating oxidative and non-oxidative leaching test results

and Snyder *et al.* (2018). The precipitation behaviour of Ru and Ir closely followed that of Cu. A high acid concentration had a positive effect on Cu, Ru and Ir precipitation, as well as Fe and Ni dissolution.

For oxidative leaching experiments it was found that a higher initial acid concentration resulted in higher Ni and Fe extractions, as well as faster leaching rates. A high initial acid concentration also resulted in faster precipitation of Cu, Ru, and Ir.

The effect of initial acid concentration on the leaching behaviour of Ni and Fe, as well as on the extent of Cu precipitation, was much less marked under non-oxidative conditions. A high initial Cu concentration had a negative effect on the leaching of Ni and Fe, as well as the precipitation of Cu and PGEs, under non-oxidative conditions.

Acknowledgements

The support by Sibanye-Stillwater (formerly Western Platinum Ltd) is gratefully acknowledged.

References

- BAES, C.F. and MESMER, R.E. 1976. *The Hydrolysis of Cations*. Wiley, New York.
- BURKIN, A.R. 2001. *Chemical Hydrometallurgy: Theory and Principles*. Imperial College Press, London. 414 pp.
- COETZEE, R., DORFLING, C., and BRADSHAW, S.M. 2018. Precipitation of Ru, Rh and Ir with iron ions from synthetic nickel sulphate leach solutions. *Hydrometallurgy*, vol. 175. pp. 79-92.
- CREAMER, M. 2006. The uses of platinum-group metals. *Mining Weekly*. <http://www.miningweekly.com/article/the-uses-of-platinumgroup-metals-2006-11-10>
- CRUNDWELL, F.K., MOATS, M.S., RAMACHANDRAN, V., ROBINSON, T.G., and DAVENPORT, W.G. 2011. Overview of extraction of platinum-group metals. *Extractive Metallurgy of Nickel, Cobalt and Platinum-Group Metals*. Elsevier. pp. 411-413.
- DORFLING, C. 2012. Characterisation and dynamic modelling of the behaviour of platinum group metals in high pressure sulphuric acid/oxygen leaching systems. PhD thesis, Stellenbosch University, South Africa.

- FÜGLEBERG, S., HULTHOLM, S.E., ROSENBACK, L., and HOLOHAN, T. 1995. Development of the Hartley Platinum leaching process. *Hydrometallurgy*, vol. 39. pp. 1-10.
- HOFIREK, Z. and KERFOOT, D. 1992. The chemistry of the nickel-copper matte leach and its application to process control and optimization. *Hydrometallurgy*, vol. 29. pp. 357-381.
- JONES, R. 2005. An overview of Southern African PGM Smelting. *Nickel and Cobalt 2005: Challenges in Extraction and Production. Proceedings of the 44th Annual Conference of Metallurgists*, Calgary, Alberta, Canada, 21-24 August 2005. Canadian Institute of Mining, Metallurgy and Petroleum, Montreal. pp. 147-178.
- LAMYA, R.M. 2007. A fundamental evaluation of the atmospheric pre-leaching section of the nickel-copper matte treatment process, PhD thesis, Stellenbosch University, South Africa.
- LAMYA, R. and LORENZEN, L. 2006. Atmospheric acid leaching of nickel-copper matte from Impala Platinum Refineries. *Journal of the Southern African Institute of Mining and Metallurgy*, vol. 106. pp. 385-396.
- LLANOS, Z.R., QUENEAU, P.B., and RICKARD, R.S. 1974. Atmospheric leaching of matte at the Port Nickel Refinery. *CIIM Bulletin*, vol. 67. pp. 74-81.
- MULAK, W. 1987. The catalytic action of cupric and ferric ions in nitric acid leaching of Ni₃S₂. *Hydrometallurgy*, vol. 17. pp. 201-214.
- PLASKET, R.P. and ROMANCHUK, S. 1978. Recovery of nickel and copper from high-grade matte at Impala Platinum by the Sherrit process. *Hydrometallurgy*, vol. 3. pp. 135-151.
- SNYDERS, C.A., AKDOGAN, G., THOMPSON, G., BRADSHAW, S.M., and VAN WYK, A.P. 2018. Investigating the behaviour of PGEs during first-stage leaching of a Ni-Fe-Cu-S converter matte. *Journal of the Southern African Institute of Mining and Metallurgy*, vol. 118. pp. 353-360.
- SYMENS, R.D., QUENEAU, P.B., CHOU, E.C., and CLARK, F.F. 1979. Leaching of iron-containing copper-nickel matte at atmospheric pressure. *Canadian Journal of Metallurgy and Materials Science*, vol. 18. pp. 145-153.
- THONON-ORD, A. 2017. Hydrogen to drive the energy revolution. <https://www.esi-africa.com/regional-news/international/hydrogen-drive-energy-revolution/>
- VAN SCHALKWYK, R.F., EKSTEEN, J.J., PETERSEN, J., THYSE, E.L., and AKDOGAN, G. 2011. An experimental evaluation of the leaching kinetics of PGM-containing Ni-Cu-Fe-S Peirce Smith converter matte, under atmospheric leach conditions. *Minerals Engineering*, vol. 24. pp. 524-534.
- VAN SCHALKWYK, R.F., EKSTEEN, J.J., and AKDOGAN, G. 2013. Leaching of Ni-Cu-Fe-S converter matte at varying iron endpoints; Mineralogical changes and behaviour of Ir, Rh and Ru. *Hydrometallurgy*, vol. 136. pp. 36-45. ◆



A critical review of initial Resource and Reserve tonnage estimation and reporting

by L. Roux

Affiliation:

¹Leon Roux Retired from Exxaro's Grootegeluk Coal Mine and continued with the Clean Coal Research Group at the University of the Witwatersrand during his research years preparing for this paper. Post Humous.

Correspondence to:

L. Roux
M. van Aswegen

Email:

marcia.vanaswegen@datamine-
software.com

Dates:

Received: 12 Nov. 2020
Revised: 1 Jun. 2021
Accepted: 2 Nov. 2021
Published: November 2021

How to cite:

Roux, L. 2021
A critical review of initial Resource and Reserve tonnage estimation and reporting.
Journal of the Southern African Institute of Mining and Metallurgy, vol. 121, no. 11, pp. 607–616

DOI ID:

<http://dx.doi.org/10.17159/2411-9717/1427/2021>

Synopsis

This review was initially motivated by the author's own experience in attempting to reconcile run-of-mine production tons with the Coal Resource and Reserve estimation of mineable, *in-situ* tonnages. The primary scientific measurements and observations that are collected during exploration at the beginning of the value chain will have a profound effect on the future of the mining operation. Due diligence must be exercised during the planning of a new mine and during the life of an existing mine.

The comments provided by the technical and economic assessment group of Venmyn Deloitte confirmed the need for this critical review. They found the reporting of Coal Resources in South Africa to be inconsistent. This was particularly problematic in the Waterberg Coalfield in Limpopo Province. In this coalfield there are two types of coal deposit present. The first is comprised of the thick intercalated, cyclic coal and shale/mudstone sequences of the Volksrust Formation. This overlies multiple coal seams within the Vryheid Formation, each of which is thick enough to be extracted as an individual raw coal unit. On the other hand, the interbedded coal and shale seams of the Volksrust Formation require beneficiation to separate the coal from the shale.

The review examines practices and methods, investigates alternatives, provides checks and balances, and tests these against actual production reconciliations. In conclusion, the best estimates of the mineable, *in-situ* tonnage will be obtained from the air-dry raw material density. These estimates should be adjusted afterwards to allow for free moisture content. The adjustments are derived from reconciliation data. The greatest contributing factor to the over-estimation of Reserve tonnages is the moisture content of the raw material. This fluctuates significantly under varying conditions in situ, as well as upon exposure to the natural environment. The air-dried density of the raw material includes inherent (structurally bound) moisture within the matrix. It provides credible tonnage estimations of raw material available while also providing an indication of voids within the volume of material being assessed. The calculated solids percentage can be used to adjust the specific gravity, which is determined *via* the Archimedes principle. This will supply a representative estimate of the material to be mined.

Keywords

Coal, Resource, Reserve, *in-situ* tonnage, density determination.

Introduction

Problems related to the reconciliation of product predictions and run-of-mine tonnages obtained from the geological model led to two major projects, initiated by the author, being undertaken at Grootegeluk Coal Mine in Limpopo Province. The initial project, 'Optimal yield prediction of semi soft coking coal and power station coal in the Waterberg Coalfield, Limpopo Province' (Roux, 2012) dealt with product prediction, actual production, and reconciliation, resulting in the determination of a beneficiation-plant-specific correlation factor applied to the predicted tonnages in order to reconcile the actual products from a specific beneficiation process. This was successful and relevant to the plant process, but did not satisfy the discrepancy between run-of-mine tonnages budgeted and those predicted from the geological model. The second project, 'The application of ash adjusted density in the evaluation of coal deposits' (Roux, 2017) addressed the discrepancy between the geological model values and actual reported run-of-mine tonnages by evaluating the whole process from exploration through the entire value chain. An assessment of the Resource material in the initial phases pertaining to exploration and laboratory processes, and various density determinations based on field and laboratory data through to run-of-mine reconciliation of mineable tons, was established.

A critical review of initial Resource and Reserve tonnage estimation and reporting

The physical make-up and properties of the material being mined should be understood and evaluated with regard to the matrix of the raw material and the probable geological losses with reference to the raw material determined prior to establishing Resource and Reserve values. Furthermore, consideration should be given to the compatibility of the feed material with the beneficiation processes and the required products. The prediction of run-of-mine feedstock and the expected product yields should be optimal and realistically based on the mining process, the beneficiation plants, products required, and material available.

This has been accomplished by a back-to-basics evaluation, starting at the exploration phase, through core recovery, depth corrections, lithological demarcation, lithological logging of the core, profile generation, and subsequent correlation for sample delineation, sampling, and preparation prior to dispatch to accredited laboratories for analyses, and an evaluation of laboratory results. All mass derivations from the exploration field, after Archimedes SG determinations through dispatch and laboratory receipt, as well as masses determined during and after sample preparation for analysis, were evaluated and various density determination calculations done for comparative purposes. It should be noted that no effort was made to determine the moisture content on recovery or impeccably preserve the exploration drill core after recovery in the field, therefore the *in-situ* moisture content of the core is unknown.

Basic evaluation of initial core mass, volume, and density

Drill core recovered from the core barrel is washed and laid out on 20 m corrugated sheeting. The core is depth-adjusted and marked off, differentiating the lithology with corresponding geophysical log data and depths for each lithology encountered. This is done to 1 cm accuracy. On completion of the borehole, the core is logged and described geologically, a profile of the borehole constructed, and the geological log is correlated with other boreholes from the area in order to conduct sample delineation. The samples are marked out on the core, sample depths recorded, and the core is sampled. General practises at Grootegeeluk require the samples to be separated into shale and coal components, the cut off values being anything less than 1 cm would be left in the overriding lithology. The samples are bagged and weighed as coal and shale samples separately. Field masses for the individual

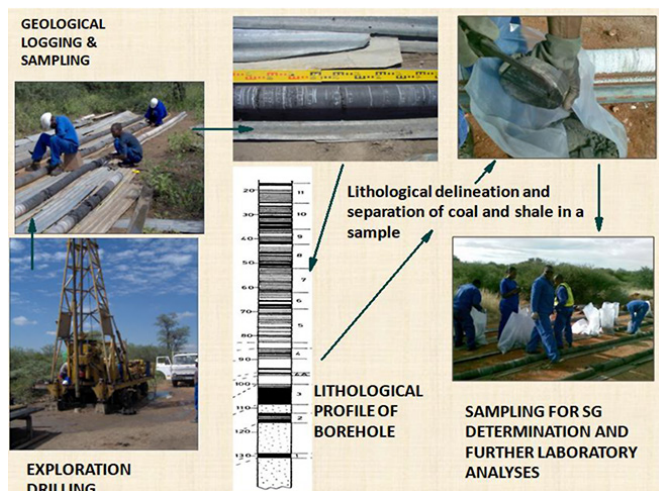


Figure 1—Pictorial flow illustrating the initial exploration phase from drilling to sampling

components *i.e.*, coal samples and shale samples are recorded since these masses would represent the received mass of the field sample in air. The samples are then subjected to SG determination *via* the Archimedes principle, the density derived is recorded, and a theoretical reconstruction to represent the original sample, *i.e.* coal and shale combined, is done to provide an SG for the entire sample. Samples are dried and re-weighed before dispatch to an accredited laboratory for analysis. Exploration core received by the laboratory is weighed on receipt, masses checked against field masses dispatched from the mine, and SG determinations done on coal and shale samples.

RECOVERED EXPLORATION COAL CORE SAMPLE

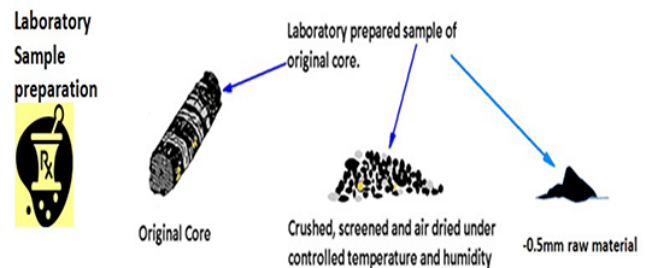


FIELD DETERMINATIONS

Core sample mass in air - 46440 g
 Core length - 257 cm
 Core diameter = 123 mm
 Core Area - 117.81 cm²
 Core Volume - 30227 cm³
 Field density = Mass / Volume = 1.53g/cc
 Core sample mass in water - 18464 g
 Archimedes principle SG = Mass in air / (mass in air - mass in water) - 1.66 g/cc

Figure 2—Coal core sample: basic field-determined density

BASIC INFORMATION FROM LABORATORY PROCESSES FOR SAME SAMPLE



The mass of the crushed and screened air dried products related to the envelope volume of the original core should approximate the air dry density of the sample.

Initial Laboratory information

Core received Mass	46450g
-13mm +0.5mm screened Mass	41113g
-0.5mm discard Mass	2990g
a) Density of core received	1.53g/cc
b) Density derived from -13+0.5mm material	1.36g/cc
c) Density derived from -13mm+0.5mm and the -0.5mm	1.46g/cc

Figure 3—Coal core sample: basic laboratory-determined density. SG = Mass in air / (mass in air - mass in water) = 1.66 g/cm³

A critical review of initial Resource and Reserve tonnage estimation and reporting

Sample preparation involves crushing and screening to prescribed top sizes and screening to -13 mm +0.5 mm, with the -0.5 mm fraction being retained for raw analysis. The crushed samples are then dried under controlled temperature and humidity conditions to represent air-dry samples, screened to -13 mm and +0.5 mm, and re-weighed before float and sink analysis. Float /sink analysis is performed in the range from 1.35 g/cm³, 1.40, 1.50 ... to 2.20 g/cm³ for coal samples and from 1.40 g/cm³ to 2.20 g/cm³ for shale samples, and the yields at each float fraction determined and recorded. Thereafter proximate analyses, total sulphur, Roga Index, crucible swell number, and calorific value, as well as ash analyses on the float and sink fractions, are completed for all samples, and the results recorded and forwarded to the mine.

Figure 4 portrays an evaluation of the different density values obtained from basic field and laboratory data.

Evaluation of laboratory data after float/sink and proximate analyses

The evaluation relates to two alternative methods of obtaining accurate density determinations for the samples. The first is an

ash-adjusted density algorithm derived from a regression of 31 000 float and sink data-sets to obtain an accurate absolute dry density value for each float fraction within a set range of fixed density values, and adjusting these with reference to the inherent moisture content determined in the laboratory to give a credible air-dry density value for the sample. The second approach, devised by Robeck and Huo (2015), is assessing the mineral matter content and then deriving a probable *in-situ* density based on averaged measured moisture content. Since averaged moisture content data for the Waterberg coals was not available, the laboratory-determined inherent moisture content of the samples was used instead. Both methods were validated by pycnometer-determined densities for the same samples. Research with regard to ash-adjusted density determined the contribution of mineral content for each fractional value from the data-set. As the mineral content increases, the ash yield content also increases, and each incremental increase represents a subtle increase in density between the previous fixed float density and the next cut-off float density.

Regression analyses based on cumulative frequencies of the various float fraction values were done on a 31 000 sample

An example of mass data and densities derived for the same sample portrayed below.

Coal									
SAMPLE NO	Lab Mass	-13mm Mass	<0.5mm mass	Arch, SG	THICKNESS (cm)	Core Volume	Field mass SG	Lab Mass SG	-13mm Mass SG
14	34620	30620	2387	1.58	202	23798	1.45	1.45	1.29
<13mm + <0.5mm Mass		33007				23798	Air Dry SG		1.39

Shale									
SAMPLE NO	Lab Mass	-13mm Mass	<0.5mm mass	Arch, SG	THICKNESS (cm)	Core Volume	Field mass SG	Lab Mass SG	-13mm Mass SG
14S	11654	10493	603	1.98	55	6480	1.81	1.80	1.62
<13mm + <0.5mm Mass		11096				6480	Air Dry SG		1.71

Combined Coal and Shale -13mm+0.5mm screened air dry material.									
SAMPLE NO	Lab Mass	-13mm Mass	<0.5mm mass	Arch, SG	THICKNESS (cm)	Core Volume	Field mass SG	Lab Mass SG	-13mm Mass SG
14	46274	41113	2990	1.68	257	30277	1.53	1.53	1.36

Combined Coal and Shale including -0.5mm material									
SAMPLE NO	Lab Mass	-13mm Mass	Total <.5 mm mass	Arch, SG	THICKNESS (cm)	Core Volume	Field mass SG	Lab Mass SG	Air Dry SG
14	46274	41113	2990	1.68	257	30277	1.53	1.53	1.36
Actual air dry Mass incl<.0.5mm		44103							1.46

Figure 4—Various density values obtained from different basic methods relating to field and primary laboratory data

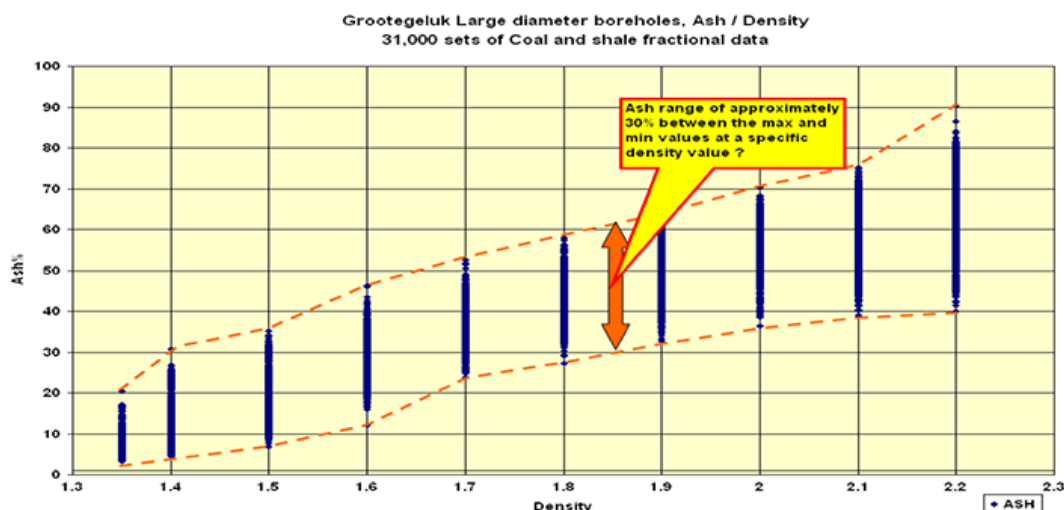


Figure 5—Distribution of ash percentage at each float density, illustrating the range of possible ash contents between float cut-offs

**DESCRIPTIVE STATISTIC RESULTS FOR DENSITY
FLOAT FRACTIONS ASH CONTENT ANALYSES**

	Ash 1,35 g/cc	Ash 1,40 g/cc	Ash 1,50 g/cc	Ash 1,60 g/cc	Ash 1,70 g/cc	Ash 1,80 g/cc	Ash 1,90 g/cc	Ash 2,00 g/cc	Ash 2,10 g/cc
Mean	7,34	13,51	20,22	28,48	35,96	42,32	48,15	53,32	57,08
Standard error	0,05	0,08	0,09	0,10	0,09	0,09	0,10	0,10	0,12
Median	6,99	14,06	21,00	29,20	36,41	42,61	48,60	53,70	57,67
Mode	6,10	16,00	21,70	29,90	37,60	44,00	51,00	52,70	59,10
Standard Deviation	2,09	3,62	4,14	4,23	4,14	4,16	4,33	4,48	5,12
Sample Variance	4,36	13,07	17,14	17,89	17,16	17,29	18,77	20,09	26,22
Kurtosis	3,03	0,52	0,14	-0,23	-0,30	-0,19	0,04	0,36	0,12
Skewness	1,29	0,17	-0,31	-0,26	-0,13	-0,15	-0,38	-0,46	-0,50
Range	17,22	26,23	25,40	27,50	27,96	30,70	29,10	31,80	31,61
Minimum	3,28	4,47	8,70	15,90	23,74	27,20	32,70	36,30	39,09
Maximum	20,50	30,70	34,10	43,40	51,70	57,90	61,80	68,10	70,70
Sum	14156,60	26103,04	39170,81	55259,82	69800,52	82064,53	92059,22	100987,23	107816,41
Count	1928	1932	1937	1940	1941	1939	1912	1894	1889
95% Confidence Level	0,09	0,16	0,18	0,19	0,18	0,19	0,19	0,20	0,23

Coal values from descriptive statistics based on original data-set used for AAD evaluation

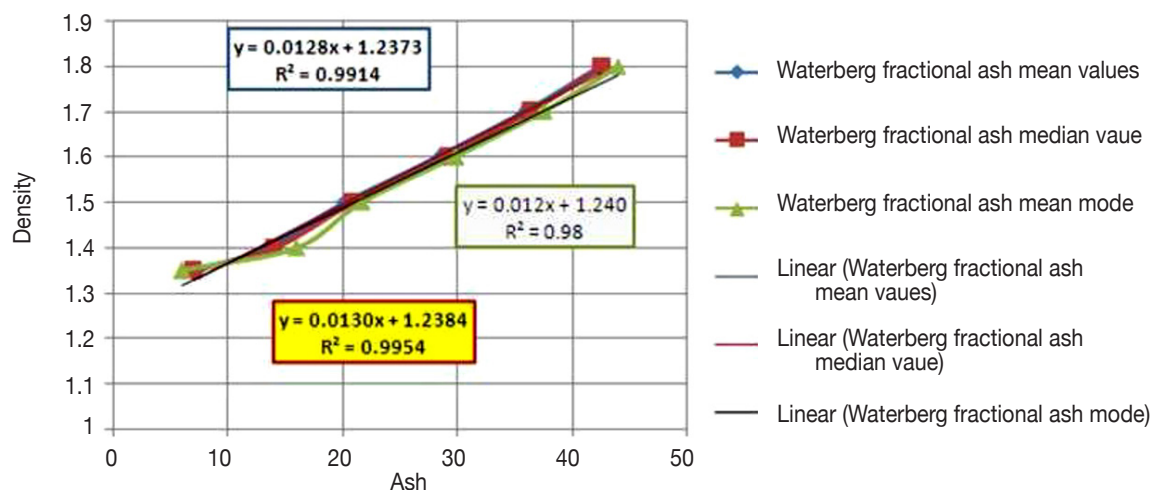


Figure 6—Descriptive statistics results and plots of the linear regressions on mean, median, and mode

data-set (Roux, 2012) and later refined through statistical methods to produce the algorithm eventually applied. The ash-density relationship displays the distribution around specific float densities and can be accommodated along the slope of increasing ash with increasing density (Roux, 2017).

The linear regression done on median values from descriptive statistics provided the following relationship:

$$RD = (0.013 \times \text{Ash}\%) + 1.238$$

which also resulted in an R2 value of 0.99. The constant 1.238 represents the density of bituminous coal. The credibility of the densities obtained was questioned; this led to a request that each fraction from samples in a new exploration borehole be subjected to pycnometry by the density bottle method (Australian Standard method AS1038.21 Item 4) to determine the densities of the individual fractions from the samples. A total of 741 'true relative densities' for float and sink fractions were determined according to this method. The coal and shale samples combined for the separate stratigraphic units, ash-adjusted density (AAD)-derived densities, and the re-determined laboratory densities were compared and statistically evaluated at a 99.9% confidence level. The differences between AAD and pycnometer-derived densities are illustrated in Figure 7. The AAD values had not been corrected to accommodate the inherent moisture content, thus they represent an absolute dry matrix density, and if this

correction is applied the values would be comparable with an air-dry density.

All three sets of values obtained at various confidence levels indicate a high level of accuracy. The evaluation based on a comparison between AAD-calculated values and laboratory-determined values indicates that the AAD methodology can be used confidently for predictions of dry densities in coal assessments. Minor differences between the two data-sets (AAD and pycnometer) are attributable to the inherent moisture content of the samples.

Robeck and Huo (2015), however, used another approach to ascertain *in-situ* density. Their study did not support the ash content as a basis for the evaluation of density since they believed that ash was a product of combustion and that inorganic volatiles would have contributed more to the losses through combustion. Their method is referred to as the Gray method.

The proposed evaluation requires an estimation of mineral matter content. The most commonly used approach is the Parr formula (Rees, 1966):

$$Md = 1.08 Ad + 0.55 Stot$$

where *Stot* = total sulphur (dry)
and the mineral matter ratio is determined by

A critical review of initial Resource and Reserve tonnage estimation and reporting

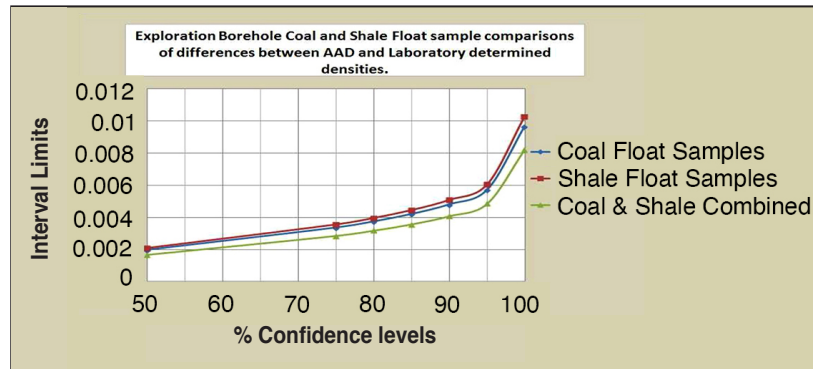


Figure 7—Differences between AAD predicted values and pycnometer-determined RD at various confidence levels, the combined coal and shale samples showing the lowest difference up to a 95% confidence level. This is smaller than 0.005

$$r = \frac{1.08 Ad + 0.55 Stot}{Ad}$$

The Gray method, in which Md cannot exceed 100%, accounts for a wider range of mineral volatiles and reveals changes in mineral content with increasing ash. This only requires specific energy (CV) and ash, and is the most robust method, particularly for high-ash samples. The relationship between dry CV and mineral matter is given by:

$$Ed = Edmmf \frac{100 - Md}{100}$$

where Ed = Specific energy, dry expressed in MJ/kg
 $Edmmf$ = Specific energy, dry mineral matter-free and the mineral matter ratio is determined by

$$r = \frac{100(Edmmf - Ed)}{Edmmf Ad}$$

The dry mineral matter-free CV is determined by:

$$Edmmf = \frac{100 * (CV - 0.15S)}{(100 * (Minh + 1.08) * (Ad + 0.55S))}$$

Mineral matter content is then derived by:

$$Md = rAd$$

(for all samples).

The determination of the air-dry density of the sample is then obtained from the equation:

$$\rho_{est} = \frac{100}{(a + b) * Md}$$

where coefficients a and b are determined by:

$$a = \left(\frac{Minh}{\rho_w} \right) + \left(100 - \frac{Minh}{\rho_c} \right)$$

where ρ_c represents the matrix density of bituminous coal (1.2384 g/cm³) and ρ_w is the density of water at 5°C (1.0 g/cm³).

$$b = \left(100 - \frac{Minh}{100} \right) * \left(\frac{\rho_c - \rho_m}{\rho_c * \rho_m} \right)$$

where ρ_m = density of the mineral matter. Here, 2.53 g/cm³ was used for Waterberg coals.

The individual sample densities can then be obtained from the following equations:

$$\rho_c = \frac{100}{a}$$

and

$$\rho_m = \frac{100}{a + (100 * b)}$$

The values determined from the AAD and Gray methods represent air-dry densities. The AAD values have been adjusted from an absolute dry (moisture-free) basis to an air-dry basis, including the analytical inherent moisture (%) so that all three data-sets are comparable. Note that the matrix density of bituminous coal at 1.2384 g/cm³ and that of the mineral content at 2.53 g/cm³ were the same as the values used in the AAD evaluation and have been used in the Gray method. Trends established by the AAD and Gray methods correlate almost perfectly, with a slight divergence in the higher ash regimes (Figure 8).

The assessment and tabulation of field, preliminary laboratory, and proximate analysis calculated values for the sample used in the example, which were obtained for density determinations, are illustrated in Table I. From the foregoing, very little difference is apparent between the methods utilizing the analytical data. Densities of 1.45 to 1.46 g/cm³ were obtained using an average correction factor of 0.83 for the solid matrix, which implies that the effective porosity of this sample is approximately 17%. In Table II the overestimation is determined by the final percentage by which the calculated value exceeds the mass of the measured air-dry material, *i.e.* the Archimedes-calculated mass of 50 865 g measured against 44 204 g results in an overestimation of approximately 15.06%. It is also apparent that the original field mass volume contains a fair percentage of moisture.

Reconciliation of actual production results, validating the foregoing with regard to basic Resource and Reserve tonnage estimations

From a mining production and reconciliation perspective two examples, one from the Volksrust Formation and the second from the Vryheid formation, were dealt with. These two scenarios are depicted in the locality map in Figure 9, showing the positions of the mining strips, blocks, and surrounding exploration boreholes from which the basic information with regard to mining block densities and expected run-of-mine tonnages were obtained. The same approach using the basic density equation was used in this

A critical review of initial Resource and Reserve tonnage estimation and reporting

Air dry float fractions ash/density comparisons on combined Volksrust & Vryheid Formation Data

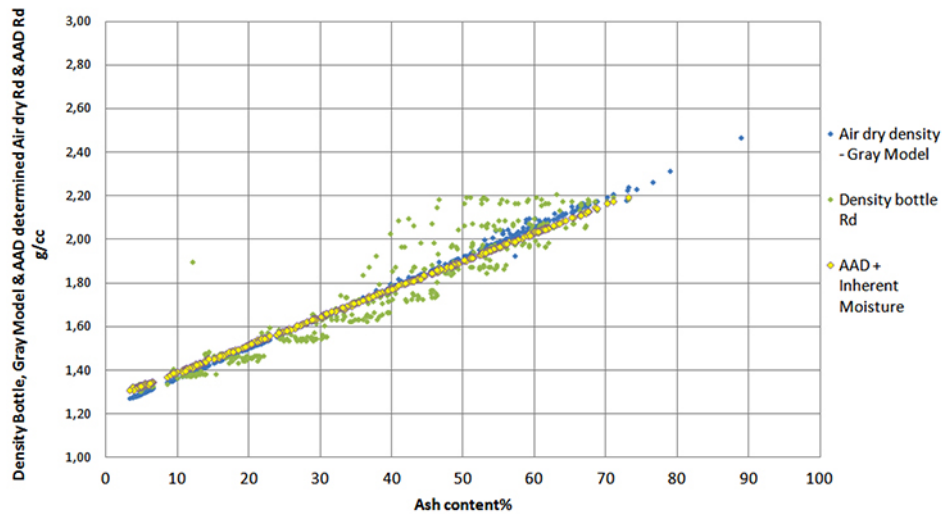


Figure 8—Plot of inherent moisture-adjusted AAD RD, Gray Method RD, and laboratory density-bottle-RD

Table I
Summary of derived densities using various methods of determination. Combined coal and shale

Determination method	Mass g	Volume cm ³	Density g/cm ³	Perceived % solids	Possible % voids	Mass loss from original field mass to other measured masses
Field and preliminary laboratory evaluation of perceived solids and voids						
Archimedes	46300	27560	1.68	0.91	0.09	26
Field mass/volume	46300	30277	1.529			
Lab mass./volume	46274		1.528			
Determination method	Mass g	Volume cm ³	RD	% Solids matrix	Possible % voids	
Laboratory sample preparation evaluation of perceived solids and voids						
-13 mm – 0.5 mm mass/volume	41113	30277	1.358	0.81	0.19	5187
Air dry mass including < 0.5 mm/volume	44103		1.46	0.87	0.13	2197
Determination method	Mass g	Volume cm ³	RD	% Solids matrix	Possible % voids	Air-dry RD derived from RD x % solid matrix
Validation of solid matrix RD based on pycnometer, AAD results and grey method						
Pycnometer RD	44103	25347	1.74	0.84	0.16	1.457
Absolute dry AAd RD			1.72	0.85	0.15	1.457
Air dry AAD RD			1.76	0.83	0.17	1.457
Gray method RD			1.75	0.83	0.17	1.460

Table II
Overestimation of core mass as a result of solid to void ratios

Determination method	Density g/cm ³	Volume cm ³	Actual solids volume cm ³	Voids volume cm ³	% voids	
Air dry mass including < 0.5 mm/volume	1.46	30277	25251	5026	16.60%	Based on average calc values from pycnometer, AAD and Gray methods. RD
Pycnometer RD	1.74		25347	4930	16.28%	
Air dry AAD RD	1.76		25130	5147	17.00%	
Gray method RD	1.75		25130	5147	17.00%	
Average for calculated values	1.75		25130	5147	17.00%	
Determination method	Density g/cm ³	Volume cc	Mass in grams = RD x volume	% Over estimation		
Archimedes	1.68	30277	50865.36	15.07%		
Air dry mass including < 0.5 mm/volume	1.46		44204.42			

A critical review of initial Resource and Reserve tonnage estimation and reporting

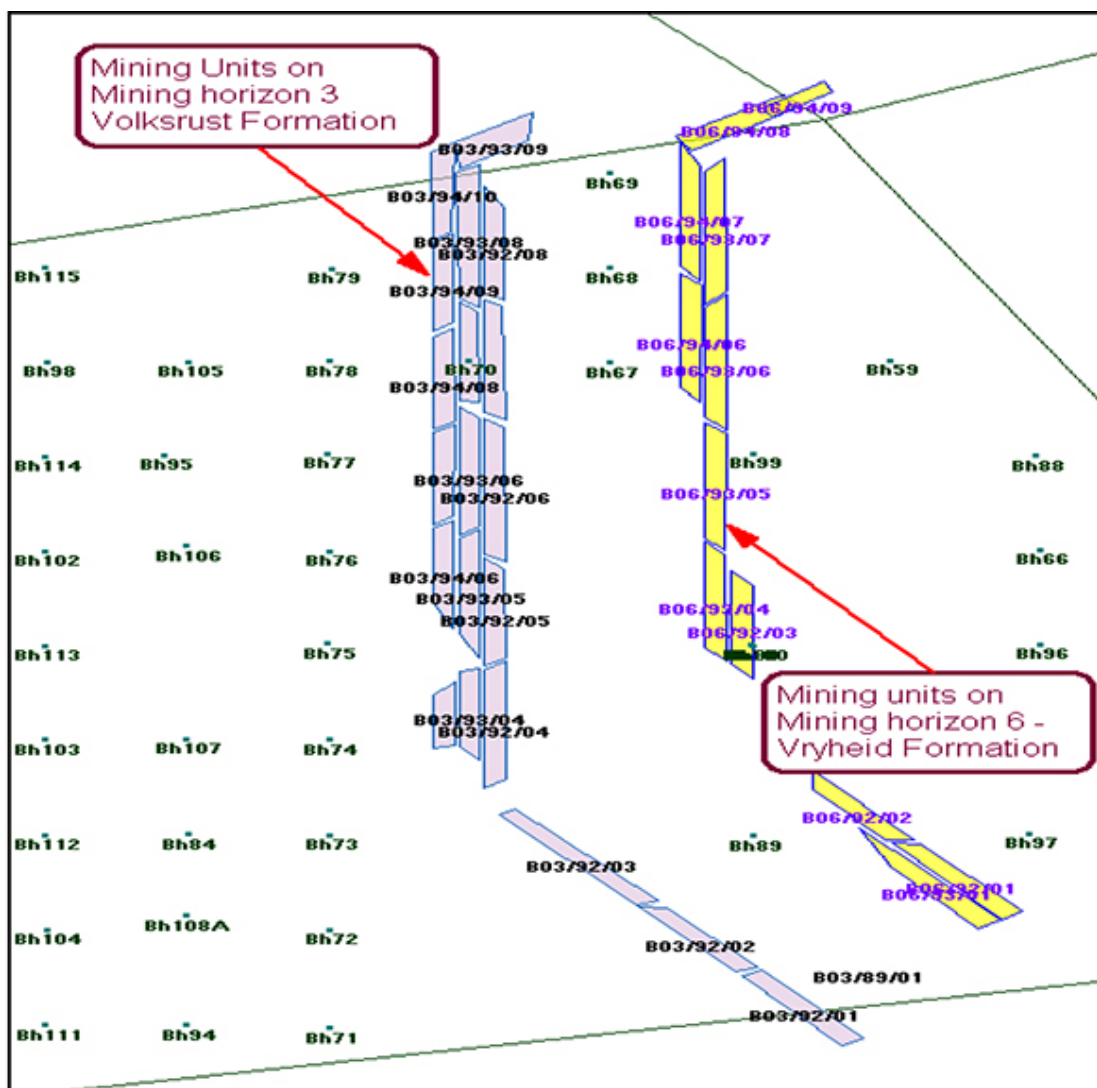


Figure 9—Locality map illustrating the respective mining strips, mining units, and mining horizons evaluated, with locations of boreholes over the entire area

evaluation. The masses relate to tonnages, the volumes in cubic metres to the material mined, and the initial densities allocated to the areas as well as the derived densities represented by the surveyed volumes and reported tonnages. Differences between the Volksrust Formation and the Vryheid Formation are depicted in Figure 10.

Two uniquely different types of deposit are represented by the mining horizons used in this reconciliation exercise. Mining horizon 3 in the Volksrust Formation represents a thick interbedded coal seam deposit, which includes coal and shale and requires beneficiation to separate the two main lithologies. The shales could be regarded as a contaminant but they need to be mined together, thus would constitute the raw reserve with respect to mineable run-of-mine tonnages. Mining horizon 6 in the Vryheid Formation, however, is classified as part of a multiple seam deposit; the coal portion can be extracted without beneficiation and can thus be considered as an *in-situ* Reserve.

Table III represents summaries of the weighted averages for the four data-sets relevant to the mining horizon 3 units, depicting tonnage differences and overestimation percentages.

In Table III, overestimation percentages are attributable to completely different areas, bench thicknesses, densities, and

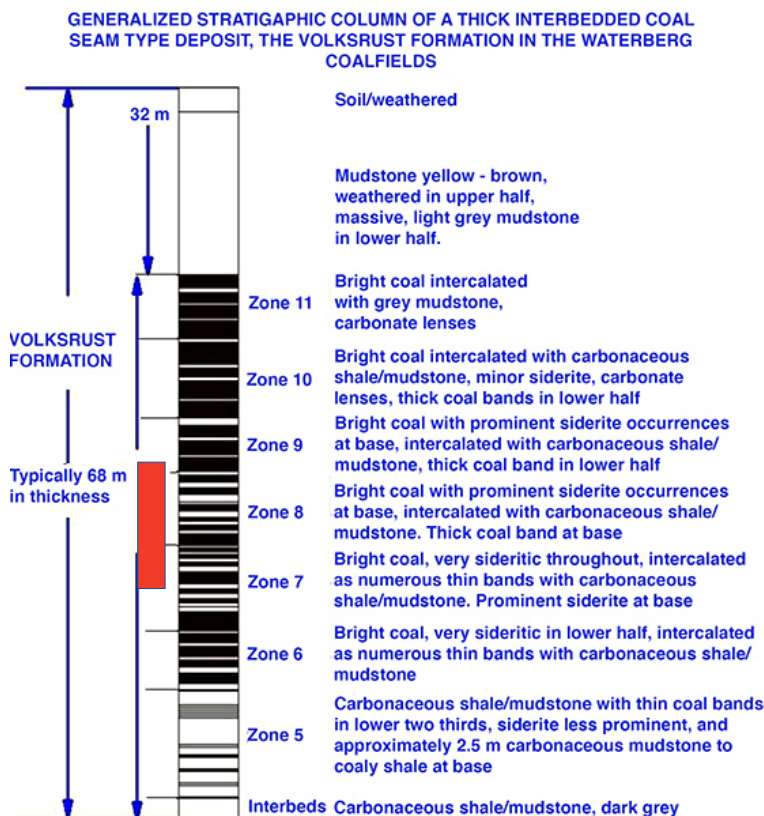
volumes planned and staked as opposed to the raw material actually mined. The most important difference, however, lies between the as-mined data and the surveyed data. In Table IV the areas, volumes, bench thicknesses, and relative densities for the model, staked, and as-mined scenarios have been equalized in order to compare the four scenarios on the same basis, the only difference being the tonnage for the surveyed material and its resultant density. This shows a difference of 17.41%, which could be attributable to the voids in the matrix, which implies that the solid matrix contributes only 82.59% to the final density.

In Table V the areas, bench thicknesses, and *in-situ* tons derived from raw density data are compared with surveyed areas and derived tonnages as well as dispatch values of tonnages sent to beneficiation plants. The dispatched tonnage divided by the surveyed tonnage show a loss of 17.89%, which may be indicative of voids in the original raw material which had not been taken into account in a geological loss factor. The actual density of the material dispatched to the various plants was 1.35 g/cm³, as opposed to the 1.65 g/cm³ used for planning or raw density for these blocks.

Finally, both the theoretical values obtained from a sample used illustratively and the reconciliation data pertaining to far

A critical review of initial Resource and Reserve tonnage estimation and reporting

MINING HORIZON 3 TYPE DEPOSIT



MINING HORIZON 6 TYPE DEPOSIT

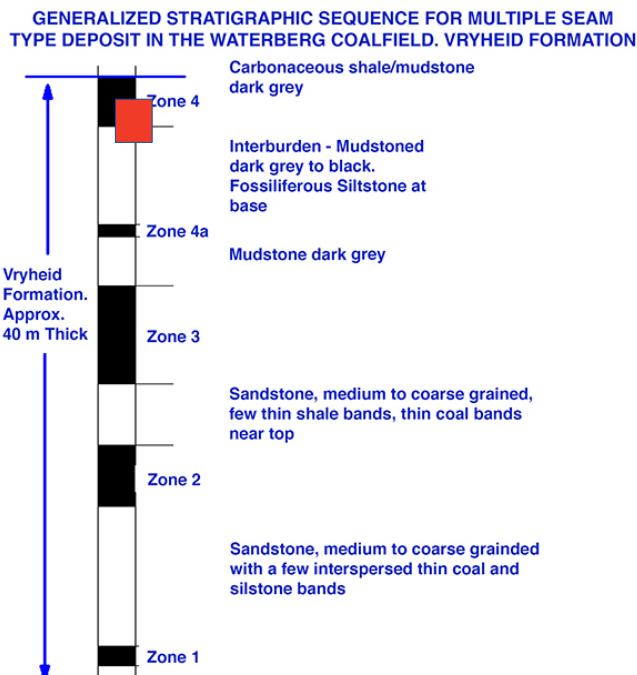


Figure 10—Waterberg coal deposit types, relating to the Volksrust Formation (left) and the Vryheid Formation (right)

Table III

Mining Horizon 3 in the Volksrust Formation

	Summary of initial reported values				
	Area	Thick	RD	Volume	Tonnage
Model	220 414.00	15.84	1.85	3 491 357.76	6 459 011.86
Staked	225 836.00	16.02	1.85	3 617 892.72	6 693 101.53
As mined	150 858.00	16.14	1.86	2 434 848.12	4 522 987.95
Surveyed	149 998.00	16.23	1.53	2 434 125.76	3 719 131.91
Model to surveyed tonnage difference					2 739 879.95
Model % overestimation					60.84%
Staked to surveyed tonnage difference					2 973 969.63
Staked % overestimation					44.43%
A-mined tonnage difference					803 856.04
As-mined % overestimation					17.77%

larger mining blocks, which in the case of mining horizon 3 comprise several samples in the vertical sequence and mining horizon 6, which is purportedly a relatively pure dull coal bench, have exhibited voids in the range of 16% to >17%.

Discussion

The initial requirement in the SAMREC Code pertains to an *in-situ* density of the resource material for tonnage estimations of 'mineable tonnes in situ'. The term *in-situ* requires the inclusion of all the matrix components, *i.e.* the solid matrix, moisture, voids, or gases contained within the matrix in order to ascertain

Table IV

Comparison of planning, survey, and mining data-sets on the same basis

	Calculated values for surveyed area and volume				
	Area	Thick	RD	Volume	Tonnage
Model	149 998.33	16.23	1.85	2 434 125.76	4 503 132.66
Staked	149 998.33	16.23	1.85	2 434 125.76	4 503 132.66
As mined	149 998.33	16.23	1.85	2 434 125.76	4 503 132.66
Surveyed	149 998.33	16.23	1.53	2 434 125.76	3 719 131.90
As-mined tonnage difference					784 000.76
As-mined % overestimation					17.41%

the tonnages of the raw material in its natural *in-situ* state. SAMREC should specify that tonnes *in-situ* must be reported on an air-dry basis.

Groundwater levels, porosity, and permeability would greatly influence the *in-situ* density of the material being assessed. By implication this requires exploration core to be impeccably preserved on recovery so that the adventitious moisture content may be accurately determined in the laboratory. Consider the two scenarios in Figure 11. In the first, illustrating an exploration borehole intersecting a coal sequence below the groundwater table, the probability of the core retaining the moisture is relatively good, provided that it is impeccably preserved on recovery. In the second example, a purported dry borehole, the core may still contain some moisture, relating initially to

A critical review of initial Resource and Reserve tonnage estimation and reporting

Table V

Bench 6 blocks with as-mined reported values as well as the final survey results

Block No.	As-mined reported dats			Model	Model	Survey measured data		Dispatch reported tonnages		
	Seam	As-mined area	As-mined bench thick	Equivalent as-mined <i>in-situ</i> tons	Archimedes raw RD	Surveyed volume	Surveyed tons	GG3	GG2	Toal despatch tons
B06/92/01	Bench 6	12 049	3.51	70 614	1.67	42 284	70 614	109 727	489	110 217
B06/92/02		10 926	3.92	70 614	1.65	42 797	70 614	82 095	1 309	83 404
B06/92/03		3 256	2.70	14 520	1.65	8 800	14 520	91 196	1 476	92 672
B06/93/01		31 934	3.56	188 867	1.66	113 775	188 867	56 746	813	57 559
B06/93/04		15 018	3.18	78 417	1.64	47 815	77 938	57 176	1 151	58 328
B06/93/05		10 751	3.47	61 108	1.64	37 261	61 108	70 092	1 633	71 725
B06/93/06		36 800	2.85	169 828	1.62	104 832	169 828	75 194	661	75 855
B06/93/07		15 273	3.10	77 246	1.63	47 390	77 246	77 423	1 194	78 616
B06/93/08		1 241	3.20	6 501	1.64	3 964	6 501	100 049	1 194	101 242
B06/94/06		69 319	2.26	255 861	1.63	156 970	255 861	51 522	3 447	54 968
B06/94/07	5 791	2.82	26 621	1.63	16 332	26 621	51 522	1 799	53 321	

Table VI

Comparison of planning, survey, and mining data-sets

	Summary of reported values				
	Area	Thick	RD	Volume	Tonnage
Model	15 805 4	4.05	1.64	63 950 6	10 487 24
Staked	15 523 5	3.73	1.64	57 837 3	94 770 5
As mined	21 235 7	2.93	1.64	62 222 0	102 019 6
Surveyed	21 236 2	2.93	1.64	62 222 0	10 197 18
Dispatch	21 236 2	2.93	1.35	62 222 0	83 790 8
Probable voides			17.89%		
Solid matrix			82.11%		

interstitially trapped water, to structural or inherent moisture, or moisture introduced during drilling. These values should also be ascertained since they will influence the overall apparent relative density of the material.

Another aspect to be taken into consideration relates to the time elapsed and possible changes to the *in-situ* environment between the exploration phase and actual mining of the deposit.

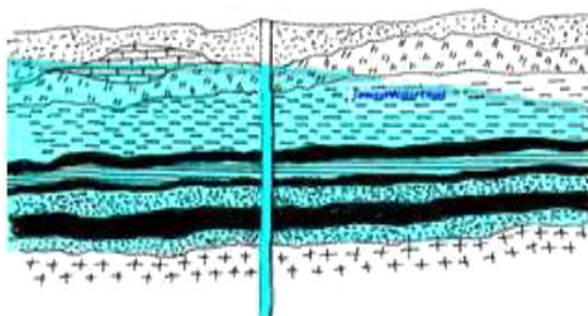
Consider an exploration borehole that may have been drilled several years earlier, prior to any mining activities, but is now in a position where an opencast mining operation has advanced closer to the borehole, on which the original determinations were done Groundwater has drained from this area into the mine's sump over the years and is now at a level below some of the coal seams, and the mining benches have been exposed

to the ambient atmospheric and climatic conditions for several years, thus rendering them effectively dry. Information with regard to *in-situ* densities determined during the exploration phase and used for mineable tons *in-situ* determinations will no longer be valid since the moisture content in the subsurface environment has changed over time. If, however, the densities were determined on an air-dry basis initially, the reference base and subsequent changes in moisture content or water content will have no influence.

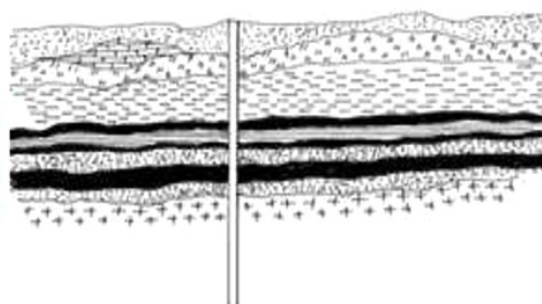
What would the *in-situ* moisture content of this material be? Assuming this is the same borehole as shown in the first scenario (Figure 11), the moisture content in the upper benches may be the same as for the borehole drilled through a dry area, similar to the one shown in the second scenario. Surely it is no longer feasible to use the values initially obtained for an *in-situ* density, especially if they were derived using the Archimedes principle method? The most logical value to use would be representative of the air-dry relative density, which at least partially conforms to the material being mined. This value would allow more credible Resource and Reserve tonnage estimations and an improved planned volume of material to be extracted in order to satisfy budgetary predictions.

Conclusions

- An intimate knowledge of the physical nature of the matrix is a prerequisite, since porosity of the matrix components contributes to the complexity.



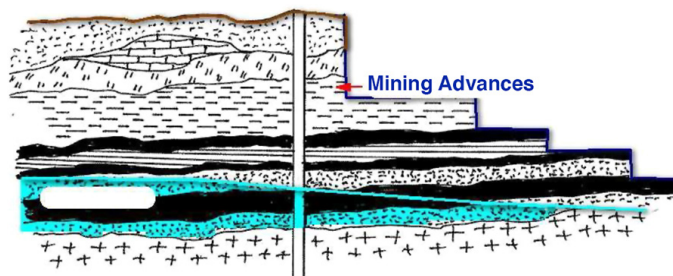
Scenarion 1 Coal measures below groundwater level



Scenarion 2 Essentially dry- no groundwater influence

Figure 11—Two exploration scenarios

A critical review of initial Resource and Reserve tonnage estimation and reporting



Scenario 3 Opencast mining approaches the exploration borehole illustrating the effect of the drainage of ground water over time

Figure 12—Effect of groundwater drainage over time

- Neither the Archimedes-determined SG nor RD determined by pycnometry are suitable for *in-situ* Resource tonnage estimation unless the samples were impeccably preserved and the moisture content determined.
- An idea of moisture content at the time of the Archimedes determination can be formulated by determining the volume required to support the derived SG. The difference between the initial volume and the determined volume would be indicative of the moisture content at that time.
- Pycnometer density would also require a reconstruction of the sample to its original state with regard to the initial volume of the sample.
- The air-dried, crushed, and screened masses reconstituted can be used with the original sample volume to give a representative air-dry RD.
- The representative air-dry RD value can be validated by utilizing both the AAD methodology and the Gray method, substituting the inherent moisture content. The AAD method would give an absolute dry density, which would then be adjusted by the inherent moisture content to provide an air-dry RD.
- This RD does not represent the *in-situ* RD but gives an accurate value for the matrix material to be recovered.
- The *in-situ* RD is applicable only when densities are determined immediately before mining, due to the changing environments with regard to the movement of groundwater and the time elapsed between original exploration and actual mining of the material.

Recommendations

It is recommended that SANS/SAMREC set a standard for the reporting of Coal Resource and Coal Reserve tonnages based the type of deposit, and specify air-dry tonnages for the Mineable Resources. These tonnages would be derived from the air-dry density of the resource matrix material, which is far more representative of the resource, in this case mineable coal, than a density derived for so-called *in-situ* values, including entrapped adventitious moisture. Water does not generate revenue!

References

- GRAY, V.R. 1983. A formula for the mineral matter to ash ratio for low rank coals. *Fuel*, vol. 62. pp. 94–97.
- HUANG, H., WANG, K., BODILY, D.M., and HUCKA, V.J. 1995. Density measurements of Argonne Premium coal samples. *Energy & Fuels*, vol. 9. pp. 20–24.

- KING, J.G. and WILKINS, E.T. 1944. The internal structure of coal. *Proceedings of the Conference on the Ultra-fine Structure of Coals and Cokes*, London, 1943. British Coal Utilization Research Association, London. pp. 46–56.
- McENANEY, B. and MAYS, T.J. 1989. Porosity in carbons and graphites. *Introduction to Carbon Science*. Marsh, H. (ed.), Butterworths, London. pp. 153–196.
- MEYERS, A., CLARKSON, C., WEX, T., and LEACH, B. 2004. Estimation of *in-situ* density of coal and relative density analyses. *Final Report for ACARP Project C10042*. Australian Coal Association Research Programme, Brisbane.
- MORLEY, C. 2003. Beyond reconciliation – A proactive approach to using mining data. *Proceedings of the Fifth Large Open Pit Conference*. Australasian Institute of Mining and Metallurgy, Melbourne. pp. 185–191.
- NOPPE, M. 2004. Reconciliation: Importance of good sampling and data QA/QC. *Proceedings of the Mining and Resource Geology Symposium*, XYZ, EGRU Contribution no 62.
- PRESTON, K. 2005. Estimating the in situ relative density of coal – Old favourites and new developments. *Proceedings of the Bowen Basin Symposium 2005, The Future for Coal – Fuel for Thought*, Yeppoon, Queensland. Beeston, J.W. (ed.). Geological Society of Australia Coal Geology Group and the Bowen Basin Geologists Group. pp. 13–22.
- PRESTON, K.B. and SANDERS, R.H. 1993. Estimating the *in-situ* relative density of coal. *Australian Coal Geology*, vol. 9, May. pp. 22–26.
- PRESTON, K. and SANDERS, R. 2005. Calculating reserves – A matter of some gravity. A study by Quality Coal Consulting Pty Ltd for Pacific Coal Pty Ltd.
- REES, O.W. 1966. Chemistry, uses and limitations of coal analyses. *Report of Investigations 220*. Illinois State Geological Survey. 55 pp.
- ROBECK, E. and HUO, D. 2015. Pure coal and mineral matter properties: A practical foundation for *in situ* density estimation. Peabody Energy, St. Lois, MO.
- ROUX, L. 2012. Optimal yield and cut density prediction of semi soft coking coal and powerstation coal in the Waterberg Coalfield, Limpopo Province. MSc dissertation, University of the Witwatersrand, Johannesburg.
- ROUX, L. 2017. The application of ash adjusted density in the evaluation of coal deposits. PhD thesis, University of the Witwatersrand, Johannesburg.
- ROUX, L. 2021. Density – A contentious issue in the evaluation and determination of Resources and Reserves in coal deposits. *Journal of the Southern African Institute of Mining and Metallurgy*, vol. 121, no. 5. pp. 227–250.
- UNSWORTH, J.F., FOWLER, C.S., and JONES, L.F. 1989. Moisture in coal: 2. Macerated effects on pore structure. *Fuel*, vol. 69. pp 18–26.
- WARD, C.R. (ed.). 1984. Coal Geology and Coal Technology. *Blackwell Scientific*, Melbourne. 345 pp.
- WARD, C.R. 2002. Analysis and significance of mineral matter in coal seams. *International Journal of Coal Geology*, vol. 46. pp. 67–82.
- WEBB, P.A. 2001. Volume and density determinations for particle technologists. Micromeritics Instrument Corp., Norcross, GA. ◆

NATIONAL & INTERNATIONAL ACTIVITIES

2021

15, 17, 19, 22, 24, 26 November 2021 — Global Tailings Standards and Opportunities Online Conference 2021

'For the Mine of the Future'

Contact: Gugu Charlie

Tel: +27 11 834-1273/7

Fax: +27 11 838-5923/833-8156

E-mail: gugu@saimm.co.za

Website: <http://www.saimm.co.za>

2022

23–24 February 2022 — Drill and Blast Hybrid Short Course 2022-Online via Zoom

Wits Club, Johannesburg

Contact: Camielah Jardine

Tel: +27 11 834-1273/7

Fax: +27 11 838-5923/833-8156

E-mail: camielah@saimm.co.za

Website: <http://www.saimm.co.za>

27 February–3 March 2022 — TMS Furnace Tapping 2022

Anaheim, California, USA

https://www.tms.org/AnnualMeeting/TMS2022/Programming/Furnace_Tapping_2022/AnnualMeeting/TMS2022/Programming/furnaceTapping.aspx?hkey=718f6af7-1852-445c-be82-596102913416

20–27 May 2022 — ALTA 2022 Nickel-Cobalt-Copper, Uranium-REE, Gold-PM, Lithium & Battery Technology Online Conference & Exhibition

Perth, Australia, Tel: +61 8 9389 1488

E-mail: alta@encanta.com.au

Website: www.encanta.com.au

14–16 June 2022 — Water | Managing for the Future

Vancouver, BC, Canada

<https://www.mineconferences.com>

Website: <http://www.saimm.co.za>

21–25 August 2022 — XXXI International Mineral Processing Congress 2022

Melbourne, Australia + Online

www.impc2022.com

24–25 August 2022 — Battery Materials Conference 2022

Misty Hills Conference Centre, Muldersdrift,

Johannesburg, South Africa

Contact: Gugu Charlie

Tel: +27 11 834-1273/7

Fax: +27 11 838-5923/833-8156

E-mail: gugu@saimm.co.za

Website: <http://www.saimm.co.za>

8–14 September 2022 — 32nd SOMP Annual Meeting and Conference 2022

Windhoek Country Club & Resort, Windhoek, Namibia

Contact: Camielah Jardine

Tel: +27 11 834-1273/7

Fax: +27 11 838-5923/833-8156

E-mail: camielah@saimm.co.za

Website: <http://www.saimm.co.za>

15–20 September 2022 — SDIMI 2022 10th International Hybrid Conference

Windhoek Country Club & Resort, Windhoek, Namibia

Contact: Gugu Charlie

Tel: +27 11 834-1273/7

Fax: +27 11 838-5923/833-8156

E-mail: gugu@saimm.co.za

Website: <http://www.saimm.co.za>

28–29 September 2022 — Thermodynamic from Nanoscale to Operational Scale (THANOS) International Hybrid Conference 2022

on Enhanced use of Thermodynamic Data in Pyrometallurgy Teaching and Research

Mintek, Randburg, South Africa

Contact: Camielah Jardine

Tel: +27 11 834-1273/7

Fax: +27 11 838-5923/833-8156

E-mail: camielah@saimm.co.za

Website: <http://www.saimm.co.za>

24–27 October 2022 — 8th Sulphur and Sulphuric Acid Conference 2022

Contact: Gugu Charlie

Tel: +27 11 834-1273/7

Fax: +27 11 838-5923/833-8156

E-mail: gugu@saimm.co.za

Website: <http://www.saimm.co.za>

2–4 November 2022 — PGM The 8th International Conference 2022

Sun City, Rustenburg, South Africa

Contact: Camielah Jardine

Tel: +27 11 834-1273/7

Fax: +27 11 838-5923/833-8156

E-mail: camielah@saimm.co.za

Website: <http://www.saimm.co.za>

2023

13–15 June 2023 — Copper Cobalt Africa In Association with The 10th Southern African Base Metals Conference

Avani Victoria Falls Resort, Livingstone, Zambia

Contact: Camielah Jardine

Tel: +27 11 834-1273/7

Fax: +27 11 838-5923/833-8156

E-mail: camielah@saimm.co.za

Website: <http://www.saimm.co.za>

Company affiliates

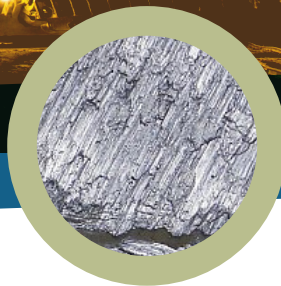
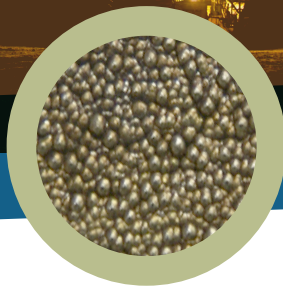
The following organizations have been admitted to the Institute as Company Affiliates

3M South Africa (Pty) Limited	Exxaro Coal (Pty) Ltd	MSA Group (Pty) Ltd
AECOM SA (Pty) Ltd	Exxaro Resources Limited	Multotec (Pty) Ltd
AEL Mining Services Limited	Filtaquip (Pty) Ltd	Murray and Roberts Cementation
African Pegmatite (Pty) Ltd	FLSmidth Minerals (Pty) Ltd	Nalco Africa (Pty) Ltd
Air Liquide (PTY) Ltd	Fluor Daniel SA (Pty) Ltd	Namakwa Sands(Pty) Ltd
Alexander Proudfoot Africa (Pty) Ltd	Franki Africa (Pty) Ltd-JHB	Ncamiso Trading (Pty) Ltd
AMEC Foster Wheeler	Fraser Alexander (Pty) Ltd	New Concept Mining (Pty) Limited
AMIRA International Africa (Pty) Ltd	G H H Mining Machines (Pty) Ltd	Northam Platinum Ltd - Zondereinde
ANDRITZ Delkor (Pty) Ltd	Geobruigg Southern Africa (Pty) Ltd	Opermin Operational Excellence
Anglo Operations Proprietary Limited	Glencore	Optron (Pty) Ltd
Anglogold Ashanti Ltd	Gravitas Minerals (Pty) Ltd	Paterson & Cooke Consulting Engineers (Pty) Ltd
Arcus Gibb (Pty) Ltd	Hall Core Drilling (Pty) Ltd	Perkinelmer
ASPASA	Hatch (Pty) Ltd	Polysius A Division Of Thyssenkrupp Industrial Sol
Aurecon South Africa (Pty) Ltd	Herrenknecht AG	Precious Metals Refiners
Aveng Engineering	HPE Hydro Power Equipment (Pty) Ltd	Rams Mining Technologies
Aveng Mining Shafts and Underground	Huawei Technologies Africa (Pty) Ltd	Rand Refinery Limited
Axiom Chemlab Supplies (Pty) Ltd	Immersive Technologies	Redpath Mining (South Africa) (Pty) Ltd
Axis House Pty Ltd	IMS Engineering (Pty) Ltd	Rocbolt Technologies
Bafokeng Rasimone Platinum Mine	Ingwenya Mineral Processing (Pty) Ltd	Rosond (Pty) Ltd
Barloworld Equipment -Mining	Ivanhoe Mines SA	Royal Bafokeng Platinum
BASF Holdings SA (Pty) Ltd	Joy Global Inc.(Africa)	Roytec Global (Pty) Ltd
BCL Limited	Kudumane Manganese Resources	RungePincockMinarco Limited
Becker Mining (Pty) Ltd	Leica Geosystems (Pty) Ltd	Rustenburg Platinum Mines Limited
BedRock Mining Support (Pty) Ltd	Longyear South Africa (Pty) Ltd	Salene Mining (Pty) Ltd
BHP Billiton Energy Coal SA Ltd	Lull Storm Trading (Pty) Ltd	Sandvik Mining and Construction Delmas (Pty) Ltd
Blue Cube Systems (Pty) Ltd	Maccaferri SA (Pty) Ltd	Sandvik Mining and Construction RSA (Pty) Ltd
Bluhm Burton Engineering (Pty) Ltd	Magnetech (Pty) Ltd	SANIRE
Bond Equipment (Pty) Ltd	Magotteaux (Pty) Ltd	Schauenburg (Pty) Ltd
Bouygues Travaux Publics	Malvern Panalytical (Pty) Ltd	Sebilo Resources (Pty) Ltd
Castle Lead Works	Maptek (Pty) Ltd	SENET (Pty) Ltd
CDM Group	Maxam Dantex (Pty) Ltd	Senmin International (Pty) Ltd
CGG Services SA	MBE Minerals SA Pty Ltd	SISA Inspection (Pty) Ltd
Coalmin Process Technologies CC	MCC Contracts (Pty) Ltd	Smec South Africa
Concor Opencast Mining	MD Mineral Technologies SA (Pty) Ltd	Sound Mining Solution (Pty) Ltd
Concor Technicrete	MDM Technical Africa (Pty) Ltd	SRK Consulting SA (Pty) Ltd
Council for Geoscience Library	Metalock Engineering RSA (Pty) Ltd	Time Mining and Processing (Pty) Ltd
CRONIMET Mining Processing SA Pty Ltd	Metorex Limited	Timrite (Pty) Ltd
CSIR Natural Resources and the Environment (NRE)	Metso Minerals (South Africa) (Pty) Ltd	Tomra (Pty) Ltd
Data Mine SA	Micromine Africa (Pty) Ltd	Traka Africa (Pty) Ltd
Digby Wells and Associates	MineARC South Africa (Pty) Ltd	Ukwazi Mining Solutions (Pty) Ltd
DRA Mineral Projects (Pty) Ltd	Minerals Council of South Africa	Umgeni Water
DTP Mining - Bouygues Construction	Minerals Operations Executive (Pty) Ltd	Webber Wentzel
Duraset	MineRP Holding (Pty) Ltd	Weir Minerals Africa
Elbroc Mining Products (Pty) Ltd	Mining Projections Concepts	Welding Alloys South Africa
eThekweni Municipality	Mintek	Worley
Ex Mente Technologies (Pty) Ltd	MIP Process Technologies (Pty) Ltd	
Expectra 2004 (Pty) Ltd	MLB Investment CC	
	Modular Mining Systems Africa (Pty) Ltd	

BATTERY MATERIALS CONFERENCE 2022

24-25 AUGUST 2022

MISTY HILLS CONFERENCE CENTRE,
MULDERSDRIFT, JOHANNESBURG



The intensified search over the past decade for alternatives to fossil-fuels as stores of energy has led to an exponential growth in the demand for batteries and research into battery technologies. The largest application by far has been in transportation, followed by electrical distribution grids.

Of the raw materials required for battery manufacture, metals such as cobalt, manganese and vanadium are highly concentrated in southern Africa. The supply of lithium, on the other hand, is concentrated in Australia, Chile and Argentina.

These activities have created both opportunities and challenges. Opportunities such as new value chains for the associated raw materials, with several production companies with battery-

material metals in their plant feedstocks undertaking research towards producing battery-grade products. And challenges such as the means for recycling these batteries once they reach the end of their (first) life.

The aim of this conference is to provide the opportunity for thought leaders in the global battery value chain to exchange ideas on recent developments in the fields of:

- Materials and high-purity intermediates for battery components
- Flow-battery electrolytes
- Processes for the recycling of batteries
- Market outlook and legislative implications
- Related case studies.

FOR FURTHER INFORMATION, CONTACT:

Gugu Charlie
Conference Co-Ordinator

E-mail: gugu@saimm.co.za
Web: www.saimm.co.za



SAIMM
THE SOUTHERN AFRICAN INSTITUTE
OF MINING AND METALLURGY

2 DAY HYBRID CONFERENCE

THANOS

PROJECT THERMODYNAMICS FROM NANOSCALE TO OPERATIONAL SCALE

INTERNATIONAL CONFERENCE ON ENHANCED USE OF THERMODYNAMIC DATA IN PYROMETALLURGY TEACHING AND RESEARCH

28-29 SEPTEMBER 2022 - CONFERENCE
VENUE - JOHANNESBURG (MINTEK)



NTNU



NWU®



東京大学
THE UNIVERSITY OF TOKYO



北京科技大学
University of Science and Technology Beijing

BACKGROUND

Fundamental knowledge of thermodynamic principles and data is important in understanding and improving processes used in the production of metals as well as in the design and development of new processes. This is particularly so given the fact that the production of metals from ores and/or secondary resources using pyrometallurgical processes involve complex thermochemical phenomena as a result of high temperatures and application of energy to materials. In most cases, however, pyrometallurgists do not fully appreciate the immense potential of thermodynamics to the design and operation industrial processes. This trend is worrying so as the engineering society is moving towards competencies focusing on a wide area of knowledge. The shift towards “Wikipedia knowledge” is a natural consequence of availability of huge amounts of information, but invariably, tends to occur at the expense of fundamental knowledge which forms the backbone of high quality thermodynamics teaching and research. In some instances, students and researchers tend to regurgitate derivations of thermodynamic equations with no indication of how such thermodynamic principles and data are to be put to practical use. To keep the interest and the dedication to the teaching, learning and application of thermodynamics principles and data, new teaching methods must continuously be developed with emphasis on how the fundamental knowledge is used in the research, design and operation of pyrometallurgical processes.

CONFERENCE OBJECTIVES

The broad objective of the International Conference on enhanced use of Thermodynamic Data in Pyrometallurgy Teaching and Research is to enhance the use of thermodynamic data in pyrometallurgy teaching and research. The ultimate goal is to increase competitiveness of the South African pyrometallurgical industry by demystifying thermodynamics and equipping the industry to use thermodynamic principles and data in metal production. Hosted by the Metallurgy Technical Programme Committee of the Southern African Institute of Mining and Metallurgy, this conference will focus on two main pillars: (a) the enhanced use of thermodynamic tools and data and the understanding the fundamental reaction mechanisms in metal production, and (b) developing methods for teaching thermodynamics and enhancing the teaching and learning and availability of thermodynamic methods and data. The project is funded by the Research Council of Norway through the Programme for International Partnerships (INTPART) under the project “Thermodynamic from Nanoscale to Operational Scale” (THANOS).



FOR FURTHER INFORMATION, CONTACT:

Camielah Jardine,
Head of Conferencing

E-mail: camielah@saimm.co.za
Tel: +27 11 834-1273/7
Web: www.saimm.co.za



SAIMM
THE SOUTHERN AFRICAN INSTITUTE
OF MINING AND METALLURGY